



NTNU – Trondheim
Norwegian University of
Science and Technology

Dynamic buckling of marine structures

Jonas Gullaksen Straume

Marine Technology

Submission date: June 2014

Supervisor: Jørgen Amdahl, IMT

Norwegian University of Science and Technology
Department of Marine Technology

MASTER THESIS 2014

for

Stud. Techn. Jonas Gullaksen Straume

Dynamic buckling of marine structures
Dynamisk knekking av marine konstruksjoner

The present trend is to build modern marine structures with small weight, high slenderness and highly optimized with respect to buckling. A few examples are tethers in tension leg platforms/wind turbines, shell structures in turbine towers, substructures in new generator concepts and container vessels. During extreme actions the static buckling resistance may be exceeded for a short period. The question is whether this is critical for the structure, notably when the governing buckling modes mobilize significant inertia forces or drag forces.

Another challenge may be related to displacement controlled buckling, i.e. the end of a panel or a column is subjected to constant rate end shortening; how much is the buckling force increased by comparison with static buckling? This issue is relevant for various impact scenarios.

The purpose of the work is to study the behaviour and resistance of relevant structural components subjected to impulsive type loads and constant rate shortening; thereby developing improved insight into dynamic buckling. The work is proposed carried out in the following steps:

- 1) Project work revisited. Establish the governing parameters for elastic dynamic buckling of simple columns and the SWAY tether. Analyse the tether with real dimensions and steel material. Both force and displacement controlled buckling shall be investigated. For the SWAY tether the response history during the straightening phase shall also be included.
- 2) Investigate elastic-plastic dynamic buckling of single columns and the SWAY tether.
- 3) Propose simplified design oriented strength formulations for dynamic buckling.
- 4) Perform dynamic buckling analysis of unstiffened and stiffened plates, both in the elastic and plastic range. Comparative analysis with USFOS and ABAQUS may be considered. The influence of initial displacements with respect to magnitude and buckling modes shall be examined. Relevant buckling modes shall be identified by means of eigenvalue analysis. Both force and displacement controlled buckling shall be investigated where the duration of loading and the mean stress may be varied. Results for elastic buckling shall be compared with the theoretical solutions given in R.E Ekstrom: *Dynamic Buckling of Orthotropic Plates*.
- 5) On the basis of the results in pt 4 propose simplified design oriented strength formulations for dynamic buckling.

- 6) Investigate dynamic buckling effects related to dropped object on subsea protection structures. The need to analyse local deformations at the pint of impact shall be considered.
- 7) Conclusions and recommendations for further work

Literature studies of specific topics relevant to the thesis work may be included.

The work scope may prove to be larger than initially anticipated. Subject to approval from the supervisors, topics may be deleted from the list above or reduced in extent.

In the thesis the candidate shall present his personal contribution to the resolution of problems within the scope of the thesis work.

Theories and conclusions should be based on mathematical derivations and/or logic reasoning identifying the various steps in the deduction.

The candidate should utilise the existing possibilities for obtaining relevant literature.

Thesis format

The thesis should be organised in a rational manner to give a clear exposition of results, assessments, and conclusions. The text should be brief and to the point, with a clear language. Telegraphic language should be avoided.

The thesis shall contain the following elements: A text defining the scope, preface, list of contents, summary, main body of thesis, conclusions with recommendations for further work, list of symbols and acronyms, references and (optional) appendices. All figures, tables and equations shall be numerated.

The supervisors may require that the candidate, in an early stage of the work, present a written plan for the completion of the work. The plan should include a budget for the use of computer and laboratory resources which will be charged to the department. OVERRUNS shall be reported to the supervisors.

The original contribution of the candidate and material taken from other sources shall be clearly defined. Work from other sources shall be properly referenced using an acknowledged referencing system.

The report shall be submitted in two copies:

- Signed by the candidate
- The text defining the scope included
- In bound volume(s)
- Drawings and/or computer prints, which cannot be bound, should be organised in a separate folder.
- The report shall also be submitted in pdf format along with essential input files for computer analysis, spreadsheets, MATLAB files etc in digital format.
-

Ownership

NTNU has according to the present rules the ownership of the thesis. Any use of the thesis has to be approved by NTNU (or external partner when this applies). The department has the right to use the thesis as if the work was carried out by a NTNU employee, if nothing else has been agreed in advance.

Thesis supervisor

Prof. Jørgen Amdahl

Contact person at Reinertsen:
Hagbart Skage Alsos

Deadline: June 10, 2014

Trondheim, January 14, 2014


Jørgen Amdahl

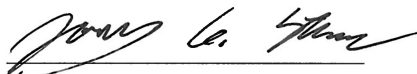
Preface

This report is a result of the master thesis conducted by Stud. Techn. Jonas Gullaksen Straume for the Department of Marine Technology at NTNU. The work has been carried in the spring of 2014. This is a continuation of the project thesis work carried out in fall 2013.

The purpose of this project is to study the behavior of structural components during dynamic compressive loading. Together with studies of the literature on the subject, gain an improved insight into dynamic buckling.

I would like to thank my supervisor Professor Jørgen Amdahl for good help and guidance during my work on the project. I would also like to thank Benjamin I. Brynstad and Hagbart S. Alsos from Reinertsen AS for answering questions about the riser impact case.

Trondheim, June 10, 2014



Jonas Gullaksen Straume

Summary

In this report the buckling resistance of marine structures when dynamic effects is important is investigated. A review of the governing theory is presented for both beam and plates. A sample of the different ways of solving the buckling problem is presented, and what kind of assumptions that are made. The overall conclusion from this study is that a structure may have a significant reserve capacity with respect to buckling when dynamic effects are important.

A selected solution to the dynamic buckling problem for unstiffened plates is chosen. A MATLAB program is written using this basis with numerical time integration. This program is compared with the finite element analysis programs USFOS and Abaqus FEA. The results were very similar to the finite element programs, and could predict for example the axial load with high accuracy.

An unstiffened plate was investigated with respect to dynamic buckling. Both displacement and load control was used. From this it was found that the dynamic buckling in an elastic analysis was not critical for the capacity of the plate. Buckling of the plate combined with a yield stress found that the capacity increased with dynamic effects.

An analysis of a tension leg in an offshore wind turbine was conducted. The top of the tension leg was displaced to simulate vertical motions of the wind turbine. The motions made the tension leg take compression forces. The result from this analysis was that the capacity of the tension leg increased substantially with fast-applied loads. The buckling motion of the leg could give large tension forces during the straightening of the leg. These forces could be critical for the leg, and larger than the corresponding compressive load.

The last type of marine structure investigated was a steel riser. The scenario examined was a production riser that was dropped from the platform, and the following impact with a subsea structure at the bottom. It was concluded that the energy of the impact was dependent on the curvedness of the riser. For a curved riser, a smaller amount of energy was dissipated to the deformation of the ground. The energy dissipation was also dependent on the deformation strength of the ground. If the riser yielded, the energy dissipated was much smaller. Risers with a lot of kinetic energy had high buckling modes as response near the impact. These

modes were very similar to the eigenmode corresponding to the impact durations. From this it could be said that the eigenmodes may have influence on the buckling mode, and strength.

For further work it is recommended that a design strength formulation is found for dynamic buckling, for both columns and plates. It is also recommended that the analyses of the marine structures gets expanded. Doing analyses on more complex structures with other actions included could give more insight on the effect of dynamic buckling.

Sammen drag

I denne rapporten har knekkingsmotstanden til marine konstruksjoner, når dynamiske effekter er viktige, blitt undersøkt. Den gjeldene teorien for dynamisk knekking har blitt drøftet for både plater og bjelker. Et utdrag av forskjellige løsningsmetoder for å løse knekkingsproblemet er blitt presentert, og hvilke antagelser som har blitt gjort. Konklusjonen fra denne undersøkelsen er at strukturer kan ha mye reservekapasitet for knekking når dynamiske effekter er viktige.

En av løsningsmetodene som ble presentert for dynamisk plateknekkning har blitt brukt videre. Et MATLAB-program har blitt skrevet med basis i denne metoden, og løst ved hjelp av numerisk tidsintegrasjon. Dette programmet ble sammenlignet med elementmetode-programmene USFOS og Abaqus FEA. Resultatene fra MATLAB-programmet var veldig like resultatene fra elementmetode-programmene. Aksialkraften ble for eksempel funnet med høy nøyaktighet i forhold til de etablerte programmene.

En ustivet plate ble undersøkt med hensyn på dynamisk knekking. Lasten ble påført som både forskyvning og kraft. Det ble funnet ut at dynamisk knekking ikke var kritisk for en plate i det elastiske området. Plateknekkning med en definert flytstyrke ble økt med høyere dynamiske effekter.

Et strekkstag i en offshore-vindmølle konsept har blitt undersøkt. Toppen av strekkstaget ble forskjøvet for å etterligne hiv-bevegelsene til vindmøllen. Disse bevegelsene fikk staget til å ta trykk-krefter. Hovedresultatene fra denne analysen var at knekkingskapasiteten økte kraftig ved rask påsatt last. Bevegelsen til staget etter knekking kunne gi store strekk-krefter i staget. Disse kreftene var i enkelte tilfeller større en knekklasten, og kunne være kritisk for staget.

Den siste strukturen som ble undersøkt var en stålriser. En produksjonsriser ble mistet fra en plattform, ved havoverflaten, og krasjer i subsea-utstyr på havbunnen. Det ble funnet at energien i kollisjonen var avhengig av konfigurasjonen til riseren. Mindre energi ble tatt opp hvis riseren var kurvete enn hvis den var rett. Energien, tatt opp i grunnen, var også avhengig av styrken til subsea-utstyret. Hvis riseren nådde flytspenning var den absorberte energien mye mindre. Riserkollisjonene med mye kinetisk energi hadde høye knekkmoder rett ved kollisjonsstedet. Disse modene var veldig like til den tilsvarende egenmoden med hensyn til kollisjonstiden. Fra

dette kan det konkluderes at egenmodene kan påvirke knekkmodene, og dermed knekkingsmotstanden.

For videre arbeid er det anbefalt å finne en designformulering for styrken til marine konstruksjoner med hensyn på dynamisk knekking. Dette kan finnes for både plater og bjelker. Det er også anbefalt at analysene av konstruksjonene blir utvidet. Hvis analyser blir gjort på mer kompliserte system, der andre laster blir tatt hensyn til, kan dette hjelpe med å gi mer innsikt i effekten av dynamisk knekking.

Contents

Scope of Work	i
Preface	v
Summary	vii
Sammendrag	ix
1 Introduction	1
2 Dynamic buckling of unstiffened plate	3
2.1 Analytical formulation	3
2.2 Numerical time integration	10
2.3 Finite element formulation	13
2.3.1 Dynamic formulation	14
2.3.2 The stiffness matrix	18
2.3.3 The damping matrix	21
3 Dynamic buckling of simple beam	25
3.1 Analytical formulation	25
3.2 Finite element formulation	28
3.2.1 Shape functions	29
4 Analysis of unstiffened plates	31
4.1 Setup of the analyses	31
4.1.1 End displacement analysis	33
4.1.2 Axial load analysis	33
4.1.3 Elastic-plastic analysis	34
4.2 Result of the analyses	35
4.2.1 Static buckling analysis	35
4.2.2 Eigenfrequency analysis	36
4.2.3 End displacement analysis	36
4.2.4 Axial load analysis	40
4.2.5 Elastic-plastic analysis	43

4.3	Discussion of the result	44
4.3.1	Static buckling and eigenfrequency analysis	44
4.3.2	End displacement analysis	44
4.3.3	Axial load analysis	48
4.3.4	Elastic-plastic analysis	49
4.4	Conclusion	50
5	Analysis of tension leg in SWAY concept	51
5.1	Setup of the analysis	52
5.1.1	Implementation of initial imperfection	54
5.1.2	Eigenfrequency analysis	56
5.1.3	Static analysis	56
5.1.4	Dynamic analysis	56
5.2	Result of the analysis	57
5.2.1	Eigenfrequency analysis	58
5.2.2	Static analysis	59
5.2.3	Dynamic analysis	62
5.2.4	Elastic-plastic analysis	64
5.2.5	Post buckling behavior	65
5.3	Discussion of the result	67
5.3.1	Analyses with spurious vibrations	67
5.3.2	Eigenvalue analysis	69
5.3.3	Higher buckling modes	70
5.3.4	Comparison with static analysis	72
5.3.5	Elastic-plastic analysis	72
5.3.6	Post buckling behavior	73
5.3.7	Mass calculations	74
5.4	Conclusion	75
6	Impact analysis of dropped riser	77
6.1	Setup of the analysis	77
6.2	Result of the analysis	85
6.2.1	Elastic analysis	89
6.2.2	Eigenvalue analysis	91
6.3	Discussion of the result	94
6.3.1	Energy considerations	94
6.3.2	Deformation of the risers	96
6.3.3	Elastic analysis	100
6.3.4	Eigenvalue analysis	101
6.4	Conclusion	101
7	Conclusion	103
8	Further work	105
	Appendices	

Appendix A Unstiffened plate analyses	I
A.1 MATLAB-code for the numeric time integration	I
A.2 Python script for Abaqus analyses	II
Appendix B SWAY analyses	V
B.1 BASH-script for USFOS runs	V
Appendix C Riser impact analyses	IX
C.1 Data for the production riser	IX
C.1.1 Details for the tapered stress joint	IX
C.2 Result of the riser impact analysis	X
C.2.1 Result from the stiff bottom analysis	X

List of Figures

2.1	A rectangular plate with compressive loading	4
2.2	Geometric description of bending deformation	5
2.3	Geometric description of membrane deformation	6
2.4	A typical axial slamming load time history	9
2.5	Constant average acceleration method	11
2.6	Constant initial acceleration method	12
2.7	Incremental solution of dynamic problem	16
2.8	Equilibrium iteration with Newton-Raphson method	17
2.9	In-plane force in x-direction for a plate [Leira, 2011, chap. 6]	20
2.10	Rayleigh damping given as a function of frequency	22
3.1	Simple bar with initial imperfections and axial loading	26
4.1	The Abaqus equation for the edge constraint	32
4.2	Buckling coefficient versus the plate aspect ratio for $n = 1$	35
4.3	The eigenmode shape for the static buckling case	36
4.4	Comparison between different analyses of edge displacement, $v = 5$ m/s, $m = 7$	37
4.5	Comparison between different imperfection shapes for $v = 5$ m/s . .	38
4.6	Axial force for $m = 7$ at $\Delta U = 1.36$ mm	39
4.7	Lateral deflection for $m = 7$ at $\Delta U = 1.36$ mm	40
4.8	Deformation of plate with $P_0 = 5.0 \cdot 10^6$ N and $\frac{t_0}{T} = 0.50$	40
4.9	Maximum deflection of plate at different force amplitudes	41
4.10	Force amplitude at different loading durations at given deflections .	42
4.11	Maximum deflection at different loading durations at given force amplitudes	42
4.12	Maximum deflection of plate at different force amplitudes, plastic analysis	43
4.13	Plastic deformation of plate with $P_0 = 1.5 \cdot 10^6$ N and $\frac{t_0}{T} = 2.00$. . .	43
4.14	Stress propagation in a plate after $2.3 \cdot 10^{-4}$ seconds	45
4.15	Plate shifts buckling shape from 3 to 9 half-waves over the length . .	46
4.16	Axial force for MATLAB results $m = 7$ at $\Delta U = 1.36$ mm	47
4.17	Axial force history for $v = 0.5$ m/s and $m = 7$	48

4.18	Maximum deflection of plate at different force amplitudes, d_{max} from 0 m to 0.02 m	49
5.1	Improved displacement history as one sinusoidal period	53
5.2	SWAY wind turbine model in USFOS	54
5.3	Initial imperfection of SWAY tension leg	55
5.4	The first three eigenmode shapes shown in USFOS	58
5.5	Eigenmode with a period of 0.20 seconds	59
5.6	Static buckling analysis in USFOS	60
5.7	Dynamic loading factor for the dynamic analyses	61
5.8	Maximum axial compression load of tension leg	62
5.9	Load history of tension leg for $A = 1.00$ m and $T = 0.25$ s	64
5.10	Maximum axial compression load of tension leg	64
5.11	maximum axial tension load of tension leg	65
5.12	Load history of tension leg for $A = 1.00$ m and $T = 1.00$ s	66
5.13	First maximum axial compression load of tension leg	67
5.14	Time history for axial load for $A=1.00$ m and $T=100$ s with vibrations	67
5.15	Original displacement history of SWAY spar as half-sine wave	68
5.16	Buckling response for $A = 1.00$ m and $T = 0.25$ s	69
5.17	Change in maximum loading with varying amplitude and $T = 10$ s	71
5.18	Change in maximum loading with varying period and $A = 0.1$ m	71
5.19	Plastic deformation of the tension leg with $A = 1.0$ m, $t_0 = 1.0$ s	73
5.20	Configuration of tension leg with max tension force	74
6.1	Sketch of the production riser	78
6.2	Drop of production riser with different length and drop angle	80
6.3	Riser configuration for PA	80
6.4	Riser configuration for PC	81
6.5	Riser configuration for PF	81
6.6	Riser configurations with no scaling	82
6.7	Sketch of the spring deformation and equivalent elastic-plastic behavior	83
6.8	Riser deformation during impact for scenario PF at 85° and scale = 5	86
6.9	Riser deformation during impact for scenario PF at 85°	87
6.10	Representation of wall thickness for PF at 85°	88
6.11	Comparison of riser before and after impact for scenario PF at 85° and scale = 5	90
6.12	Load history for the bottom spring, scenario PF85	91
6.13	Eigenmodes for the PF-riser	92
6.14	Vertical velocity of riser top for the softer bottom	95
6.15	Buckling wave traveling, PF85 at $t = 0.2$ and scale = 5	97
6.16	The force and relative displacement of the PA-riser	98
6.17	The force and relative displacement of the PF-riser	98
6.18	Collapse mode for the PF85 scenario	99
6.19	Stress propagation for the PF-riser at 85° at 0.02 s	100
C.1	Deformation of PA-riser	X

C.2	Deformation of PC-riser	XI
C.3	Deformation of PF-riser	XI

List of Tables

4.1	Properties of the unstiffened plate	32
4.2	Shows the different velocities of the edge	33
4.3	Shows the half-waves for imperfection shapes	33
4.4	Shows the different loading periods	34
4.5	Shows the different loading amplitudes	34
5.1	Properties of the SWAY tension leg	53
5.2	Shows the different displacement amplitudes	57
5.3	Shows the different displacement duration periods	57
5.4	Eigenperiod and eigenmode shapes for the tension leg	58
5.5	Result of the static analysis	60
5.6	Dynamic analysis with a loading period $T = 5s$	62
5.7	Dynamic analysis with a displacement amplitude $A = 0.5m$	63
6.1	Material properties of 80 ksi grade steel	78
6.2	Components of production riser	79
6.3	Drop scenarios for production riser	79
6.4	Stiffness used on bottom	84
6.5	Kinetic energy of the riser scenarios	85
6.6	Maximum axial load during an impact for a $1 \cdot 10^7$ N/m stiffness impact	85
6.7	Maximum axial load during an impact for a $1 \cdot 10^8$ N/m stiffness impact	87
6.8	Energy absorbed in softer spring used on bottom	88
6.9	Energy absorbed in stiffer spring used on bottom	89
6.10	Maximum axial load during an elastic impact for a $1 \cdot 10^8$ N/m stiffness impact	89
6.11	Eigenperiods for bottom stiffness $1.0 \cdot 10^7$ N/m	92
6.12	Eigenperiods for bottom stiffness $1.0 \cdot 10^8$ N/m	93
6.13	Energy comparison for bottom stiffness $1.0 \cdot 10^7$ N/m	94
6.14	Energy comparison for bottom stiffness $1.0 \cdot 10^8$ N/m	95
C.1	Stiffness used on bottom	XII

Nomenclature

A	Cross sectional area [m ²]
a	Length of a plate [m]
\mathbf{B}	Strain-displacement matrix
b	Width of a plate [m]
C_d	Drag coefficient [-]
C_m	Mass coefficient [-]
\mathbf{C}	Global damping matrix
\mathbf{C}_I	Incremental damping matrix
c_N	Nonlinear damping coefficient [kg/m]
c_{eq}	Equivalent damping coefficient [kg/s]
\mathbf{D}_b	Plate flexural rigidity matrix
dt	Time increment [s]
d_{max}	Maximum lateral deflection [m]
E	Young's modulus [Pa]
E_k	Kinetic energy [J]
E_s	Strain energy [J]
$f_{0,nm}$	Initial imperfection amplitude for buckling mode n, m [m]
f_{nm}	Lateral displacement amplitude for buckling mode n, m [m]
h	Plate thickness [m]
I	Second area moment [m ⁴]
\mathbf{K}	Global stiffness matrix
\mathbf{K}_I	Incremental stiffness matrix

k	Plate buckling coefficient [-]
L	Length of the beam [m]
\mathbf{M}	Global mass matrix
m	Number of half-waves in x-direction
N	In plane force [N/m]
\mathbf{N}	Shape function vector
n	Number of half-waves in y-direction
P	Applied axial loading [N]
P_0	Axial load amplitude [N]
p	Average compressive stress [Pa]
p_0	Average stress amplitude [Pa]
\mathbf{q}	Beam nodal displacement vector
\mathbf{R}	Global load vector
\mathbf{r}	Global nodal displacement vector
\mathbf{S}	Plate stretching rigidity matrix
T	Period [s]
t	Time [s]
t_0	Duration of loading [s]
u	Displacement in x-direction [m]
\dot{u}_0	Velocity of deformation in x-direction [m/s]
v	Displacement in y-direction [m]
\mathbf{v}	Element nodal displacement vector
W_{ext}	External work [J]
W_{int}	Internal work [J]
w	Lateral displacement [m]
w_0	Initial imperfection [m]
w_A	Lateral displacement amplitude [m]
$w_{0,nm}$	Initial imperfection for buckling mode n, m [m]
w_{nm}	Lateral displacement for buckling mode n, m [m]
α_k	Weight factor for damping terms [-]

γ_{xy}	In-plane shear strain [-]
Δ	Displacement error [m]
ε_x	Strains in x-direction [-]
ε_y	Strains in y-direction [-]
ν	Poisson's ratio [-]
ρ	Material density [kg/m ³]
σ_E	Static buckling stress for perfect plates [Pa]
σ_x	Stress in x-direction [Pa]
σ_y	Stress in y-direction [Pa]
τ_{xy}	In-plane shear stress [Pa]
Φ	Airy's stress function [N/m ⁴]
ϕ	Beam shape function vector
ω	Frequency [rad/s]
ω_n	Eigenfrequency for eigenmode n [rad/s]

Chapter 1

Introduction

The present trend is to build modern marine structures with small weight, high slenderness and highly optimized with respect to buckling. A few examples are tethers in tension leg platforms/wind turbines, shell structures in turbine towers, substructures in new generator concepts and container vessels. The load carrying members in the structures could be prone to compressive axial loads. During extreme actions the static buckling resistance may be exceeded for a short period. The dynamics of the structure now becomes important. Inertia forces for the structure can counteract the buckling movement. Damping forces, like drag, could also contribute to the increase in buckling capacity. The question is how much increases the capacity of the structure.

Another question is if the capacity is dependent on how the buckling is induced. A high enough load from slamming could be a relevant buckling problem. The capacity could be dependent on both the amplitude and the duration of the load. Another way to induce buckling is by displacement control. This is, for example, an approximation of a large mass colliding with the structure. Then the strength of the structure is negligible to the mass, and a constant end shortening can be used. How does the capacity of the member change when the displacement rate change. Could the yield capacity of the member be the important factor if the buckling capacity increases enough?

Dynamic buckling problems introduce often very complicated problems even on simple structures. Giving non-linear second order differential equation, making the problem impossible to solve analytically. A highly versatile method of study dynamic buckling problems is to use finite element method.

In this thesis a short introduction of the governing theory for dynamic buckling has been presented, for both beams and plates. Analytical solution methods that have been proposed are presented. The governing methods in Finite Element Analysis (FEA) that are used when solving dynamic buckling problems are also presented.

The dynamic buckling of unstiffened plates has been investigated. Both displacement control and load control have been used to induce buckling. The effect amplitude and duration of the displacement and load have been investigated. Abaqus FEA and USFOS have been used to solve the problems, and an analytically proposed solution has been compared to the finite element method.

The tension leg of an offshore wind turbine has been investigated. The buckling strength of different sinusoidal displacement has been found. It has been found if buckling or yielding limits the capacity of the tension leg in compression. The response of the tension leg during the straightening phase has also been investigated.

A riser that has been accidentally dropped from an offshore platform has been considered. When the highly slender member impacts the seabed or subsea equipment below, does the buckling capacity of this member contribute on the impact deformation. This has been examined. Different lengths and drop scenarios has been considered. The response of the riser during impact has been investigated.

Chapter 2

Dynamic buckling of unstiffened plate

To get an understanding of the parameters that govern dynamic buckling, a unstiffened plate is considered. Plates are important structural members for marine structures. The governing ways to solve the dynamic buckling problem for a plate is presented in this chapter.

2.1 Analytical formulation

A rapid variation of compressive loading for a plate can also induce dynamic buckling. A thin isotropic rectangular plate can be used to analyze the effect of a compressive load relevant for marine structures. Figure 2.1 is used when describing the plate. The length of the plate in the x-direction is a , and b is the length in y-direction. The plate is assumed to be simply supported in both x- and y-direction. The plate has a stress loading, $\sigma_x(y, t)$, in the x-direction. The stress can vary in the y-direction and with time, t . The plate has an initial displacement in z-direction denoted w_0 .

Ekstrom [1973] describes a general orthotropic plate with the same conditions as shown in Figure 2.1. The result can therefore be used for the more specialized isotropic plate. The strains are defined by the in-plane displacements and the second order out of plane displacements.

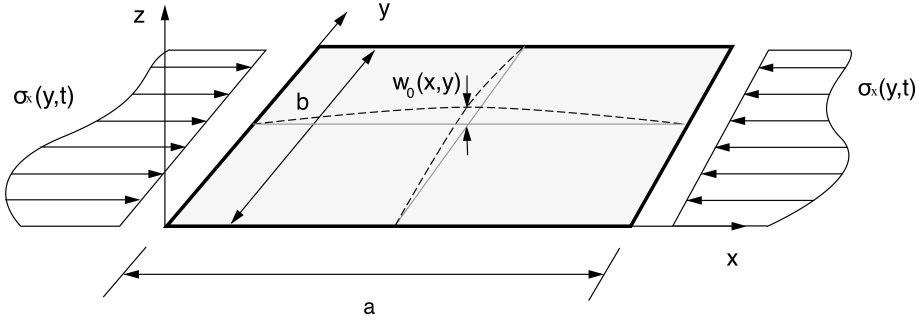


Figure 2.1: A rectangular plate with compressive loading

$$\varepsilon_x = \frac{\partial u}{\partial x} + \frac{1}{2} \left(\frac{\partial w}{\partial x} \right)^2 - \frac{1}{2} \left(\frac{\partial w_0}{\partial x} \right)^2 \quad (2.1a)$$

$$\varepsilon_y = \frac{\partial v}{\partial y} + \frac{1}{2} \left(\frac{\partial w}{\partial y} \right)^2 - \frac{1}{2} \left(\frac{\partial w_0}{\partial y} \right)^2 \quad (2.1b)$$

$$\gamma_{xy} = \frac{\partial u}{\partial y} + \frac{\partial v}{\partial x} + \frac{1}{2} \left(\frac{\partial w}{\partial x} \frac{\partial w}{\partial y} \right) - \frac{1}{2} \left(\frac{\partial w_0}{\partial x} \frac{\partial w_0}{\partial y} \right) \quad (2.1c)$$

The strains in x- and y-direction are ε_x and ε_y respectively, and γ_{xy} is the in plane shear strain. Now the lateral displacement is described by $w(x, y, t)$. The displacement in x-direction is $u(x, y, t)$ and the displacement in y-direction is $v(x, y, t)$. The initial imperfection is $w_0(x, y)$. The lateral displacement is defined as the initial imperfections when $t = 0$, so

$$w(t = 0) = w_0 \quad (2.2)$$

The strain in x-direction is used to show the different components of the strain, but the process is similar in y- and shear direction. First a perfect plate without initial imperfection is considered. The first component of the strain is in-plane strain. It consists of both pure axial deformation and bending deformation. The u is defined as

$$u = u(x, y) - z w_{,x}(x, y) \quad (2.3)$$

where z is the position from the neutral axis. The compact notation $w_{,x}$ means the derivative of w with respect to x . The first part is the axial deformation. The pure axial strain becomes

$$\varepsilon_a = \frac{\partial u}{\partial x} \quad (2.4)$$

The last part is the bending strain. The deformation in the cross section caused by a lateral displacement, w , and rotation, $w_{,x}$. This is shown in Figure 2.2. The bending strain now becomes

$$\varepsilon_b = -z \frac{\partial^2 w}{\partial x^2} \quad (2.5)$$

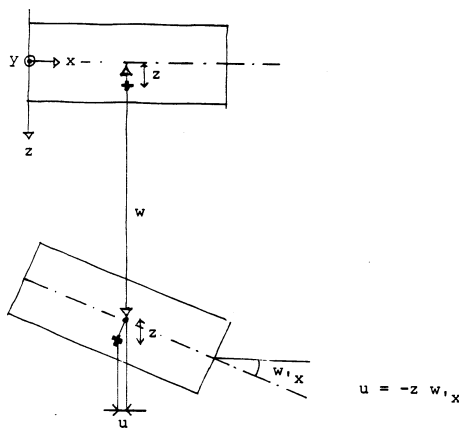


Figure 2.2: Geometric description of bending deformation

The second and third component of Equation (2.1a) is the second order membrane strain from out of plane displacements with the effects of initial deflection. Figure 2.3 shows the length ds for a rotated differential element in x -direction. The element goes from its initial configuration, dx , to the new configuration, ds , and gets longer. Equation (2.6) shows the derivation of ds . Using the definition of strain, the membrane strain has the expression shown in Equation (2.7).

$$ds = \left[1 + \left(\frac{\partial w}{\partial x} \right)^2 \right]^{1/2} dx \approx \left[1 + \frac{1}{2} \left(\frac{\partial w}{\partial x} \right)^2 \right] dx \quad (2.6)$$

$$\varepsilon_m = \frac{ds - dx}{dx} \approx \frac{1}{2} \left(\frac{\partial w}{\partial x} \right)^2 \quad (2.7)$$

If the initial imperfection is accounted for, the infinitesimal element goes from the configuration $ds_0 \approx [1 + \frac{1}{2}w_{0,x}^2] dx$ to ds in Equation (2.6). The membrane strain can be approximated to

$$\varepsilon_m = \frac{ds - ds_0}{ds_0} \approx \frac{1}{2} \left(\frac{\partial w}{\partial x} \right)^2 - \frac{1}{2} \left(\frac{\partial w_0}{\partial x} \right)^2 \quad (2.8)$$

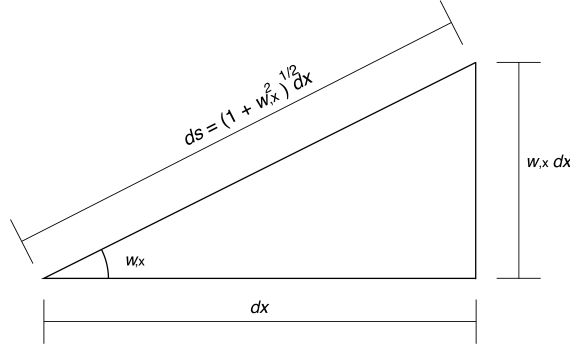


Figure 2.3: Geometric description of membrane deformation

Adding the different strains together and the total strain becomes the expression in Equation (2.1a). Repeating similar derivations in y-direction and for the shear strains and the whole Equation (2.1) gets derived.

Using Hooke's law for isotropic materials the relationship between stresses and strains are

$$\begin{bmatrix} \sigma_x \\ \sigma_y \\ \tau_{xy} \end{bmatrix} = \frac{E}{1 - \nu^2} \begin{bmatrix} 1 & \nu & 0 \\ \nu & 1 & 0 \\ 0 & 0 & \frac{1-\nu}{2} \end{bmatrix} \begin{bmatrix} \varepsilon_x \\ \varepsilon_y \\ \gamma_{xy} \end{bmatrix} \quad (2.9)$$

The parameters E and ν express the Young's modulus and the Poisson's ratio respectively. This is often called the plate flexural rigidity.

The kinematic compatibility equation expresses the relation between the strains in different directions. The nonlinear kinematic compatibility equilibrium states

$$\frac{\partial^2 \varepsilon_x}{\partial y^2} + \frac{\partial^2 \varepsilon_y}{\partial x^2} - \frac{\partial^2 \gamma_{xy}}{\partial x \partial y} = \left(\frac{\partial^2 w}{\partial x \partial y} \right)^2 - \frac{\partial^2 w}{\partial y^2} \frac{\partial^2 w}{\partial x^2} - \left[\left(\frac{\partial^2 w_0}{\partial x \partial y} \right)^2 - \frac{\partial^2 w_0}{\partial y^2} \frac{\partial^2 w_0}{\partial x^2} \right] \quad (2.10)$$

Airy's stress function Φ , as seen in Leira [2011, chap. 4], is defined as

$$\sigma_x = \frac{\partial^2 \Phi}{\partial y^2}, \quad \sigma_y = \frac{\partial^2 \Phi}{\partial x^2}, \quad \tau_{xy} = \frac{\partial^2 \Phi}{\partial x \partial y} \quad (2.11)$$

Using Equation (2.9) and (2.11) in Equation (2.10) the kinematic compatibility becomes

$$\begin{aligned} & \frac{1}{E} \left(\frac{\partial^4 \Phi}{\partial x^4} + 2 \frac{\partial^4 \Phi}{\partial x^2 \partial y^2} + \frac{\partial^4 \Phi}{\partial y^4} \right) \\ &= \left(\frac{\partial^2 w}{\partial x \partial y} \right)^2 - \frac{\partial^2 w}{\partial y^2} \frac{\partial^2 w}{\partial x^2} - \left(\frac{\partial^2 w_0}{\partial x \partial y} \right)^2 + \frac{\partial^2 w_0}{\partial y^2} \frac{\partial^2 w_0}{\partial x^2} \end{aligned} \quad (2.12)$$

The plate differential equation can also be found using Airy's stress function [Ekstrom, 1973].

$$\begin{aligned} & \frac{Eh^3}{12(1-\nu^2)} \left(\frac{\partial^4(w-w_0)}{\partial x^4} + 2 \frac{\partial^4(w-w_0)}{\partial x^2 \partial y^2} + \frac{\partial^4(w-w_0)}{\partial y^4} \right) = \\ & h \left[\frac{\partial^2 w}{\partial x^2} \frac{\partial^2 \Phi}{\partial y^2} - 2 \frac{\partial^2 w}{\partial x \partial y} \frac{\partial^2 \Phi}{\partial x \partial y} + \frac{\partial^2 w}{\partial y^2} \frac{\partial^2 \Phi}{\partial x^2} - \rho \frac{\partial^2 w}{\partial t^2} \right] \end{aligned} \quad (2.13)$$

where h is the plate thickness and ρ is the material density.

Since the plate is assumed simply supported along the edges, the boundary conditions that w and w_0 has to fulfill are

$$\left. \begin{aligned} w = w_0 = 0 \\ \frac{\partial^2 w}{\partial x^2} = \frac{\partial^2 w_0}{\partial x^2} = 0 \end{aligned} \right\} x = 0 \text{ and } x = a \quad (2.14)$$

and

$$\left. \begin{aligned} w = w_0 = 0 \\ \frac{\partial^2 w}{\partial x^2} = \frac{\partial^2 w_0}{\partial x^2} = 0 \end{aligned} \right\} y = 0 \text{ and } y = b \quad (2.15)$$

A lateral displacement that fulfill these conditions are

$$w_{nm}(x, y, t) = f_{nm}(t) \sin\left(\frac{m\pi}{a}x\right) \sin\left(\frac{n\pi}{b}y\right) \quad (2.16)$$

The same will be the case for the initial displacement

$$w_{0,nm}(x, y) = f_{0,nm} \sin\left(\frac{m\pi}{a}x\right) \sin\left(\frac{n\pi}{b}y\right) \quad (2.17)$$

The initial conditions for $f_{nm}(t)$ are

$$\left. \begin{aligned} f_{nm} &= f_{0,nm} \\ \frac{\partial}{\partial t}(f_{nm}) &= 0 \end{aligned} \right\} \text{ for } t = 0 \quad (2.18)$$

From looking at Figure 2.1 the average stress in each direction becomes

$$\frac{1}{b} \int_0^b \sigma_x dy = \frac{1}{b} \int_0^b \frac{\partial^2 \Phi}{\partial y^2} dy = -p(t) \quad (2.19)$$

for $x = 0$ and $x = a$. $p(t)$ is the average compressive stress.

$$\frac{1}{a} \int_0^a \sigma_y dx = \frac{1}{a} \int_0^a \frac{\partial^2 \Phi}{\partial x^2} dx = 0 \quad (2.20)$$

for $y = 0$ and $y = b$.

Using these equations, Ekstrom [1973] got the equation of motion of the plate to be

$$\begin{aligned} \frac{Eh^3}{12(1-\nu^2)} \frac{\pi^4}{h} \left[\frac{m^4}{a^4} + 2\frac{m^2n^2}{a^2b^2} + \frac{n^4}{b^4} \right] (f_{nm}(t) - f_{0,nm}) = \\ \frac{m^2\pi^2}{a^2} p(t) f_{mn}(t) - \rho \frac{\partial^2 f_{mn}(t)}{\partial t^2} + E \frac{\pi^4}{8} \left[\frac{m^4}{a^4} \cos \frac{2\pi n}{b} y \right. \\ \left. + \frac{n^4}{b^4} \cos \frac{2\pi m}{a} x \right] (f_{nm}(t)^2 - f_{0,nm}^2) f_{mn}(t) \quad (2.21) \end{aligned}$$

This expression depends on both x and y . This means that only an approximate solution can be found for the buckling problem. By applying the Galerkin method to Equation (2.21), Ekstrom found an approximated expression. By multiplying each term with $\sin(mx/a) \sin(ny/b) dx dy$ and integrating over the middle surface, the expression becomes

$$\begin{aligned} \rho \frac{\partial^2 f}{\partial t^2} + \frac{Eh^3}{12(1-\nu^2)} \frac{\pi^4}{h} \left[\frac{m^4}{a^4} + 2\frac{m^2n^2}{a^2b^2} + \frac{n^4}{b^4} \right] (f_{nm}(t) - f_{0,nm}) - \\ \frac{m^2\pi^2}{a^2} p(t) f_{mn}(t) + E \frac{\pi^4}{24} \left[\frac{m^4}{a^4} + \frac{n^4}{b^4} \right] (f_{nm}(t)^2 - f_{0,nm}^2) f_{mn}(t) = 0 \quad (2.22) \end{aligned}$$

The solution to this second order differential equation will depend on what assumptions are made for $p(t)$.

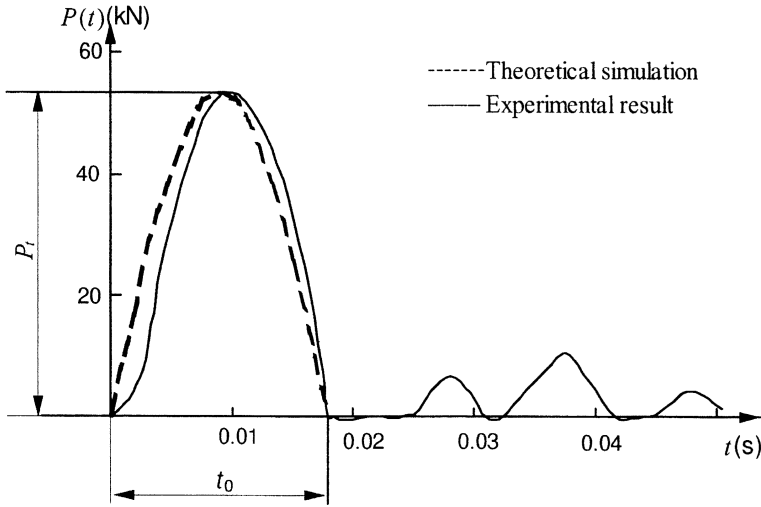


Figure 2.4: A typical axial slamming load time history

From experimental studies done by Cui et al. [1999] show that loading during fluid-solid interaction can be idealized to a half-sine wave. Figure 2.4 show that this is a good approximation. This is typical a slamming load from waves. The loading pressure can be described as

$$p(t) = \begin{cases} p_0 \sin \frac{\pi}{t_0} t & 0 \leq t \leq t_0 \\ 0 & t > t_0 \end{cases} \quad (2.23)$$

The solution of the second order differential equation now becomes very hard to solve analytically and numerical solution methods must be used. In another paper Cui et al. [2001] used finite element method to solve for the lateral displacement. For large loads, the plate will buckle before the sine wave reaches its loading peak. This means that the loading can be approximated to an axial load that increases linearly with time. Ekstrom [1973] proposes this load history. The loading pressure can therefore be written as:

$$p(t) = \begin{cases} \frac{p_0}{t_0} t & 0 \leq t \leq t_0 \\ 0 & t > t_0 \end{cases} \quad (2.24)$$

Also here the solution must be found numerically. The solution found by Ekstrom [1973] is for a rectangular orthotropic plate, but can be specialized to an isotropic plate.

Ekstrom [1973] proposes another way to simulate a dynamic impact. The assumption is that the end of the plate will be displaced with a constant velocity. The solution to this buckling case is also needed to be solved numerically.

To solve the second assumption, a relationship between the stress in axial direction and the in-plane displacements have to be derived. Using Equation (2.10) and Equation (2.1), and solving for $\partial u/\partial x$, the expression becomes

$$\frac{\partial u}{\partial x} = -\pi^2 \left[\frac{m^2}{8a^2} \left(1 + \cos \frac{2\pi m}{a} x - \cos \frac{2\pi m}{a} x \cos \frac{2\pi n}{a} y \right) - \nu \frac{n^2}{8b^2} \cos \frac{2\pi m}{a} x \right] (f_{nm}(t)^2 - f_{0,nm}^2) - \frac{p(t)}{E} \quad (2.25)$$

Integrating over the plate length, a , gives the total relative edge displacement in x-direction

$$u = -\frac{m^2\pi^2}{8a} (f_{nm}(t)^2 - f_{0,nm}^2) - \frac{p(t)a}{E} \quad (2.26)$$

Similarly the total relative edge displacement in y-direction can be found

$$v = -\frac{n^2\pi^2}{8b} (f_{nm}(t)^2 - f_{0,nm}^2) + \nu \frac{p(t)b}{E} \quad (2.27)$$

Now the assumption that the end of the plate is displaced with a constant velocity can be expressed by the average compressive stress in the plate:

$$p(t) = -\frac{E}{a} \left[\frac{m^2\pi^2}{8a} (f_{nm}(t)^2 - f_{0,nm}^2) - \dot{u}_0 t \right] \quad (2.28)$$

where \dot{u}_0 is the constant velocity of the end of the plate. The compact notation \dot{u}_0 means that u_0 is derived with respect to the time, t .

The result for all the different loading approximation was that the dynamic buckling load was larger than the static buckling load. The solution from Cui et al. [2001] and Ekstrom [1973] are both relevant for buckling of marine structures. The sinusoidal and the linearly increasing load can be used to simulate a slamming load on the structure. The displacement of the end will be a good approximation when simulating collisions with objects with large mass.

2.2 Numerical time integration

A MATLAB program was written to solve the dynamic buckling problem. The program took basis in Ekstrom [1973]'s theory, described in Section 2.1.

The lateral displacement was found by numerical time integration. The methods were found in Larsen [2012]. It was first proposed to solve the time integration with an implicit method. Constant average acceleration method was chosen. This method assumes the acceleration is constant over the time step, and the average of the previous and following acceleration step. The acceleration over the time step is expressed in Equation (2.29a) and seen in Figure 2.5.

$$\ddot{f}_{nm}(t) = \frac{1}{2} (\ddot{f}_{nm_i} + \ddot{f}_{nm_{i+1}}) \quad (2.29a)$$

$$\dot{f}_{nm_{i+1}} = \dot{f}_{nm_i} + \frac{dt}{2} (\ddot{f}_{nm_i} + \ddot{f}_{nm_{i+1}}) \quad (2.29b)$$

$$f_{nm_{i+1}} = f_{nm_i} + dt \dot{f}_{nm_i} + \frac{dt^2}{4} (\ddot{f}_{nm_i} + \ddot{f}_{nm_{i+1}}) \quad (2.29c)$$

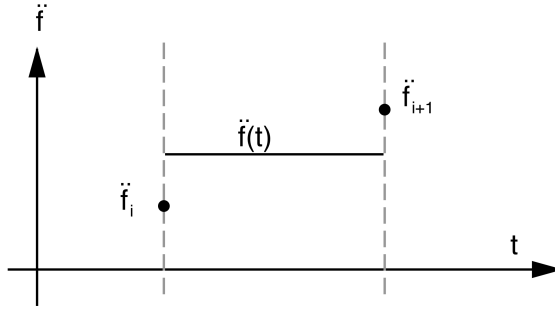


Figure 2.5: Constant average acceleration method

The velocity and displacement is shown in Equation (2.29b) and (2.29c) respectively. They are found by Taylor series expansion of the velocity and displacement function. The f_{nm} is the lateral displacement amplitude for buckling mode m over the length, and n over the width. So the problem is solved independent of the spacial coordinates. The connection between f_{nm} and w is shown in Equation (2.16).

The approximate equation of motion (Equation (2.22)) for time step, $i+1$, is stated in Equation (2.30).

$$\begin{aligned} \rho \ddot{f}_{nm_{i+1}} + \frac{Eh^3}{12(1-\nu^2)} \frac{\pi^4}{h} \left[\frac{m^4}{a^4} + 2 \frac{m^2 n^2}{a^2 b^2} + \frac{n^4}{b^4} \right] (f_{nm_{i+1}} - f_{0,nm}) - \\ \frac{m^2 \pi^2}{a^2} p_{i+1} f_{nm_{i+1}} + E \frac{\pi^4}{24} \left[\frac{m^4}{a^4} + \frac{n^4}{b^4} \right] (f_{nm_{i+1}}^2 - f_{0,nm}^2) f_{nm_{i+1}} = 0 \quad (2.30) \end{aligned}$$

Combining the Equations (2.29) and (2.30) an expression for $f_{nm_{i+1}}$ can be found. The benefit of this solution is that it is unconditionally stable for every time step. It is also an accurate method. The only requirement for the time increment is the accuracy of the solution. It is therefore probably the most used time integration method [Larsen, 2012]. A more general form of the constant time integration is called the Newmark- β method, were the time steps are weighted with different factors.

However, the differential equation that is solved is nonlinear. The lateral displacement has up to third order parts in the equation. This makes it very hard to solve the numerical integration by implicit methods. To solve the equation, the terms could be linearized between two time steps (described in Section 2.3.1). Another method is to iterate the amplitude, $f_{nm_{i+1}}$. These solution would make the MATLAB-code very complicated. To keep the code simple, an explicit time integration method was used.

The Euler method (constant initial acceleration) was chosen as the explicit method. This method assumes that the acceleration of the lateral displacement is constant between two time steps. The value of this acceleration was assumed to be the acceleration at the beginning of the time interval, see Figure 2.6.

The speed and displacement could now be found by using Taylor series expansion for f_{nm} .

$$\ddot{f}_{nm}(t) = \ddot{f}_{nm_i} \quad (2.31a)$$

$$\dot{f}_{nm_{i+1}} = \dot{f}_{nm_i} + dt\ddot{f}_{nm_i} \quad (2.31b)$$

$$f_{nm_{i+1}} = f_{nm_i} + dt\dot{f}_{nm_i} + \frac{dt^2}{2}\ddot{f}_{nm_i} \quad (2.31c)$$

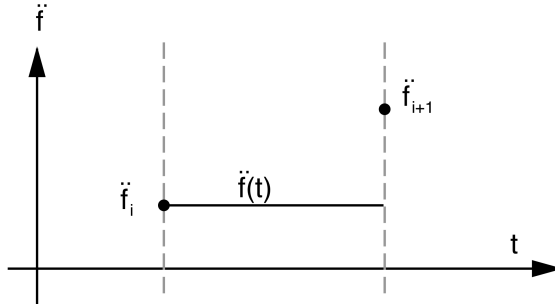


Figure 2.6: Constant initial acceleration method

This method is only conditionally numerically stable and it is also relatively inaccurate compared to the constant average acceleration method. To insure a stable

solution the time increment, dt , has to be smaller than at least half the largest natural frequency of the system [Moan, 2003]. Since the MATLAB program only has one degree of freedom the largest natural frequency has to be the frequency of the assumed buckling mode. Because of the requirement for accuracy, the time increment was chosen so small that the solution always was stable from Equation (2.32). This was verified with convergence tests.

$$dt < \frac{2}{\omega_n} \quad (2.32)$$

By solving Equation (2.30) for the acceleration the expression becomes Equation (2.33).

$$\ddot{f}_{nm_i} = \frac{1}{\rho A} \left\{ -\frac{EAh^2\pi^4}{12(1-\nu^2)} \left[\frac{m^4}{a^4} + 2\frac{m^2n^2}{a^2b^2} + \frac{n^4}{b^4} \right] (f_{nm_i} - f_{0,nm}) + \left[\frac{m^2\pi^2}{a^2} P_i - EA\frac{\pi^4}{24} \left[\frac{m^4}{a^4} + \frac{n^4}{b^4} \right] (f_{nm_i}^2 - f_{0,nm}^2) \right] f_{nm_i} \right\} \quad (2.33)$$

$\dot{f}_{nm_{i+1}}$ and $f_{nm_{i+1}}$ can now be found from the expressions in Equation (2.31). Now the axial force, P , has to be assumed. The program can be modified to account for the different expressions of $P(t)$ discussed earlier in this chapter.

The program takes basis in the assumption that the end of the plate is displaced with a constant velocity. This will be used later in Chapter 4. Since the axial force is the result of the displacement of the plate end, a connection between the two has to be found. In Section 2.1 the relationship between the average compressive stress and end displacement for plates was found in Equation (2.28). This can be converted to a relationship between the axial force and end displacement for a plate, shown in Equation (2.34).

$$P_i = -\frac{EA}{a} \left[\frac{m^2\pi^2}{8a} (f_{nm_i}^2 - f_{0,nm}^2) - \dot{u}_0 t_i \right] \quad (2.34)$$

This can now be used in the expressions in Equation (2.33). The MATLAB-code of this solution method is attached in Appendix A.1.

2.3 Finite element formulation

To reproduce the dynamic buckling phenomena finite element formulation is a useful tool. A finite element program such as Abaqus FEA or USFOS can be used. A model of the plate is created and divided into several elements. The elements are discretized into nodes, and interpolation functions, or shape functions, that describe

the connection between node displacement and displacement of the element. The displacements are then related to strain of the elements and the stress distribution of the plate is found.

The displacement is now formulated as node displacement and interpolation functions, and can be written as

$$u(x, y) = \mathbf{N}_u(x, y)\mathbf{v}_u \quad (2.35a)$$

$$v(x, y) = \mathbf{N}_v(x, y)\mathbf{v}_v \quad (2.35b)$$

$$w(x, y) = \mathbf{N}_w(x, y)\mathbf{v}_w \quad (2.35c)$$

where \mathbf{N} is a vector of the shape functions of the displacements, and \mathbf{v} is the nodal displacement vector for one element.

2.3.1 Dynamic formulation

As the dynamic effects are taken into consideration the problem gets effects from inertia and damping forces. The problem goes can be described by a general equation of motion seen in Equation (2.36).

$$\mathbf{M}\ddot{\mathbf{r}} + \mathbf{C}\dot{\mathbf{r}} + \mathbf{K}\mathbf{r} = \mathbf{R} \quad (2.36)$$

\mathbf{r} is here the global node vector and \mathbf{R} is the global load vector.

The inertia part of the equation can reasonably be assumed constant. This means that the mass matrix, \mathbf{M} , is independent of the displacements. However, the damping matrix, \mathbf{C} , and stiffness matrix, \mathbf{K} , cannot be assumed constant in a dynamic buckling problem. In Langen and Sigbjörnsson [1979, chap. 8] the solving of non-linear dynamic problems is described.

An incremental solution method is used. Looking at dynamic equilibrium equation (Equation (2.36)) for time step i and $i + 1$

$$\mathbf{M}\ddot{\mathbf{r}}_i + \mathbf{C}_i\dot{\mathbf{r}}_i + \mathbf{K}_i\mathbf{r}_i = \mathbf{R}_i \quad (2.37a)$$

$$\mathbf{M}\ddot{\mathbf{r}}_{i+1} + \mathbf{C}_{i+1}\dot{\mathbf{r}}_{i+1} + \mathbf{K}_{i+1}\mathbf{r}_{i+1} = \mathbf{R}_{i+1} \quad (2.37b)$$

Now, subtracting Equation (2.37a) from Equation (2.37b) and the incremental equation of motion becomes

$$\mathbf{M}\Delta\ddot{\mathbf{r}}_i + \mathbf{C}_{Ii}\Delta\dot{\mathbf{r}}_i + \mathbf{K}_{Ii}\Delta\mathbf{r}_i = \Delta\mathbf{R}_i \quad (2.38)$$

where \mathbf{C}_{Ii} and \mathbf{K}_{Ii} is the incremental damping and stiffness matrix respectively. The incremental displacement and force is defined as

$$\Delta \mathbf{r}_i = \mathbf{r}_{i+1} - \mathbf{r}_i \quad (2.39a)$$

$$\Delta \dot{\mathbf{r}}_i = \dot{\mathbf{r}}_{i+1} - \dot{\mathbf{r}}_i \quad (2.39b)$$

$$\Delta \ddot{\mathbf{r}}_i = \ddot{\mathbf{r}}_{i+1} - \ddot{\mathbf{r}}_i \quad (2.39c)$$

and

$$\Delta \mathbf{R}_i = \mathbf{R}_{i+1} - \mathbf{R}_i \quad (2.40)$$

The incremental damping and stiffness matrix is a linearization of \mathbf{C} and \mathbf{K} during the time interval. Ideally the incremental matrices should be the average value of the matrix during the time interval. This is difficult since the displacement and velocity of the next time step is unknown. A more common solution method is using the tangent line at the beginning of the time step as the incremental stiffness and damping. This means that each incremental stiffness and damping entry in the matrix will have the form shown in Equation (2.41) for entry number jk .

$$(c_{jk})_{Ii} = \left(\frac{\partial (c_{jk} \dot{\mathbf{r}}_k)}{\partial \dot{\mathbf{r}}_k} \right)_i \quad (2.41a)$$

$$(k_{jk})_{Ii} = \left(\frac{\partial (k_{jk} \mathbf{r}_k)}{\partial \mathbf{r}_k} \right)_i \quad (2.41b)$$

By solving the Equation (2.38) for time step i we can now find the next time step by solving Equation (2.39) and (2.40) for time step $i + 1$.

Using the tangent line as an approximation of the incremental stiffness and damping will give an error from the exact solution. This error will accumulate for each step. This is shown in Figure 2.7 for a one-dimensional problem. A way to remedy this error is to set up the difference between internal and external loads. This residual load should ideally be zero.

$$\Delta \mathbf{R}_{res,i+1} = \mathbf{R}_{i+1} - (\mathbf{M} \ddot{\mathbf{r}}_{i+1} + \mathbf{C}_{i+1} \dot{\mathbf{r}}_{i+1} + \mathbf{K}_{i+1} \mathbf{r}_{i+1}) \quad (2.42)$$

By introducing the error Δ_i , and iterating the displacement, the expression can be written as

$$\Delta \mathbf{r}_i^{(k)} = \Delta \mathbf{r}_i^{(k-1)} + \Delta_i^{(k)} \quad (2.43)$$

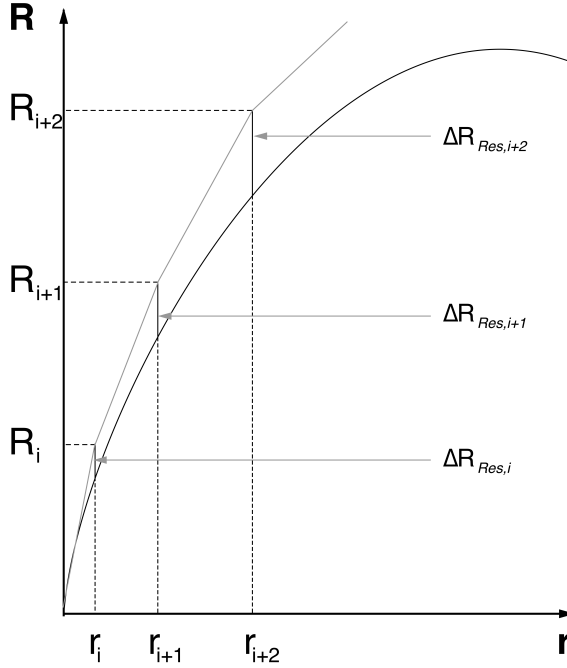


Figure 2.7: Incremental solution of dynamic problem

The total displacement vector for iteration number k will be

$$\mathbf{r}_{i+1}^{(k)} = \mathbf{r}_{i+1}^{(k-1)} + \Delta_i^{(k)} \quad (2.44)$$

Since the last time step do not change during the iteration. The same expression can be found for the velocity and acceleration vector.

The residual force can now be expressed as

$$\mathbf{M}\ddot{\Delta}_i^{(k)} + \mathbf{C}_{Ii}^{(k)}\dot{\Delta}_i^{(k)} + \mathbf{K}_{Ii}^{(k)}\Delta_i^{(k)} = \mathbf{R}_{i+1} - \left(\mathbf{M}\dot{\mathbf{r}}_{i+1}^{(k-1)} + \mathbf{C}_{i+1}^{(k-1)}\dot{\mathbf{r}}_{i+1}^{(k-1)} + \mathbf{K}_{i+1}^{(k-1)}\mathbf{r}_{i+1}^{(k-1)} \right) \quad (2.45)$$

The most frequently used method for iterating the displacement is the Newton-Raphson method. This solves Equation (2.45) until $\Delta^{(k)}$ is smaller than a set error tolerance. The method is illustrated in Figure 2.8 for a one-dimensional case. In the Newton-Raphson method, \mathbf{C}_{Ii} and \mathbf{K}_{Ii} is updated for each iteration step. To save computational time these are often held constant, or updated less often. This is called the modified Newton-Raphson iteration method.

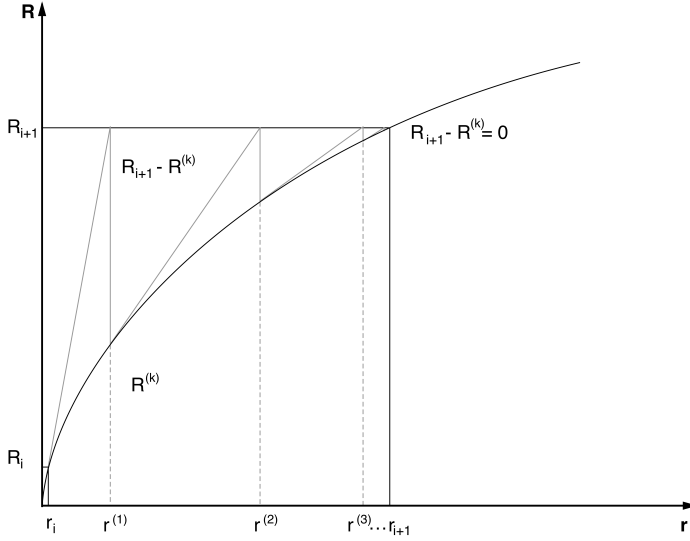


Figure 2.8: Equilibrium iteration with Newton-Raphson method

Equilibrium iteration for every time step is usually very computationally intensive. It is therefore more effective to use smaller time increments combined with equilibrium equation on after a given number of time steps. This has proven to be effective, even for strongly non-linear systems [Langen and Sigbjörnsson, 1979].

The method for numerical time integration can be used for the incremental equation of motion (Equation (2.38)). The dynamic buckling problem can be solved in two ways, either with an implicit or an explicit time integration. These methods have been discussed in Section 2.2. The implicit integration method used is often Newmark- β method. This is a more general case of the average acceleration method. Instead of the average acceleration between the previous and next time step, the time steps are now weighted as seen in Equation (2.46).

$$\Delta \dot{\mathbf{r}}_i = dt \ddot{\mathbf{r}}_i + dt \gamma \Delta \ddot{\mathbf{r}}_i \quad (2.46a)$$

$$\Delta \mathbf{r}_i = dt \dot{\mathbf{r}}_i + \frac{1}{2} dt^2 \ddot{\mathbf{r}}_i + \beta dt^2 \Delta \ddot{\mathbf{r}}_i \quad (2.46b)$$

The γ and β are weighting factors, where $\gamma = \beta = 0$ means that the time integration is only weighted by previous time step, and $\gamma = 1$, $\beta = \frac{1}{2}$ means that the time integration is only weighted by the next time step. Given $\gamma = \frac{1}{2}$, $\beta = \frac{1}{4}$ and the method becomes the constant average acceleration method.

In Abaqus the dynamic analysis can be solved implicit and explicit. For the later analyses the problem is chosen to be solved explicit. The element type used in the analyses is called S4RS. This is based on Belytschko explicit algorithm for nonlinear dynamics of shell element. This is an element suited for dynamic impact type analyses, including buckling behavior. The element is very efficient for cases with small strains, but large rotation and severe bending [Abaqus 6.12 Documentation, 2012]. This will be the case for buckling of plates. The main reason for choosing this method was the benefit of significant reduced computational time over the implicit method.

USFOS uses an implicit time integration method in the dynamic analyses. It utilizes HHT- α method to solve the time integration. This method is based on the Newmark- β method, but have advantages over the standard method. The method employs a time averaging for the damping, stiffness and loading matrix. This introduces artificial damping of higher frequency modes without degrading the accuracy [Søreide et al., 1993].

2.3.2 The stiffness matrix

The stiffness matrix is independent of time, and only dependent on the displacement. This means that to formulate the stiffness matrix for the dynamic buckling problem, the static case can be considered. This way the mass and damping matrices disappears from the equation of motion, and the problem becomes much easier. The problem can now be seen as in Equation (2.47).

$$\mathbf{K}\mathbf{r} = \mathbf{R} \tag{2.47}$$

To be able to reproduce buckling the elements has to be able to describe both membrane stress and bending stress. For a thin plate Kirchhoff plate theory is often used. This means that it is assumed that there is no shear deformation over the thickness of the plate [Moan, 2003]. This is a valid assumption for small strains, which dynamic buckling in most cases is. The plate strains can be described as in Equation (2.1). Using the definitions from Equation (2.35) the strains becomes

$$\begin{aligned} \varepsilon_x = & \mathbf{N}_{u,x} \mathbf{v}_u - z \mathbf{N}_{w,xx} \mathbf{v}_w + \frac{1}{2} \mathbf{v}_w^T \mathbf{N}_{w,x}^T \mathbf{N}_{w,x} \mathbf{v}_w \\ & - \frac{1}{2} \mathbf{v}_{w0}^T \mathbf{N}_{w0,x}^T \mathbf{N}_{w0,x} \mathbf{v}_{w0} \end{aligned} \quad (2.48a)$$

$$\begin{aligned} \varepsilon_y = & \mathbf{N}_{v,y} \mathbf{v}_v - z \mathbf{N}_{w,yy} \mathbf{v}_w + \frac{1}{2} \mathbf{v}_w^T \mathbf{N}_{w,y}^T \mathbf{N}_{w,y} \mathbf{v}_w \\ & - \frac{1}{2} \mathbf{v}_{w0}^T \mathbf{N}_{w0,y}^T \mathbf{N}_{w0,y} \mathbf{v}_{w0} \end{aligned} \quad (2.48b)$$

$$\begin{aligned} \gamma_{xy} = & \mathbf{N}_{u,x} \mathbf{v}_u + \mathbf{N}_{v,y} \mathbf{v}_v - 2z \mathbf{N}_{w,xy} \mathbf{v}_w + \frac{1}{2} \mathbf{v}_w^T \mathbf{N}_{w,x}^T \mathbf{N}_{w,y} \mathbf{v}_w \\ & - \frac{1}{2} \mathbf{v}_{w0}^T \mathbf{N}_{w0,x}^T \mathbf{N}_{w0,y} \mathbf{v}_{w0} \end{aligned} \quad (2.48c)$$

The stiffness formulation can be derived with the basis of the principle of virtual work. The lateral displacements are the important ones for buckling behavior. So the axial strain connected to \mathbf{v}_u and \mathbf{v}_v will express the regular axial stiffness. This expression can be found in Leira [2011]. Looking at virtual work for lateral displacement in Voyiadjis and Woelke [2008, chap. 7]. The internal virtual work for a plate can be described as

$$W_{int} = \int_V \tilde{\boldsymbol{\varepsilon}}^T \boldsymbol{\sigma} dV \quad (2.49)$$

where $\tilde{\boldsymbol{\varepsilon}}$ is the virtual strain of the plate. Using Hooke's law (Equation (2.9)) for expressing $\boldsymbol{\sigma}$ the large displacement matrix can be found. This is derived in Voyiadjis and Woelke [2008, chap. 7]. Essentially the nonlinear stiffness matrix for large displacements can be expressed as

$$\mathbf{K}_0 = \int_A (\mathbf{B}_b^T \mathbf{D}_b \mathbf{B}_b + \mathbf{B}_m^T \mathbf{S} \mathbf{B}_m) dA \quad (2.50)$$

where \mathbf{B}_b and \mathbf{B}_m are the bending strain and membrane strain-displacement matrices respectively. The \mathbf{D}_b and \mathbf{S} are the rigidity matrices for plate bending and stretching respectively.

The virtual external work done on the plate can be expressed as

$$W_{ext} = \int_A \begin{bmatrix} \tilde{w}'_{,x} & \tilde{w}'_{,y} \end{bmatrix} \begin{bmatrix} N_x & N_{xy} \\ N_{yx} & N_y \end{bmatrix} \begin{bmatrix} \tilde{w}'_{,x} \\ \tilde{w}'_{,y} \end{bmatrix} dA \quad (2.51)$$

where N is the in-plane force for the plate. The derivation of this external work takes basis in the one-dimensional example illustrated in Figure 2.9. Given the definition of lateral displacement

$$\begin{bmatrix} w_{,x} \\ w_{,y} \end{bmatrix} = \begin{bmatrix} N_{,x} \\ N_{,y} \end{bmatrix} \mathbf{v}_w = \mathbf{B}_\sigma \mathbf{v}_w \quad (2.52)$$

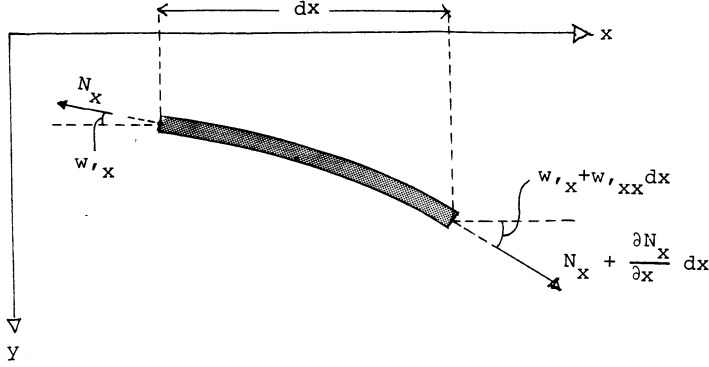


Figure 2.9: In-plane force in x-direction for a plate [Leira, 2011, chap. 6]

The external work now becomes

$$W_{ext} = \tilde{\mathbf{v}}_w^T \left[\int_A \mathbf{B}_\sigma^T \mathbf{G} \mathbf{B}_\sigma dA \right] \mathbf{v}_w \quad (2.53)$$

where

$$\mathbf{G} = \begin{bmatrix} N_x & N_{xy} \\ N_{xy} & N_y \end{bmatrix} \quad (2.54)$$

The derivation of the geometric stiffness, shown in Voyiadjis and Woelke [2008], becomes

$$\mathbf{K}_\sigma = \int \mathbf{B}_\sigma^T \mathbf{G} \mathbf{B}_\sigma dA \quad (2.55)$$

Combining the stiffness matrix for large displacements and the geometric stiffness, the total stiffness for lateral displacements becomes

$$\mathbf{K} = \mathbf{K}_0 + \mathbf{K}_\sigma \quad (2.56)$$

This stiffness matrix is set to a total stiffness matrix, with axial stiffness included, and as mentioned earlier, often linearized to a incremental stiffness matrix.

2.3.3 The damping matrix

Damping is often difficult to find physical values for. Damping from external effect is often represented in the viscous damping. In marine structures this is in most cases water. It could also be from air, but this is often disregarded because of the relative small effect. The viscous damping is often seen as linearly dependent on the velocity of the system. This makes the differential equation for the displacement easier to solve, and the solution is good enough. The damping force is often written as in Equation (2.57).

$$\mathbf{F}^d = \mathbf{C}\dot{\mathbf{r}} \quad (2.57)$$

In many cases the linear damping model is not good enough. With large deformations in a short time span, as with buckling, the viscous damping force has to be modeled nonlinear. A nonlinear model for viscous damping is often assumed as a damping force proportional to the velocity squared. A one-dimensional case is shown in Equation (2.58)

$$F_{NL}^d = c_N |\dot{w}| \dot{w} \quad (2.58)$$

where the damping coefficient, c_N , is found depending on the problem described. For computational reasons the damping is often linearized to an equivalent viscous damping with the form shown in Equation (2.57). This method is described by Langen and Sigbjörnsson [1979]. The energy loss from damping during one cycle of the motion is found for the nonlinear model. This energy loss is now set equal to the energy loss with a linear damping force and an equivalent damping coefficient. For a one-dimensional case with a sinusoidal motion the energy loss becomes

$$W_d = \oint F_{NL}^d dw = \frac{8}{3} c_N \omega^2 w_A^3 = \pi c_{eq} \omega w_A^2 \quad (2.59)$$

where ω is the frequency of the motion, and w_A is the displacement amplitude. The equivalent damping coefficient, c_{eq} , now becomes

$$c_{eq} = \frac{8}{3\pi} c_N \omega w_A \quad (2.60)$$

For the example above the equivalent damping coefficient is dependent on the amplitude of the displacement. For non-cyclic displacements, e.g., impact scenarios, the damping coefficient will also be dependent on the displacement and have to be updated during the analysis.

Other damping effects that are often included in dynamic buckling problems are structural damping. This damping effect is difficult to find good basis for the

chosen values. It is therefore common to assume the structural damping is linearly dependent by a combination of the mass and stiffness matrix. This is called Rayleigh damping and is shown in Equation (2.61).

$$\mathbf{C} = \alpha_0 \mathbf{M} + \alpha_1 \mathbf{K} \quad (2.61)$$

where α_0 and α_1 are factors giving weight to the mass and stiffness matrix respectively. This method makes the damping effect easy to find since the damping matrix is found when the mass and stiffness matrix are known.

$$\lambda = \frac{c}{2m\omega} = \frac{1}{2} \left(\frac{\alpha_0}{\omega} + \alpha_1 \omega \right) \quad (2.62)$$

Looking at a one-dimensional case, the damping ratio becomes Equation (2.62). The α_0 and α_1 are often set by finding what the damping ratio should be at given frequencies. As seen in Figure 2.10 the mass proportional part of the damping ratio is dominating for low frequencies while the stiffness proportional part is dominating for high frequencies. For dynamic impact scenarios the stiffness part will be the most important damping contribution. The mass proportional part is more important for rigid body motions.

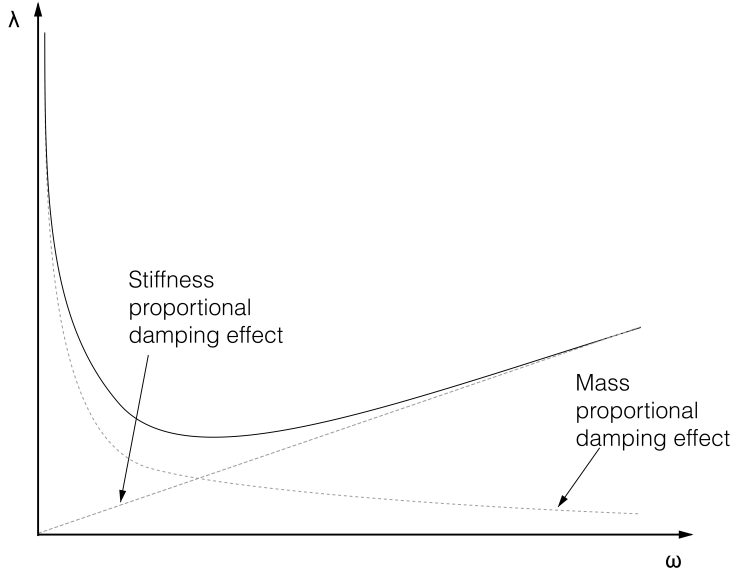


Figure 2.10: Rayleigh damping given as a function of frequency

The Rayleigh damping method can be generalized to a Caughey series with as many damping weight factors as needed. The damping matrix with N weight factors becomes

$$\mathbf{C} = \sum_{k=0}^N \alpha_k \mathbf{M} (\mathbf{M}^{-1} \mathbf{K})^k \quad (2.63)$$

The first two terms becomes the Rayleigh damping. The number of terms accounted for in the analyses is dependent on known modal shapes and the value of α_k are gathered from available damping data.

Chapter 3

Dynamic buckling of simple beam

Beams and columns in marine structures are often designed to take compressive loads. In this chapter the governing parameters for elastic dynamic buckling is presented. A more in-depth look of the theory governing dynamic buckling of beam-columns is presented in Straume [2013].

3.1 Analytical formulation

When looking at rapid varying axial loading of an imperfect beam dynamic effects becomes important. The lateral motion of the beam can be described by

$$EI \frac{\partial^4 w(x, t)}{\partial x^4} + P(t) \frac{\partial^2}{\partial x^2} (w(x, t) + w_0(x)) + \rho A \frac{\partial^2 w(x, t)}{\partial t^2} = 0 \quad (3.1)$$

where EI is the bending stiffness, ρA is the axially distributed mass and t is time. As seen from Figure 3.1, $w_0(x)$ is the initial lateral displacement, $P(t)$ is the axial force, $w(x, t)$ is the lateral displacement and x is the axial coordinate relative to the beam. Unlike Chapter 2 the lateral displacement is described as

$$w(t = 0) = 0 \quad (3.2)$$

and the total deflection is the sum of initial and the current deflection.

The boundary condition of the bar can be expressed by

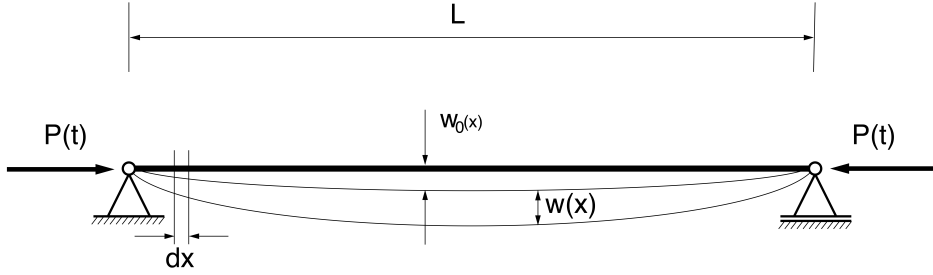


Figure 3.1: Simple bar with initial imperfections and axial loading

$$\left. \begin{aligned} w = w_0 = 0 \\ \frac{\partial^2 w}{\partial x^2} = \frac{\partial^2 w_0}{\partial x^2} = 0 \end{aligned} \right\} \text{ for } x = 0 \text{ and } x = L \quad (3.3)$$

If the lateral displacement is assumed to be from mode number n , a function that fulfill the boundary conditions from Equation (3.3) is

$$w_n(x, t) = f_n(t) \sin\left(\frac{n\pi}{L}x\right) \quad (3.4)$$

The same will be for the initial displacement

$$w_{0,n}(x) = f_{0,n} \sin\left(\frac{n\pi}{L}x\right) \quad (3.5)$$

where $f_n(t)$ is the time-varying amplitude of w_n and $f_{0,n}$ is the amplitude of $w_{0,n}$. Using Equation (3.4) and (3.5) in Equation (3.1) the expression becomes

$$\left\{ f_n(t) \left[EI \left(\frac{n\pi}{L}\right)^2 - P(t) \right] \left(\frac{n\pi}{L}\right)^2 - f_{0,n} \left(\frac{n\pi}{L}\right)^2 P(t) + \frac{\partial^2 f_n(t)}{\partial t^2} \rho A \right\} \sin\left(\frac{n\pi}{L}x\right) = 0 \quad (3.6)$$

It is assumed that the beam is at rest before loading, so the initial conditions for $f_n(t)$ are

$$\left. \begin{aligned} f_n = 0 \\ \frac{\partial}{\partial t}(f_n) = 0 \end{aligned} \right\} \text{ for } t = 0 \quad (3.7)$$

The solution of this equation will depend on the function $P(t)$. The simplest solution, proposed by Lindberg [2003], is a load applied suddenly when $t = 0$ and is constant during loading t_0 . The loading then becomes

$$P(t) = \begin{cases} P_0 & 0 \leq t \leq t_0 \\ 0 & t > t_0 \end{cases} \quad (3.8)$$

P_0 is the load amplitude and t_0 is the duration of the loading. This is a good approximation for impulse type loads. The solution becomes trigonometric and therefore bounded when $P < \left(\frac{n\pi}{L}\right)^2 EI$ and hyperbolic and exponentially growing when $P > \left(\frac{n\pi}{L}\right)^2 EI$. This means that the beam will buckle when the deflection get a hyperbolic solution. When $P = \left(\frac{n\pi}{L}\right)^2 EI$ the solution is a transition between the bounded and the unbounded motion. The solution describes the static Euler buckling load when $n = 1$. This means that the dynamic buckling load will be larger or equal to the static buckling load.

The solution found by Lindberg [2003] is the summation of all buckling modes, and is written as

$$w(\xi, \tau) = \sum_{n=1}^{\infty} \frac{a_n}{1 - \eta^2} \left[\frac{\cosh p_n \tau - 1}{\cos p_n \tau} \right] \sin \frac{n\pi\xi}{L} \quad (3.9)$$

where

$$a_n = \frac{2}{L} \int_0^l w_0(\xi) \sin \frac{n\pi\xi}{L} d\xi \quad (3.10)$$

$\eta = \frac{n\pi}{L}$, $\xi = sx$, $p_n = \eta|1 - \eta^2|^{1/2}$ and $\tau = s^2 ct$. The parameter s is the ratio between the radius of gyration, r , and the Euler wavelength, k . This will give

$$s = rk = \sqrt{\frac{P}{AE}} \quad (3.11)$$

The parameter c is the speed of the stress propagation in the material and can be expressed as

$$c = \sqrt{\frac{E}{\rho}} \quad (3.12)$$

It is assumed that the stress is constant over the beam length for marine structures. This type of impulse load is not very good assumption. The Euler wavelength and stress propagation in the material are relevant for impacts were this is not the case, i.e., impact velocities much larger than what is typical for marine structures. To describe buckling typical for impacts on marine structures the loading has to vary with time.

The assumptions of the loading history discussed in Section 2.1 are also applicable to a beam when looking at a dynamic buckling problem. The loading pressure can be integrated over the cross section of the beam, and be expressed as an axial force. However the solution method is the same. This means that solving the problem numerically is the most suitable.

3.2 Finite element formulation

As with plates, when doing analyses of dynamic buckling of beams, a finite element method is a preferred way to solve the problem. The beam problem is discretized into nodes and elements. Then a FEA program is used to solve the problem. The approach to set up the finite element formulation for a beam is very similar to a plate. The main difference is that the axial displacement is only in one direction, say x-direction, and the lateral displacement can happen in two directions, y- and z-direction. The finite element model used in USFOS will be mainly described. Also here, the updated Lagrange formulation is used.

The strain can now be formulated as

$$\varepsilon_x = u_{,x} + \frac{1}{2}v_{,x}^2 + \frac{1}{2}w_{,x}^2 - yv_{,xx} - zw_{,xx} \quad (3.13)$$

where v and w are the lateral displacement in y- and z-direction respectively. The discretization of a beam element in USFOS uses shape functions as interpolation functions. The displacements can now be written as

The internal strain energy can now be formulated as

$$W_{int} = \frac{1}{2} \int_0^l EA \left(u_{,x} + \frac{1}{2}v_{,x}^2 + \frac{1}{2}w_{,x}^2 \right)^2 dx + \frac{1}{2} \int_0^l (EI_z v_{,xx}^2 + EI_y w_{,xx}^2) dx \quad (3.14)$$

$$u(x) = \phi_u^T \mathbf{q}_u \quad (3.15a)$$

$$v(x) = \phi_v^T \mathbf{q}_v \quad (3.15b)$$

$$w(x) = \phi_w^T \mathbf{q}_w \quad (3.15c)$$

The strain formulated with finite element formulation becomes

$$\varepsilon_x = \phi_{u,x}^T \mathbf{q}_u + \frac{1}{2} \mathbf{q}_v^T \phi_{v,x} \phi_{v,x}^T \mathbf{q}_v + \frac{1}{2} \mathbf{q}_w^T \phi_{w,x} \phi_{w,x}^T \mathbf{q}_w - z \phi_{v,xx}^T \mathbf{q}_v - z \phi_{w,xx}^T \mathbf{q}_w \quad (3.16)$$

The strain energy formulated with displacement vectors and shape functions can be found in Sørense et al. [1993]. Also, the derivation of the variation of increment in external and internal work can also be seen there. From this finite element formulation of energy the stiffness matrix may be derived.

$$\mathbf{K} = \begin{bmatrix} \mathbf{k}_{uu} & \mathbf{k}_{uv} & \mathbf{k}_{uw} \\ \mathbf{k}_{vu} & \mathbf{k}_{vv} & \mathbf{k}_{vw} \\ \mathbf{k}_{wu} & \mathbf{k}_{wv} & \mathbf{k}_{ww} \end{bmatrix} \quad (3.17)$$

The sub-matrices are expressed as

$$\mathbf{k}_{uu} = \int_0^l (EA \phi_{u,x} \phi_{u,x}^T) dx \quad (3.18a)$$

$$\mathbf{k}_{vv} = \int_0^l (EI_z \phi_{v,xx} \phi_{v,xx}^T - N \phi_{v,x} \phi_{v,x}^T + EA \phi_{v,x} v_x^2 \phi_{v,x}^T) dx \quad (3.18b)$$

$$\mathbf{k}_{ww} = \int_0^l (EI_y \phi_{w,xx} \phi_{w,xx}^T - N \phi_{w,x} \phi_{w,x}^T + EA \phi_{w,x} w_x^2 \phi_{w,x}^T) dx \quad (3.18c)$$

$$\mathbf{k}_{vu} = \int_0^l (EA \phi_{v,x} v_x \phi_{u,x}^T) dx = \mathbf{k}_{uv}^T \quad (3.18d)$$

$$\mathbf{k}_{wu} = \int_0^l (EA \phi_{w,x} w_x \phi_{u,x}^T) dx = \mathbf{k}_{uw}^T \quad (3.18e)$$

$$\mathbf{k}_{wv} = \int_0^l (EA \phi_{w,x} w_x v_x \phi_{v,x}^T) dx = \mathbf{k}_{vw}^T \quad (3.18f)$$

The geometrical stiffness is expressed in the matrix in the \mathbf{k}_{vv} and \mathbf{k}_{ww} matrices as the second term, where N is the axial load.

3.2.1 Shape functions

The shape functions between the nodes are taken as the exact solution to the 4th order differential equation for a beam subjected to end forces [Sørense et al., 1993]. This means that the displacements can be expressed by an analytical solution. The

stiffness matrix can now represent the exact load-displacement functions. This means that buckling can be reproduced with very few elements in USFOS. It is often sufficient with one element between each joint in a model. The shape function for displacement in y -direction is shown in Equation (3.19)

$$\phi_v^T = \left[\cos kx \quad \sin kx \quad \frac{x}{l} \quad 1 \right] \quad (3.19a)$$

$$\phi_v^T = \left[e^{kx} \quad e^{-kx} \quad \frac{x}{l} \quad 1 \right] \quad (3.19b)$$

where

$$k^2 = \frac{|N|}{EI_z} \quad (3.20)$$

Equation (3.19a) is used when N is in compression while Equation (3.19b) is used when N is in tension. N is defined positive in compression. Now the constants in \mathbf{q}_v are determined by the boundary conditions for the beam.

Chapter 4

Analysis of unstiffened plates

Buckling of plates is a relevant problem for plates in marine structures. The plates are often load carrying members. These loads can often be compressive which means that buckling could be a relevant problem. During collisions dynamic effects are important, and the capacity of the member could change. Plates are also often exposed to hydrostatic pressure, which means that the plate will have a lateral deflection when the compressive stress is applied. This will make the plate even more exposed to buckling. If the stiffeners around the plate is very strong the plate will buckle before the stiffeners, and buckling of the plate will occur.

To examine the dynamic effects on the buckling capacity a simple unstiffened plate is analyzed in a FEA-program. Both Abaqus FEA and USFOS are used to verify the result. Ekstrom's analytical approach, described in Chapter 2, has also been used to compare with the results of the FEA.

The effect of dynamic buckling for stiffened plates was also considered, but the effect was assumed to be very close to a beam, so the results are not considered here.

4.1 Setup of the analyses

The plate that were examined had the properties as seen in Table 4.1. To simulate that the plate was part of a plate field with stiffeners dividing each plate, some special boundary conditions was applied. The longitudinal edges was able to move freely in x-direction, but was fixed against translation in z-direction. In the y-direction the translation was constrained. This means that the end could move in y-direction, but the end had to be straight. The nodes along the edge could only rotate around the x-axis. The same type of boundary condition was applied on the short end of the plate. The difference was that one of the ends was fixed against translation in x-direction.

Table 4.1: Properties of the unstiffened plate

Properties of the unstiffened plate	
Young's Modulus	211 GPa
Yield stress	255 MPa
Density	7850 kg/m ³
Length	2.4 m
Width	0.8 m
Thickness	10.0 mm
Poisson's ratio	0.3

An initial imperfection was introduced into the coordinates of the nodes. This means that the z-coordinates of the nodes were shifted from their initial values to form a shape of an assumed shape. The shape of the imperfection was taken from Equation (2.17). The amplitude of the initial imperfection is assumed to be $\frac{f_0}{b} = 1.25 \cdot 10^{-3}$ and the number of half-waves across the width, $n = 1$. The number of half-waves in the length direction was different for the different analyses.

The model was created in Abaqus and converted into a USFOS model file. The properties that could not be converted directly were introduced manually. This was, e.g., the constraint condition. This was modeled in USFOS as springs between the edge nodes with very high shear stiffness. In Abaqus this was introduced using an equation-condition. The condition was that all the nodes displacement in y-direction had to be equal. Figure 4.1 shows the equation-condition for one of the longitudinal edges.

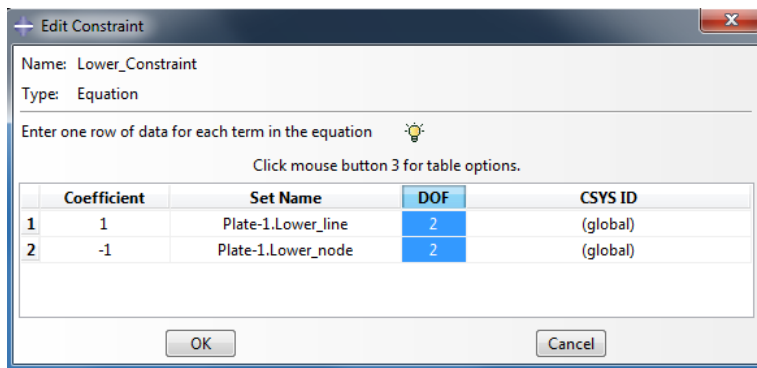


Figure 4.1: The Abaqus equation for the edge constraint

Several different conditions were run. First, the static buckling load for the plate was found. This was used to compare with the dynamic buckling load, and find the capacity change for the plate in a dynamic condition. An eigenfrequency analysis

was also performed on the model. The eigenperiod for the static buckling shape was found, to be used in later analyses.

4.1.1 End displacement analysis

An analysis with a constant velocity edge displacement was done. The short edge of the plate was displaced inwards with a constant velocity, making the plate buckle. This would simulate a buckling condition of the plate during a collision with a large mass. The large mass would be affected negligible of the impact, and continue with a constant velocity. This case was run with different speeds of the end displacement. In the initial analyses, both Abaqus and USFOS were used, and Ekstrom's solution was used to compare the FEM analyses. This method is described in Section 2.2. The speed of the end displacement was varied from 0.1 m/s to 6.5 m/s. The complete list of velocities used in the analysis can be found in Table 4.2.

Table 4.2: Shows the different velocities of the edge

Velocities of edge displacement					
0.10 m/s	0.50 m/s	1.00 m/s	1.50 m/s	2.00 m/s	2.25 m/s
2.50 m/s	2.75 m/s	3.00 m/s	3.25 m/s	3.50 m/s	4.00 m/s
4.50 m/s	5.00 m/s	5.50 m/s	6.00 m/s	6.50 m/s	

For each velocity a number of imperfection shapes were run, to see which imperfection gave the smallest buckling load. The imperfection shapes had one half-wave over the plate width, and the number of half-waves over the length is listed in Table 4.5. To achieve a large number of analyses, with least amount of work, scripting was used. The scripting was done with python scripting. Since Abaqus can be controlled entirely by python code, this program was used in the analyses. An except of the python script can be seen in Appendix A.2. The lateral deflection was found at the displacement were static buckling would have occurred, found in the static analysis.

Table 4.3: Shows the half-waves for imperfection shapes

Number of half-waves								
1	2	3	4	5	6	7	8	9

4.1.2 Axial load analysis

Another type of analysis was run. The end of the plate was exposed to a sinusoidal load history, as seen on Figure 2.4 and described in Equation (2.23). The amplitude

of the load, P_0 , and the duration of the loading, t_0 , was varied. Also in these analyses python scripting was used. This loading history can for example simulate slamming loads that induce buckling. The imperfection shape was assumed to be the same as the static buckling shape, that gives number of half-waves over the length $m = 3$.

The eigenperiod for the static buckling shape was used as basis for the loading duration. The durations used in the analyses are found in Table 4.4. T is the eigenperiod for oscillation for the static buckling shape. These periods were chosen because when $\frac{t_0}{T}$ is smaller than $\frac{1}{2}$, the problem can start behaving like a pure impulse load problem. This means the plate moves very little while the loading occurs, making dynamic effects during loading negligible. When $\frac{t_0}{T}$ is larger than 2, the problem starts behaving like a static problem.

Table 4.4: Shows the different loading periods

Loading durations ($\frac{t_0}{T}$)				
$\frac{1}{2}$	$\frac{2}{3}$	1	$\frac{3}{2}$	2

For each load duration 18 different loading amplitudes were run. The load amplitude was ranged from an amplitude much smaller than the static buckling load to an amplitude that was much larger. This was done so that the capacity change was captured in the analyses. The load amplitudes that were used can also be seen in Table 4.5.

Table 4.5: Shows the different loading amplitudes

Loading amplitudes (P_0)					
$1.0 \cdot 10^5$ N	$2.0 \cdot 10^5$ N	$5.0 \cdot 10^5$ N	$7.0 \cdot 10^5$ N	$9.0 \cdot 10^5$ N	$1.0 \cdot 10^6$ N
$1.5 \cdot 10^6$ N	$2.0 \cdot 10^6$ N	$2.5 \cdot 10^6$ N	$3.0 \cdot 10^6$ N	$3.5 \cdot 10^6$ N	$4.0 \cdot 10^6$ N
$5.0 \cdot 10^6$ N	$6.0 \cdot 10^6$ N	$7.0 \cdot 10^6$ N	$8.0 \cdot 10^6$ N	$9.0 \cdot 10^6$ N	$1.0 \cdot 10^7$ N

After the analyses were done, the maximum deflection of the plate was obtained from the results. The MATLAB-code from Ekstrom [1973]'s solution was adapted to a sinusoidal loading. The result from this code was compared to the Abaqus result.

4.1.3 Elastic-plastic analysis

For many of the results, plasticity would be the limiting factor for the plate capacity. The velocity and the axial load analyses were therefore also run with a yield stress for the plate. The yield stress was set to $\sigma_y = 255$ MPa. This is a typical yield stress for steel used in ship plates.

This would give the force, $P_y = 2.04 \cdot 10^6$ N, that would give yielding with pure axial deformation. The applied loads amplitudes that were above this load were not considered, due to the triviality of the result.

4.2 Result of the analyses

The following results were obtained by the analyses.

4.2.1 Static buckling analysis

The static buckling stress was found using the Equation (4.1) found in Amdahl [2013]. The equation states that

$$\sigma_E = \frac{\pi^2 E}{12(1 - \nu^2)} \left(\frac{h}{b}\right)^2 k \quad (4.1)$$

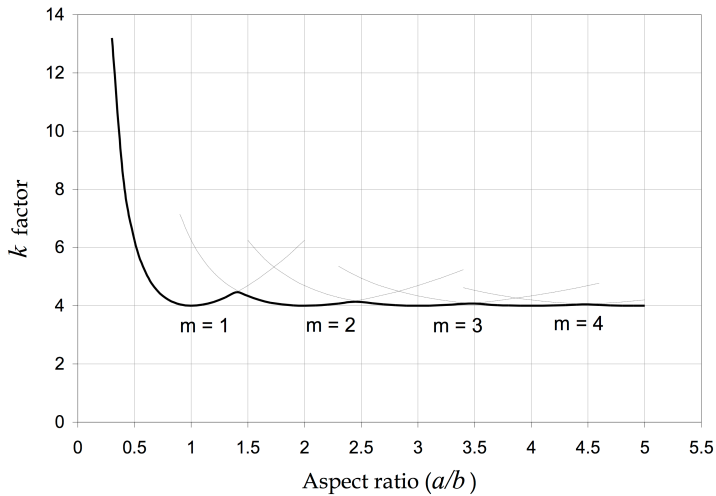


Figure 4.2: Buckling coefficient versus the plate aspect ratio for $n = 1$

where k is the plate buckling coefficient. Figure 4.2 is used to find the value of k . The plate has an aspect ratio of 3, so when assuming that the plate buckles with $n = 1$ and $m = 3$ the coefficient becomes its lowest value, $k = 4$. This gives the static buckling stress as

$$\sigma_E = 119.19 \text{ MPa} \quad (4.2)$$

When multiplying with the cross sectional area, the static buckling load for the plate becomes

$$P_E = \sigma_E \cdot A = 9.54 \cdot 10^5 \text{ N} \quad (4.3)$$

The displacement in x-direction, which would correspond to this buckling load, is found in Equation (4.4). This is for a perfect plate without any lateral displacement before the Euler buckling load.

$$\Delta U = \frac{P_E L}{EA} = 1.36 \text{ mm} \quad (4.4)$$

4.2.2 Eigenfrequency analysis

The eigenfrequency analysis for oscillation of this buckling shape gave the following result

$$T = \frac{1}{f} = \frac{1}{77.015 \text{ s}^{-1}} = 0.012984 \text{ s} \quad (4.5)$$

The eigenperiod was the same in both Abaqus and USFOS analysis. Figure 4.3 shows the shape of the eigenmode plotted in Abaqus.

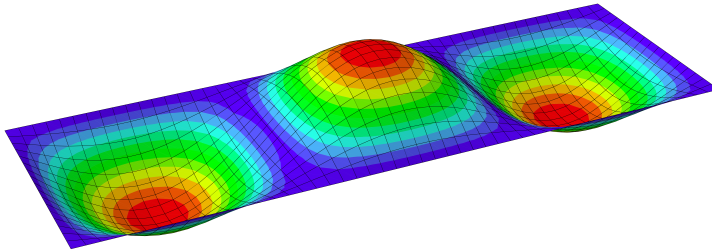


Figure 4.3: The eigenmode shape for the static buckling case

4.2.3 End displacement analysis

The first analysis was done on both USFOS, Abaqus and with the MATLAB-code for Ekstrom's solution. The case was an edge displacement of 5 m/s with an initial

imperfection with 7 half-waves over the length of the plate. The force resultant at the other edge of the beam was plotted against the time of the analysis. The results can be seen in Figure 4.4.

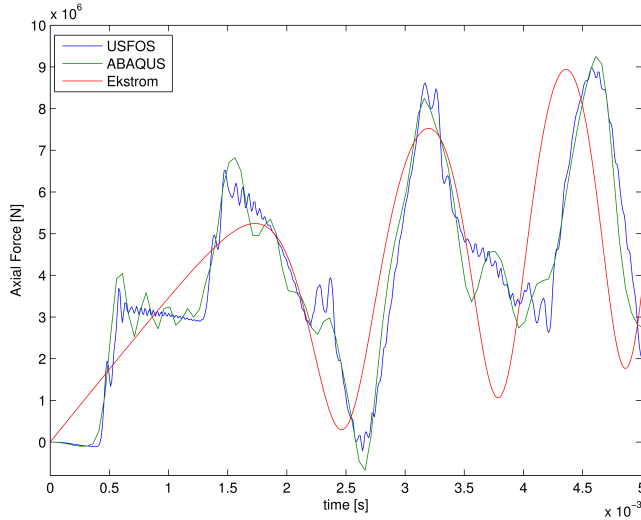


Figure 4.4: Comparison between different analyses of edge displacement, $v = 5$ m/s, $m = 7$

As seen the results coincide well between the different analyses. There are some differences. The stress propagation is not considered in Ekstrom's analysis. There seem to be a slight phase shift between the FEA and the MATLAB-code, and the maxima are somewhat different. There is also a higher order oscillation in the FEA that Ekstrom's solution does not have. USFOS seem to have higher frequency oscillation than Abaqus.

The resultant force for the edge displacement was extracted from the analyses in different ways depending on the program. In Abaqus the resultant force of each element at the plate end was extracted from the result file. Then the forces were summed together to give the total resultant force. In USFOS, two very stiff linear springs was attached at the end of the plate. The small displacement of the springs was multiplied by the stiffness of the springs to get the resultant force. In the MATLAB-code the axial force is found as described in Section 2.2 with Equation (2.34).

Since the force resultant is extracted from the other edge of the plate compared to the edge displacement, the time before the stress reaches the end will be a noticeable occurrence for these small time intervals. This will only be relevant for the FEM-analysis since Ekstrom assumes constant stress over the length of the beam. The speed of stress propagation in steel can be found from Equation (4.6),

which is found in Lindberg [2003]. The time for the stress to propagate to the end of the plate is found in Equation (4.7).

$$c = \sqrt{\frac{E}{\rho}} \quad (4.6)$$

$$t_{\text{plate end}} = \frac{a}{c} = \frac{2.4 \text{ m}}{\sqrt{\frac{211 \text{ GPa}}{7850 \text{ kg/m}^3}}} = 4.63 \cdot 10^{-4} \text{ s} \quad (4.7)$$

Combining this result with a displacement of the plate end, and it can be found for which speeds the displacement will happen faster than for the stress to propagate to the end of the plate. This result can be seen in Equation (4.8).

$$\dot{u}_{\text{lim}} = \frac{\Delta U}{t_{\text{plate end}}} = \frac{1.36 \cdot 10^{-3} \text{ m}}{4.63 \cdot 10^{-4} \text{ s}} = 2.94 \text{ m/s} \quad (4.8)$$

This means that speeds higher than 3 m/s should not have any reaction force when measured at the displacement $\Delta U = 1.36 \text{ mm}$.

The rest of the analyses were done in Abaqus. The resultant force and largest lateral displacement were extracted. The analyses were done with several imperfection shapes to see which effect it had on the result. The different imperfection shape with a speed of 5 m/s is shown in Figure 4.5. The result is very similar for all the other speeds tested.

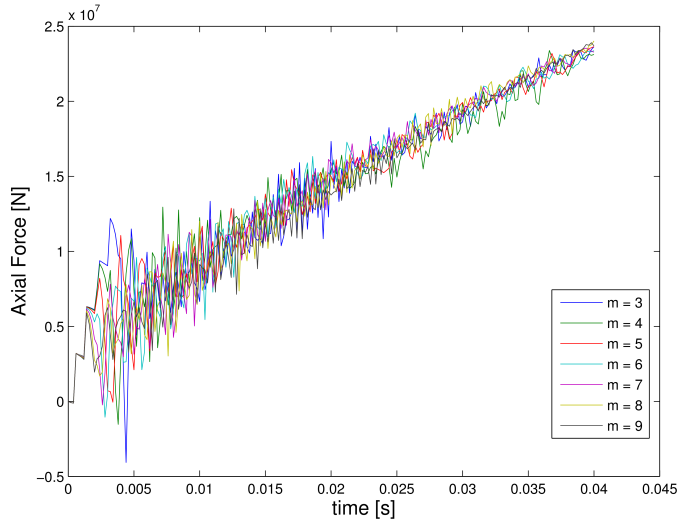


Figure 4.5: Comparison between different imperfection shapes for $v = 5 \text{ m/s}$

Since the assumed number of half-waves in the analysis did not change the resultant force significantly, the rest of the result only one imperfection shape was used. The imperfection shape with 7 half-waves over the length was chosen since many of the analyses buckled in this shape independent of their initial imperfections.

Both maximum lateral deflection and resultant force were extracted when the plate were displaced axially equal to the displacement found in Equation (4.4). These were plotted for the different speeds. The results can be seen in Figure 4.6 and Figure 4.7. The results from an identical case run with Ekstrom's solution is plotted in the same result.

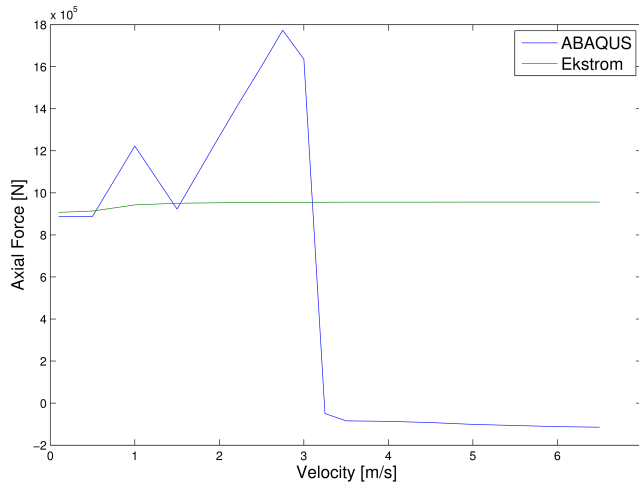


Figure 4.6: Axial force for $m = 7$ at $\Delta U = 1.36$ mm

As the Figure 4.6 shows, the axial force increases with the velocity until the stress propagation does not reach the end of the plate at the given time. Then the stress becomes a constant negative value. The axial force in Ekstrom's solution start with almost the same value as Abaqus, but does not vary nearly as much. The force only increases a little in the beginning.

The lateral displacement, seen in Figure 4.7, is almost identical between Abaqus and Ekstrom. The lateral displacements are becoming relatively large with slow end displacement, and are converging to zero as the velocity increases. The Ekstrom result is converging a little faster than Abaqus. At very slow speed the lateral displacement looks like it is converging to a static value around 0.9 mm.

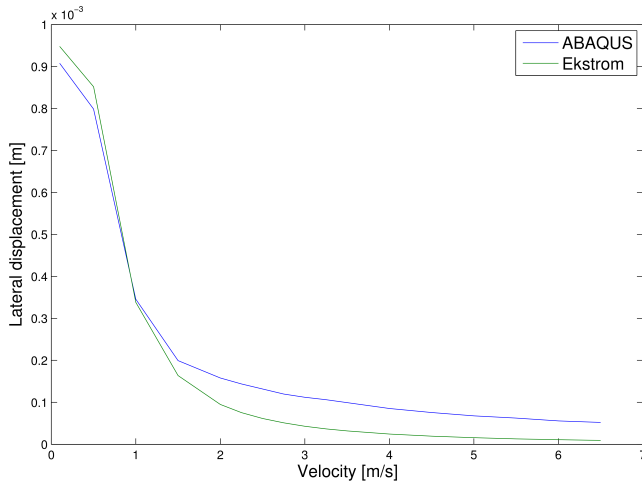


Figure 4.7: Lateral deflection for $m = 7$ at $\Delta U = 1.36$ mm

4.2.4 Axial load analysis

The result from the analyses with axial sinusoidal history can be seen in Figure 4.9. Here is the maximum deflection plotted against the force amplitude of the sinusoidal load. The deformation of the plate for $P_0 = 5.0 \cdot 10^6$ N and $\frac{t_0}{T} = 0.50$ is shown in Figure 4.8. The plate buckles with 3 half-waves, the same as the imperfection. This is the deflection towards the end of the analysis, and the half-waves have about the same amplitude. At the beginning of the analysis the half-waves deflected first close to the loaded edge, so the amplitude of the half-waves varied across the length.

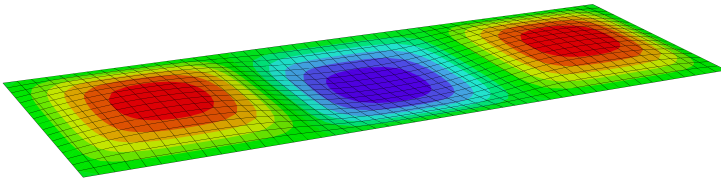


Figure 4.8: Deformation of plate with $P_0 = 5.0 \cdot 10^6$ N and $\frac{t_0}{T} = 0.50$

The general trend is that the longer the duration of loading is, the higher the maximum deflection becomes. As the force amplitude gets very high this trend breaks down.

Figure 4.10 shows the force amplitude and loading duration for fixed maximum deflection. The figure shows that the force amplitude required to get small maxi-

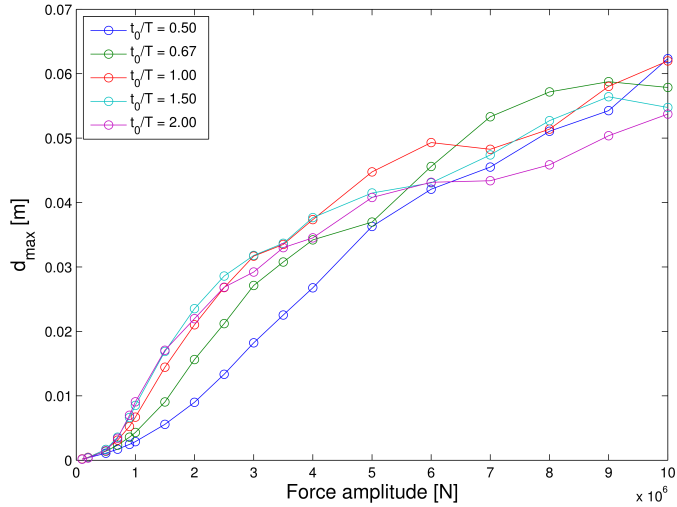


Figure 4.9: Maximum deflection of plate at different force amplitudes

mum deflections, e.g., $d_{max} = 0.001$ m, does not change much for different loading durations. The force amplitude is approximately constant. For large maximum deflections, however, the force amplitude is much more dependent on the loading duration. This can be seen with $d_{max} = 0.020$ m. For small loading durations the force amplitude required to achieve the deflection is much higher than for long durations.

When the loading duration approaches $t_0 = 2T$ the force amplitude becomes approximately constant for all deflections. This indicates that this is the static force amplitude for that deflection. As the loading duration decreases the force amplitude required to laterally deflect the plate increases exponentially. The effect is amplified with large deflections.

The same result is shown in Figure 4.11, but here is the force amplitude held constant while the maximum deflection is plotted against the loading duration. Also here it seems as the maximum deflection converges to a static value, for a given force amplitude, with large loading duration. As the loading duration decreases the maximum deflection does the same. The effect is amplified with higher force amplitudes. It may look like the maximum deflection converges to zero as the loading duration goes to zero.

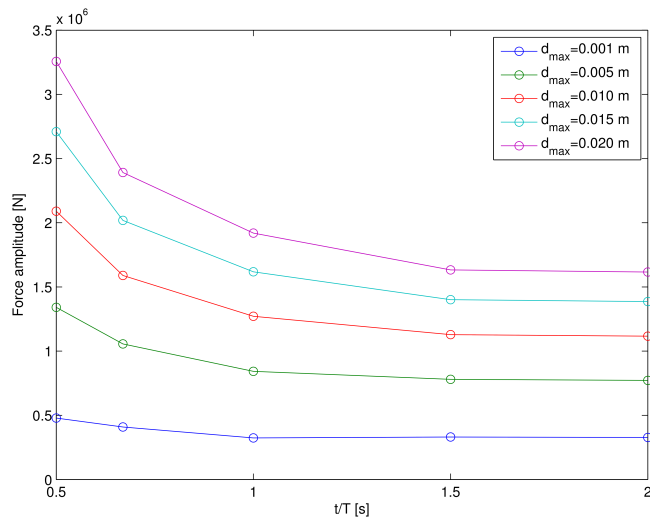


Figure 4.10: Force amplitude at different loading durations at given deflections

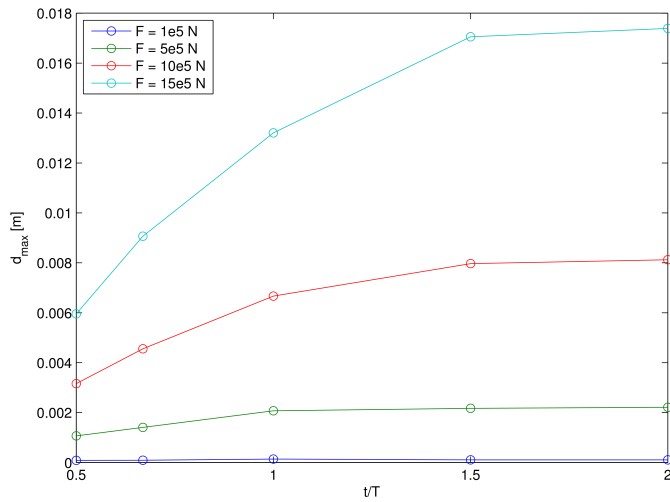


Figure 4.11: Maximum deflection at different loading durations at given force amplitudes

4.2.5 Elastic-plastic analysis

The axial load analysis done in Abaqus, was rerun with a yield stress. Figure 4.12 shows the results plotted as maximum deflection versus the axial load amplitude. The different loading durations is shown as different lines in the plot.

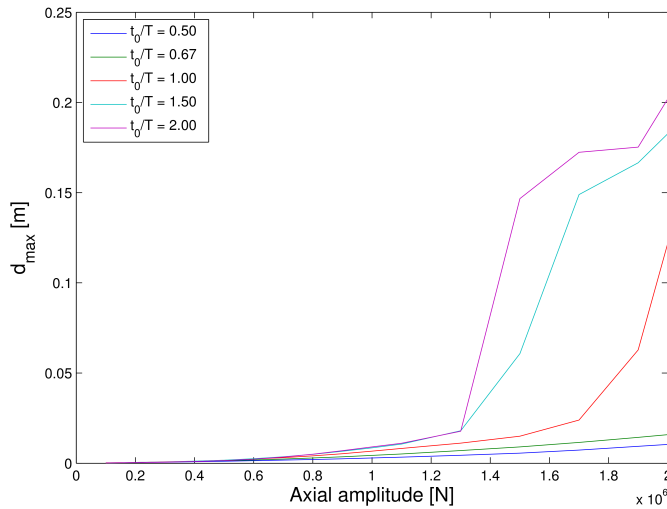


Figure 4.12: Maximum deflection of plate at different force amplitudes, plastic analysis

The fastest applied load did not have any noticeable yielding. The loading periods that were under the eigenperiod had a maximum deflection about the same as the elastic analyses, even up to almost pure axial yielding.

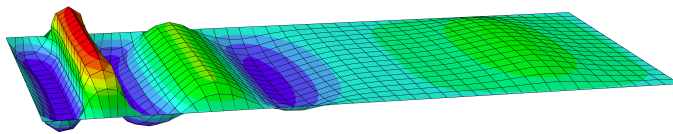


Figure 4.13: Plastic deformation of plate with $P_0 = 1.5 \cdot 10^6$ N and $\frac{t_0}{T} = 2.00$

The loading durations above the eigenperiod began to yield during the analyses. This gave much larger lateral deflections than the elastic analyses. The load amplitude that gave yielding seems to get lower as the loading duration became larger.

Both $\frac{t_0}{T} = 2.00$ and $\frac{t_0}{T} = 1.50$ started to yield after $P_0 = 1.3 \cdot 10^6$ N, while $\frac{t_0}{T} = 2.00$ seem to yield after $P_0 = 1.5 \cdot 10^6$ N.

The plate deformation for $P_0 = 1.5 \cdot 10^6$ N and $\frac{t_0}{T} = 2.00$ when yielded is shown in Figure 4.13. The most noticeable effect in the figure is that the half-waves look very different over the length. Most of the deformation has happened at the end where the loading was applied.

4.3 Discussion of the result

4.3.1 Static buckling and eigenfrequency analysis

Using the equation for static buckling load for perfect plates to get an estimate for the static buckling load. The buckling load became $P_E = 9.54 \cdot 10^5$ N. This would naturally be a little lower if the initial imperfection is taken into account, but when looking for a dynamic loading factor between the static and dynamic buckling, this is a conservative estimate.

The displacement in x-direction that would correspond to the static buckling load is also based on a perfect plate. In that case the only displacement before the plate buckles is in the axial direction. This means that the displacement can be found from a linearly consideration of the stress-strain relationship. This will not be the case for a plate with initial deformations. The plate will be more relaxed, as it can move in the lateral direction, and will have a smaller applied load at the same displacement in x-direction. Even though, this is a good point to extract axial force and lateral deflection as it can be used to compare different velocities.

The eigenfrequency analyses were done both in Abaqus and USFOS. They gave the same answer within an error of $\pm 0.5\%$. This indicates that the eigenfrequency is correct since two independent analyses gave the same answer. This is the lateral oscillation of the plate with the shape as the static buckling load. This is a good basis for the length of a loading duration on the plate. Taking a range from 0.5 to 2 times the eigenfrequency for the loading duration gives the range where the plate has most dynamic effects. A longer duration can be considered a static loading, while a shorter duration can be considered an impulse load.

4.3.2 End displacement analysis

When considering the analyses of displacement of the plate end, a case was run on Abaqus, USFOS and the MATLAB-code and compared. The Abaqus and USFOS results were very similar. The only noticeable difference was that the higher order oscillation of the axial force load was somewhat higher in the USFOS result. This difference may be explained by that Abaqus may have some damping for very high frequencies when solving the differential equation. It should probably be added

some structural damping in the USFOS case, as that coincides more with reality, but the effect of this oscillation is very small, and do not affect the result much.

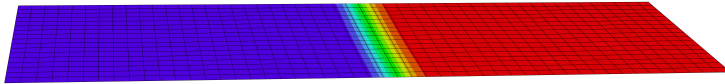


Figure 4.14: Stress propagation in a plate after $2.3 \cdot 10^{-4}$ seconds

The result from the MATLAB-code has noticeable differences from the result achieved by the FEA, although many of the characteristics, e.g., the time and magnitude of the maxima and minima are very similar. The most noticeable difference is the stress propagation effect. For the FEA results the loading start to increase after about $5 \cdot 10^{-4}$ seconds. This coincides almost perfectly with the time found in Equation (4.7). This effect is not taken into consideration at Ekstrom's formulas. The stress has to propagate back and forth through the plate before the stress starts to reach equilibrium after about $2.5 \cdot 10^{-3}$ seconds. Before that the increase, and decrease, of the stress happens in step-like intervals. Each step interval, after the first one, has a period at about $2t_{\text{plate end}} \approx 9.3 \cdot 10^{-4}$ seconds. This is the time for the stress to have propagated from the end of the plate, and back again. Figure 4.14 shows the stress after $2.3 \cdot 10^{-4}$ seconds in one of the analyses. The stress has propagated about half the plate length.

Ekstrom's formula does also not take into account the axial vibration of the plate, as a result the curve is smooth compared to the FEA-curves. These axial vibrations do not affect the result noticeable. It can be seen in Figure 4.4, at the end of the plot a slight phase shift between Ekstrom's curve and the FEA-curves can be seen. This may have to do with the way the time integration is solved. An explicit solution without equilibrium iteration will accumulate the errors from the previous step. With decreasing time step the phase shift may be minimized, but since the phase error is about $1 \cdot 10^{-4}$ seconds at the most it can be neglected for this result. This may be important for longer analyses using the MATLAB code, and ways to improve the code should then be taken into consideration.

As seen in Figure 4.5 the axial force does not change much when choosing different imperfection shapes. The plate changes which shape it buckles with during the run of the analyses. That is why there is no clear imperfection shape that gives the lowest axial load. Figure 4.15 shows the plate shifting buckling shape. An

imperfection shape of 7 half-waves over the length was chosen for the rest of the analyses. It seemed like this buckling shape was the most stable for the majority of the velocities.

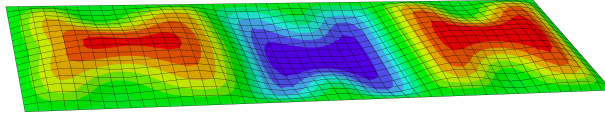


Figure 4.15: Plate shifts buckling shape from 3 to 9 half-waves over the length

The axial force for different velocities at $\Delta U = 1.36$ mm can be seen in Figure 4.6. Here does the effect of stress propagation dominate the result for Abaqus. At higher velocities than 3 m/s the stress does not reach the end of the plate before the plate is displaced the distance ΔU . Compared with the Ekstrom result the force starts about the same magnitude for velocity of 0.1 m/s in both cases, but becomes much larger in the Abaqus analysis for velocities above 1 m/s. The reaction force reaches almost twice the force in than in the Ekstrom result right before the axial force goes to zero. A proposed explanation for this difference in the FEA and analytical result is dynamic effects of stress propagation. As the Ekstrom result always assumes stress in the plate has come to equilibrium, this is not the case when Abaqus calculates the stress. The highest loads in the plate are when the first wave of stress propagation is at the plate end. The value of the axial load for Abaqus plate does vary for each velocity. This indicates that the stress at the end is also varying, probably because of the stress wave going back and forth in the plate. The value of the stress at the different velocities will therefore be dependent on where the stress wave is at the time of extraction before the plate reaches stress equilibrium.

It can also be noted that there is tension forces at the higher speeds, before the stress have propagated to the plate end. This is not a physical effect. The plate should be stress free before the stress wave propagates to the end. This has probably something to do with the way the stress in the elements are calculated in Abaqus, and should probably be regarded as a numerical error.

The axial force from the Ekstrom results are plotted alone in a graph in Figure 4.16. The figure shows that, for slow speeds, the plate is more relaxed for the given displacement than for a perfect plate. The axial force seems to converge towards about $9 \cdot 10^5$ N for very slow speeds. This is because the plates will also move in lateral direction when the load is applied, making the plate less stiff than the perfect plate. For high speeds, the lateral deflection starts becoming very small. This means that the axial stiffness contributes almost exclusively to the axial force. This means that the axial force converges to the static buckling load for a perfect

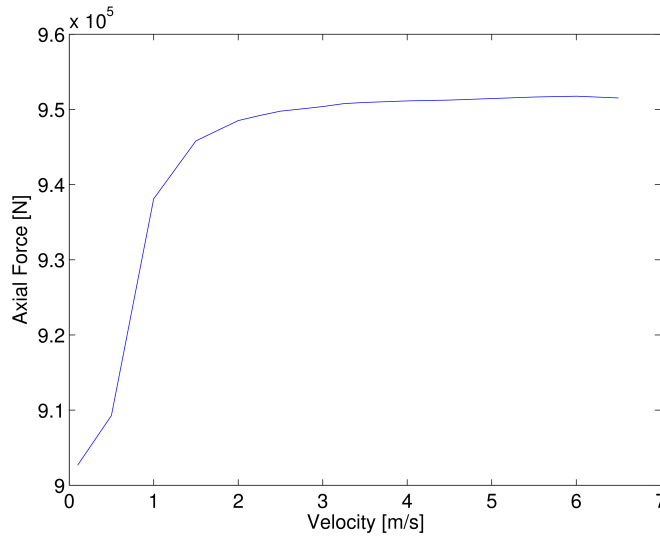


Figure 4.16: Axial force for MATLAB results $m = 7$ at $\Delta U = 1.36$ mm

plate.

Figure 4.7 shows the maximum lateral deflection of the plate at the axial displacement of $\Delta U = 1.36$ mm. At slow speeds the lateral deflection converges towards the static lateral deflection at that point. This value is about the same for both the FEA and the analytical solution. At higher speeds the lateral deflection goes towards zero. At this point the Ekstrom's solution decreases faster than the Abaqus result. In the MATLAB-code the amplitudes of the half-waves is assumed the same. This is not the case for the Abaqus result. The deflection plotted in Figure 4.7 is the largest lateral deformation in the model. Since the half-waves close to the displaced end is deflected more than the ones close to the other end, the energy needed to get the max lateral deflection is smaller in the Abaqus analysis than in the Ekstrom analysis.

Even though the plate showed signs of buckling, the capacity of the plate was not lost. As Figure 4.17 shows the slope of the axial load decreases after about 0.01 seconds for a displacement velocity of 0.5 m/s and an imperfection shape of 7 half-waves. This is where the buckling of the plate happens. The plate does, however, keep increasing the axial load after this point. This indicates that elastic dynamic buckling of a plate is not critical for the capacity of the plate. This means that other effects, like yielding, needs to be considered if a design strength formulation is going to be defined.

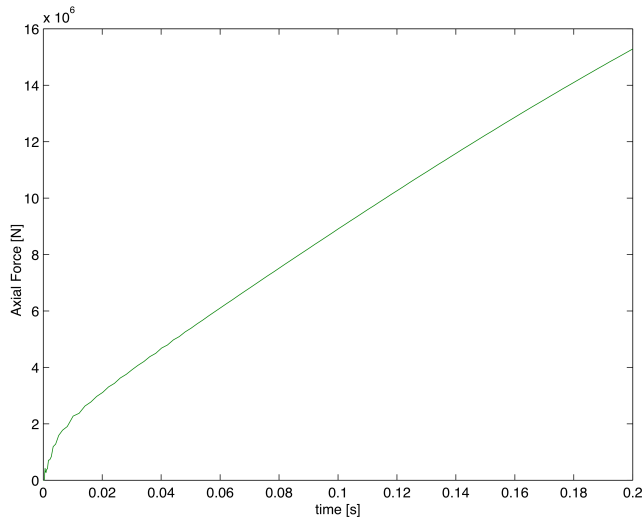


Figure 4.17: Axial force history for $v = 0.5$ m/s and $m = 7$

4.3.3 Axial load analysis

As it can be seen in Figure 4.9 that the maximum deflection of the plate during a sinusoidal load history is dependent on both axial force and duration. As with the end displacement analysis the plate shifts buckling shape for high load amplitudes. The relationship between deflection, force amplitude and loading duration breaks down when the plate starts to shift buckling mode. Since these amplitudes are very high and be in the plastic range for forces above $2 \cdot 10^6$ N, these result are not that relevant. A cropped version of Figure 4.9 can be seen in Figure 4.18. This is probably the relevant section of the results.

In Figure 4.18 it can be seen that there is not much difference between the different loading durations with small loading amplitude. This is very clear in Figure 4.11. For loading amplitudes lower than $P_0 = 0.5 \cdot 10^6$ N, the lateral deflection is almost identical. For larger amplitudes the effect of loading duration becomes important. The fast-applied loading has a much smaller lateral deflection than the slowly applied ones. For loading amplitudes over the static buckling load there is a relative big difference in the lateral deflection. For the slowest applied loads, the deflection does not change much, indicating that this deflection is the static deflection. As the loading duration decreases the lateral deflection becomes much smaller, indicating that buckling has not yet taken place. Below the static buckling load, the change in lateral deflection is almost independent of loading duration. This shows that the plate does not buckle with these loading amplitudes.

This effect can also be seen in Figure 4.10. When the plate has its maximal de-

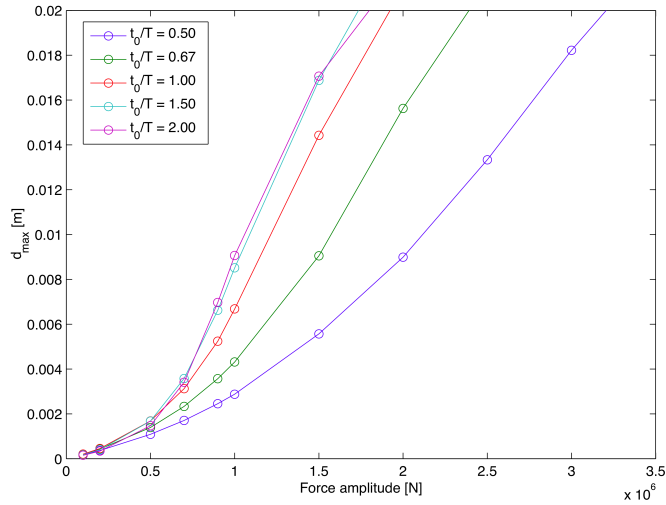


Figure 4.18: Maximum deflection of plate at different force amplitudes, d_{max} from 0 m to 0.02 m

flection below 0.005 m, the force amplitude is pretty constant for different loading durations. After $d_{max} = 0.010$ m the force amplitude that produce the given deflection is dependent on the loading duration, making the force amplitude large for small loading duration. This can be used to say that buckling for this particular plate happens after the plate deflects laterally more than between 0.005 m to 0.010 m. This may be because of the non-linear part of the strain in the plate, seen in Equation (2.1). When this becomes large enough, it becomes a noticeable part of stress in the plate, and the plate buckles.

The same effect that was shown for the end displacement analysis is also the case for the axial load analysis. The plate does not lose notable amount of capacity in the elastic analyses when it buckles.

4.3.4 Elastic-plastic analysis

As seen in the results, the Abaqus axial load analysis was done with a yield load specified for the material. The analyses had a maximum axial amplitude of $2 \cdot 10^6$ N, which is right below the yield load for pure axial force. A load amplitude above this level would not give any interesting result since the plate would have failed without any buckling.

For the shortest durations the plate does not collapse. The lateral displacements are essentially the same as for the elastic analyses. This is probably because the lateral displacement is so small. The plate gets bending stress from the arm created

from the lateral distance from the applied load. It is this bending stress that can grow so large that the total stress in the plate goes above yield. For the shortest duration, the inertia is so large that the lateral deformation becomes too small to give stress equal to the yield stress.

For the longer durations the dynamic effects smaller, so the plate have larger lateral deformations. This gives large enough bending stress in the plate, so it collapses plastically. For the plastic analyses it is much easier to find the capacity of the plate, as the collapse of the plate is shown clearly for the maximum deflection.

The capacity of the longest loading duration is probably close to the static capacity. This is probably close to $1.3 \cdot 10^6$ N. For the $\frac{t_0}{T} = 1.50$ it looks like it has the same capacity, but the increase in lateral deflection is not as sudden as the longest duration. This indicates that the capacity is a little larger. To confirm this, more amplitudes around this magnitude has to be run.

The collapse shape seen in Figure 4.13 was typical for all the analyses were the plate yielded. The first half-waves did have the largest amplitude when the plate was in the elastic area. This meant that the bending stress reached yield at this place first. This gave large deformations close to the applied load, while the half-waves at the other end had a smaller amplitude than for the elastic analysis.

If a simplified design oriented strength formulation is to be found, the yield stress has to be accounted for. A plate will not lose its capacity when only looking at the elastic dynamic buckling. There was not enough time to find a formulation in this work, however, the results can be used as basis for further work.

4.4 Conclusion

From the analyses run for dynamic buckling of an unstiffened plate, an effect stands out. For both load and displacement control, the inertia in the system gave a smaller lateral deflection. As the inertia forces became larger, the lateral deflection became smaller.

The plate did not lose much of its capacity when it buckled. The stiffness of the overall plate did become a little lower, but the plate did not lose as much capacity as a beam tends to do. This means that for most dynamic cases the yield stress will be the dominating factor.

Looking at the results from the elastic-plastic analysis, the plate yielded before the load that represented pure axial yield. This was because the imperfections of the plate introduces bending stress, and with enough lateral deformation the total stress could reach yield.

A formulation connecting the axial load capacity with a design criteria where both buckling effect and yield are accounted for, are something to do in later analyses.

Chapter 5

Analysis of tension leg in SWAY concept

As described in Chapter 3, dynamic effects increases the buckling capacity of a beam substantially. This means that in many dynamic cases the yield stress will be the dominating factor for the beam capacity. An exception is a very slender beam where the buckling capacity is much lower than the yield strength. Although these kinds of beams do not typically carry compressive loads, it can be situations were this is the case. The tension leg in the SWAY concept is such beam. The dynamic buckling of the tension leg was investigated in Straume [2013], but focused on the amplitude of the initial imperfection.

The SWAY concept is an offshore wind turbine. The wind turbine consists of a floating spar buoy with a tension leg mooring it to the seabed. It is the tension leg that is the relevant part. In extreme weather conditions the heave motions of the spar could be so large that the tension leg starts taking compressive forces. Since the tension leg is so slender, the beam could buckle almost at once the leg starts taking compressive forces. In this situation this could be a good thing. Since the tension leg has no function taking compressive forces, it is only important that the leg can still hold against tensile forces after the large heave motion. If the leg buckles early the leg may stay in the elastic area, and the leg will have full capacity after it has buckled. If the dynamic effects increase, the buckling capacity enough the leg may start to yield. This means that the leg will have reduced capacity in tension, and may fail as a result of the compression force.

Another effect to consider is a so-called "whipping" effect in the tension leg as it straightens. This effect may give substantial tension forces. This alone or combined with yielding during the compression of the leg, may cause failure.

A model of the SWAY concept has been made earlier for different analyses in USFOS. This model is adapted with correct material and dimension of the tension

leg. USFOS will then be used to do dynamic analyses for buckling of the tension leg. A case where the tension leg comes in compression will be done. The duration and force for the compression load will be varied, and compared. An eigenvalue analysis will be done for the buckling modes of the tension leg. This will determine if any of the periods for the motions are in the proximity of an eigenperiod. A static buckling analysis will also be done to compare the dynamic effects.

5.1 Setup of the analysis

The model-file of the SWAY wind turbine was already created, and was used as the basis for the analyses. The added mass for the tension leg was assumed from Morrison's theory for a cylinder. With this premise, the drag and added mass coefficients for the tension leg was set as $C_m = 2.0$ and $C_d = 0.7$ respectively. These are values typically used for a smooth infinite cylinder. In reality this will not be the case. Things like marine growth will change the coefficients, but as an initial analysis the assumption is close enough.

The structural damping model used in the analysis was chosen to be Rayleigh damping, (see Section 2.3.3). The damping ratio was set to 0.02 at 0.2 Hz and 2.0 Hz. Structural damping forces are not very large, but may be important for very high and low frequency structural and spurious numerical vibrations. The hydrodynamic damping, i.e., drag, is accounted for with the drag coefficient.

Buoyancy and gravity was applied. It was assumed that the tension leg did not contribute to the buoyancy of the spar. Mass of the structure was set from the model-file. The wind turbines was not modeled, but accounted for as a nodal mass at the top. The tension leg was subdivided into several elements to get the mass distributed correctly over the length, and to reproduce buckling of higher modes.

The mass and buoyancy was applied gradually to the model until equilibrium was reached. The ratio between the two was held constant, and the loading was applied statically before the dynamic analyses was run, so did not contribute to any dynamic movements of the structure.

The tension leg was assumed to have an imperfection as one-half sine wave. This shape was considered as a likely and conservative imperfection shape. The shape may be a result from effects such as current loads acting on the tension leg. Another likely shape is one-quarter sine wave. This shape gives very low buckling loads and will be non-conservative in this case.

A suitable motion for the displacement of the spar was a whole sine period phase shifted and displaced downwards, as illustrated in Figure 5.1 and described in Equation (5.1).

$$u_{end}(t) = \frac{A}{2} \left[1 + \sin \left(\frac{2\pi}{T}t - \frac{\pi}{2} \right) \right] \quad (5.1)$$

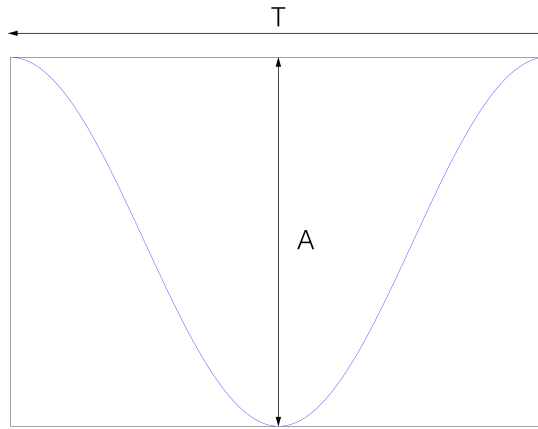


Figure 5.1: Improved displacement history as one sinusoidal period

This motion will give zero displacement and velocity at the start of the analysis. This will make the displacement much smoother, and spurious vibrations will be minimal.

A stiff spring was added between the end of the tension leg and the seabed. The spring was more than $1 \cdot 10^6$ times stiffer than the axial stiffness of the leg, and the displacement would be negligible for the results. The axial force of the tension leg was found by taking the displacement of the spring end and multiplying with the spring stiffness.

Table 5.1: Properties of the SWAY tension leg

Properties of the tension leg	
Young's Modulus	211 GPa
Yield stress	255 Mpa
Density	7850 kg/m ³
Length	100.0 m
Outer diameter	900.0 mm
Thickness	67.5 mm

The model can be seen in Figure 5.2. The tension leg is 100 meters long, and has the properties in Table 5.1. The end of the tension leg was fixed against translation on the seabed. The end could, however, rotate freely in x- and y-direction. No torsional rotation was allowed at the end. The topside was connected to the spar,

but it could rotate as the bottom end. The analysis was done with both elastic and plastic behavior of the material. Control parameters for the different analyses were found in the USFOS User's Manual [2012].

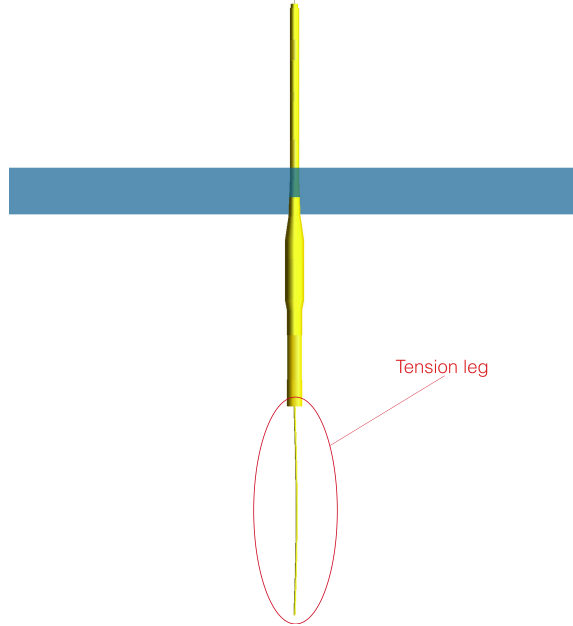


Figure 5.2: SWAY wind turbine model in USFOS

5.1.1 Implementation of initial imperfection

After the first analyses were run, it was apparent that something did not add up. The results are discussed in Section 5.3.1.

An approximate connection between the pre-initial displacement and the initial displacement can be found by idealizing the half-sine wave to an isosceles triangle. These describe the imperfection before and after the buoyancy and gravity was applied. The connection between the lateral displacement and the length of the tension leg are shown in Equation (5.2) and Equation (5.3).

$$\left(\frac{S}{2}\right)^2 = \left(\frac{L}{2}\right)^2 + w_{0,i}^2 \quad (5.2)$$

$$\left(\frac{S}{2}\right)^2 = \left(\frac{L + \Delta L}{2}\right)^2 + w_0^2 \quad (5.3)$$

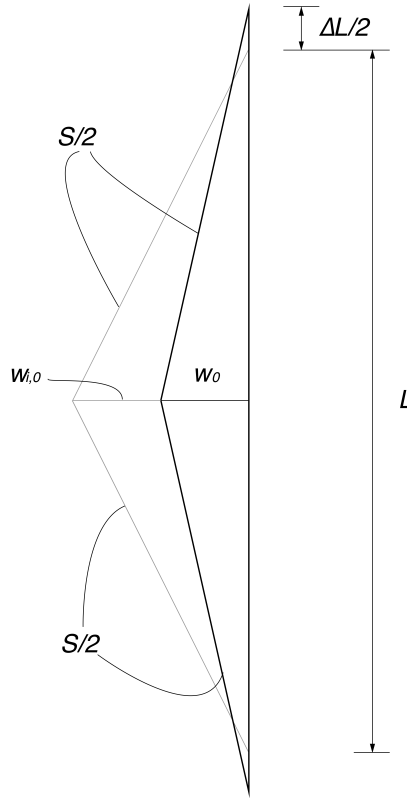


Figure 5.3: Initial imperfection of SWAY tension leg

Combining the above equations the pre-initial imperfection can be expressed by the initial imperfection, as shown in Equation (5.4)

$$w_{0,i} = \sqrt{w_0^2 + \frac{L\Delta L}{2} + \left(\frac{\Delta L}{2}\right)^2} \quad (5.4)$$

L may be found from the length of the leg, S .

Using Equation (5.4) a pre-initial imperfection of 1.8 m will give an imperfection of 0.5 m, or $0.005L$, when the analysis starts. This calculation takes the vertical displacement, ΔL , from the equilibrium state after buoyancy and gravity has been fully applied. It is also assumed that the length of the tension leg is constant. This combined with the assumption of a triangular shape of the imperfection will make the imperfection not exactly 0.5 m, but it is assumed that it is a good enough approximation. The amplitude of the initial imperfection and how this

affects dynamic buckling is discussed in Straume [2013], were different imperfection amplitudes on the SWAY tension leg are investigated.

5.1.2 Eigenfrequency analysis

First the eigenvalue analysis was set up. The control parameter EIGENVAL was used in the USFOS control-file. The top of the tension leg was fixed against translations in x- and y-directions. This was done to help against singularity in the eigenvalue matrix. This would not affect the values of the eigenfrequencies to the tension leg. The eigenvalue function was calculated after the mass and buoyancy was fully applied. The imperfection was as given in so that it matched the rest of the analyses.

5.1.3 Static analysis

As an introductory analysis, hand calculations of the Euler buckling load was found. Since the tension leg could be assumed simply supported in both ends the Euler buckling load could be found from Equation (5.5).

$$P_E = \frac{\pi^2 EI}{L^2} \quad (5.5)$$

The static buckling load was also found in USFOS for comparison. Here the analysis was done with an imperfect tension leg. The same imperfections that were used in the dynamic analyses were done. The parameter GELIMP was used to introduce the imperfections. These results were compared with the Euler buckling load, and the dynamic analyses.

The displacement amplitudes that were used in the dynamic analyses were also run as a static analyses. Now the dynamic effects can be compared with the static ones even though the axial load is smaller than the buckling load.

Last, a static analysis without any loading was done. From this analysis the tension in the leg was found, and the elongation. These results were used in the dynamic analysis.

5.1.4 Dynamic analysis

When the dynamic analyses were done a nodal displacement was used to simulate a buckling condition of the tension leg. It was assumed that the mass of the spar was so large that the compression force in the tension leg did not affect its motion in heave. The node at the top of the tension leg was displaced. The control parameter NODEDISP combined with TIMEHIST was used to displace the top in the desired motion. The NODEDISP parameter overrides all preset boundary conditions, the

gravity and buoyancy force did not contribute to any force in the tension leg. To remedy this effect, the node was displaced manually to the equilibrium found in the static buckling analysis.

The amplitude of the displacement, as well as the period of the sine function, was varied. The analysis was run for the whole displacement history and some time after the displacement was ended to be sure the maximum loading in both tension and compression had happened. The dynamic analysis was run for a total of $1.2 \times t_0$.

Table 5.2: Shows the different displacement amplitudes

Displacement amplitudes							
0.010 m	0.015 m	0.020	0.050 m	0.100 m	0.200 m	0.500 m	1.000 m

The amplitudes and periods used in the analyses are found in Table 5.2 and Table 5.3. The first buckling displacement equals the pure axial shortening when the Euler buckling load is applied. This displacement is from the position without any tension forces in the leg. A total of 8 amplitudes and 13 periods were run, making the total analyses equal to 104.

Table 5.3: Shows the different displacement duration periods

Displacement duration periods								
0.25 s	1.00 s	2.00 s	3.00 s	4.00 s	5.00 s m	10.0 s	20.0 s	30.0 s
40.0 s	50.0 s	60.0 s	100 s					

The results from the analyses were taken as the maximum compressive and tension loads during the time history. The process of setting up, running and extracting the result from the analysis were done using BASH-scripting. This made the process automatic and the large number of analyses could be done without any much work. The script used to control USFOS is attached in Appendix B.1.

The same analyses were also run with a yield strength defined for the material. This value is found in Table 5.1.

5.2 Result of the analysis

The following results were obtained by the analyses.

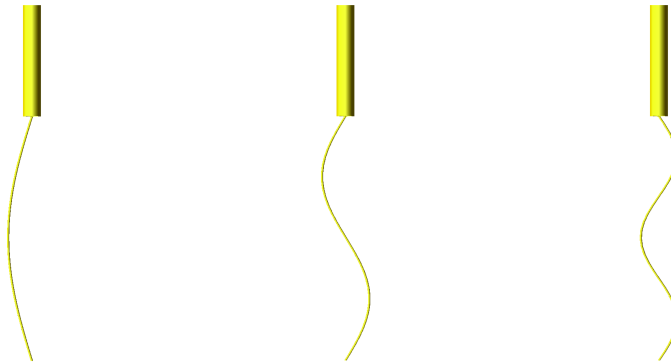
5.2.1 Eigenfrequency analysis

The eigenfrequency analysis gave the eigenperiods and eigenmode shapes for the first three eigenmodes as seen in Table 5.4. The deflection angle is relative to the direction of the imperfection shape.

Table 5.4: Eigenperiod and eigenmode shapes for the tension leg

Deflection angle	Eigenperiod [s]	Eigenmode shapes
0°	1.79	1 st
	1.15	2 nd
	0.54	3 rd
90°	3.80	1 st
	1.15	2 nd
	0.54	3 rd

Each eigenmode shape had two excitations 90 degrees relative to each other. The pairs had almost identical eigenperiods, except for the first eigenmode shape. The first three eigenmode shapes were identical to the first three buckling mode shapes. This could indicate that the tension leg would buckle in the one of the eigenmodes. If the loading period is similar to the eigenfrequency the eigenmode may be excited. Figure 5.4 shows the eigenmode shapes referred to in Table 5.4.



(a) 1st eigenmode shape (b) 2nd eigenmode shape (c) 3rd eigenmode shape

Figure 5.4: The first three eigenmode shapes shown in USFOS

The largest eigenmode of the tension leg had a period of 3.80 seconds. This was induced 90 degrees from the assumed initial imperfection. The period for the eigenmode that moves in the same direction as the initial imperfection is less than

half this period. This shows that the assumed initial imperfection has a big impact on the eigenperiod.

The eigenperiods with the eigenmode equal to the buckling mode are important to note when looking at loads from waves. A large wave, that could induce large motions on the structure, would probably not have periods that are as short as these. The assumed loading periods in the analyses, however, have a period that is in the same magnitude as the eigenperiods. This means that the buckling mode could buckle in one of the eigenmodes, and may have less capacity around the eigenfrequency.

From Straume [2013] it was found that beams tend to buckle at higher modes with a fast-applied load. The eigenmode corresponding to the shortest duration of loading was therefore found. The shortest loading period was 0.25 seconds, and the eigenperiod that were the closest to this value was 0.20 seconds. The eigenmode can be seen in Figure 5.5.



Figure 5.5: Eigenmode with a period of 0.20 seconds

5.2.2 Static analysis

The static buckling load was calculated using Equation (5.5). A static analysis of the SWAY model was run in USFOS to confirm the static buckling load. The result is shown in Table 5.5.

A load-displacement history from the USFOS analysis is shown in Figure 5.6 with a linearly increasing load applied to the tension leg. Since the USFOS analysis has

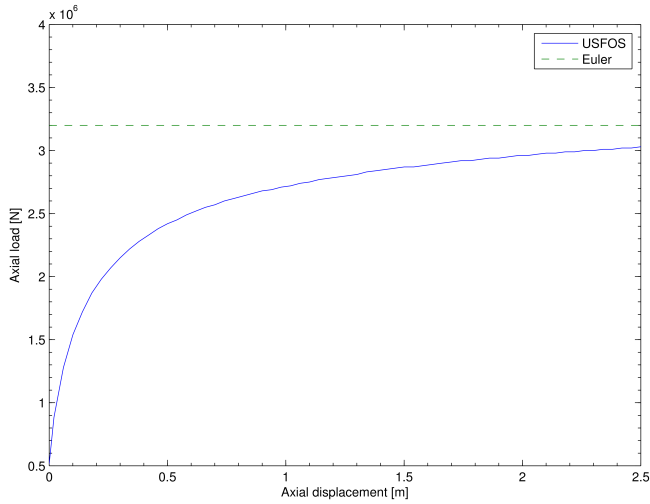


Figure 5.6: Static buckling analysis in USFOS

Table 5.5: Result of the static analysis

Calculation method	Buckling load
Euler buckling load	$3.2 \cdot 10^6 N$
USFOS	$\sim 2.7 \cdot 10^6 N$

imperfections the tension leg starts to lose the capacity for axial load earlier than the Euler buckling load. The axial load converges towards the Euler buckling load.

The Euler buckling formula only accounts linear effects of buckling. If the deflection becomes big enough in USFOS, the load starts to increase above the Euler buckling load. This is a membrane effect that starts to dominate in the USFOS analysis, although this axial displacements are much larger than what is relevant for this case.

Later, when the static capacity is compared with the dynamic analyses, the Euler buckling load is used for simplicity.

The dynamic analyses were compared to the static ones. The only difference between the analyses, was that the dynamic effects. This means that a dynamic load factor, DLF, can be found for the different analyses. Some of the DLFs are found in Figure 5.7. The long loading durations, as $T = 100$ s, gives no noticeable amplification between the dynamic and static analysis, while the short durations give an amplification that is more than 100 times larger. There is also a minimum for

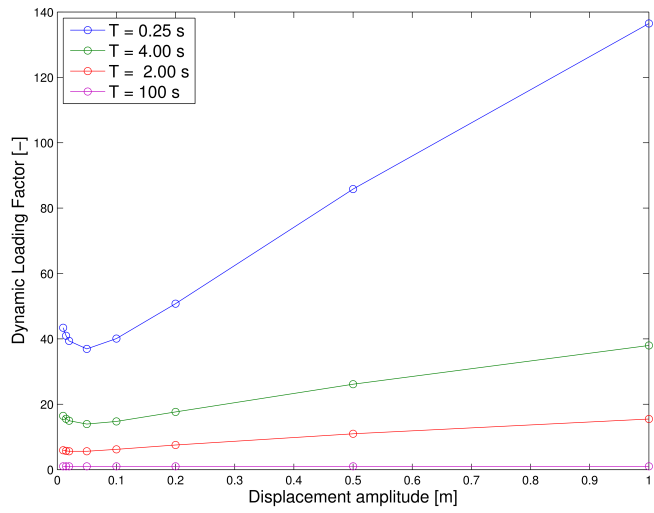


Figure 5.7: Dynamic loading factor for the dynamic analyses

all the periods for a displacement amplitude of 0.05 meters.

5.2.3 Dynamic analysis

Excerpts from the results are given in Table 5.6 and Table 5.7. In Table 5.6 the period is held constant, while a range of displacement amplitudes is shown for that period. The maximum axial loading is shown, as well as a comparison of this loading and the Euler buckling load. In Table 5.7 the maximum load is shown for a constant displacement amplitude with different loading durations. Comparison with the Euler buckling load is also shown here.

Table 5.6: Dynamic analysis with a loading period $T = 5$ s

Displacement amplitude	Maximum axial load	P/P_E
0.010 m	$2.2 \cdot 10^6$ N	0.68
0.015 m	$2.4 \cdot 10^6$ N	0.76
0.020 m	$2.7 \cdot 10^6$ N	0.84
0.050 m	$4.1 \cdot 10^6$ N	1.28
0.100 m	$6.3 \cdot 10^6$ N	1.96
0.200 m	$1.0 \cdot 10^7$ N	3.17
0.500 m	$2.0 \cdot 10^7$ N	6.12
1.000 m	$3.2 \cdot 10^7$ N	9.89

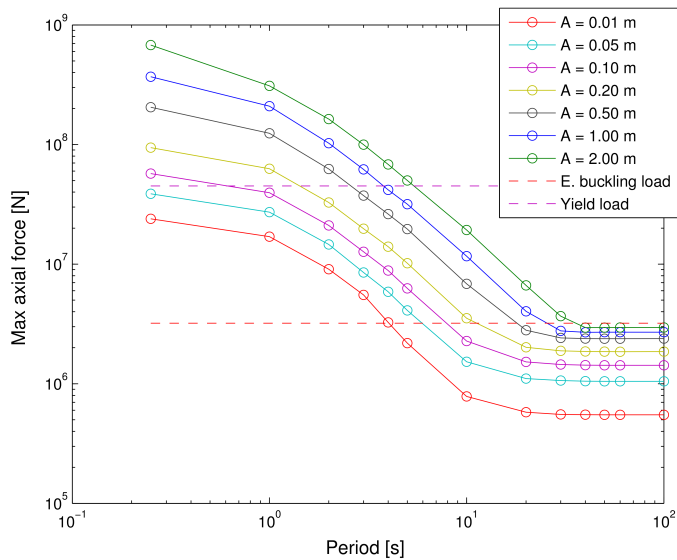


Figure 5.8: Maximum axial compression load of tension leg

Table 5.7: Dynamic analysis with a displacement amplitude $A = 0.5\text{m}$

Loading period	Maximum axial load	P/P_E
0.25 s	$2.0 \cdot 10^8 \text{ N}$	63.9
1.00 s	$1.2 \cdot 10^8 \text{ N}$	38.8
2.00 s	$6.2 \cdot 10^7 \text{ N}$	19.5
3.00 s	$3.7 \cdot 10^7 \text{ N}$	11.7
4.00 s	$2.6 \cdot 10^7 \text{ N}$	8.18
5.00 s	$2.0 \cdot 10^7 \text{ N}$	6.12
10.0 s	$6.9 \cdot 10^6 \text{ N}$	2.14
100 s	$2.4 \cdot 10^6 \text{ N}$	0.74

In Figure 5.8 the maximum axial load in the analysis is plotted against the loading period for several of the displacement amplitudes. As the period decreases the maximum loading increases very exponentially. For readability the graph has been plotted in a logarithmic scale in both the x- and y-axis. The load that gives axial yielding and the Euler buckling load marked on the graph.

The analyses with the longest loading durations have all maximum loads that are almost equal or smaller than the Euler buckling load. This may indicate that the tension leg buckles statically or does not buckle at all. As the loading duration decreases, dynamic effects starts to dominate and the maximum axial load increases very rapidly. This happens after the loading duration becomes smaller than 30 seconds. Every loading amplitude increases at an exponential rate, which becomes linear in the figure, before the rate decreases at the end. Most of the analyses have maximum axial loads above the yielding load at the shortest durations.

Figure 5.9 shows the axial load history for the tension leg with a loading duration of 0.25 seconds and a displacement amplitude of 1 meter. In this figure the positive values are compression loads. The maximum loading is clearly shown in the figure. The maximum loading takes place just before the maximum displacement at 0.125 seconds. This means that the leg buckles and is taken as the buckling load for this analysis. It can also be seen that the tension leg starts taking tension forces after the buckling has happened. This could indicate that tension forces may be relevant post buckling of the tension leg.

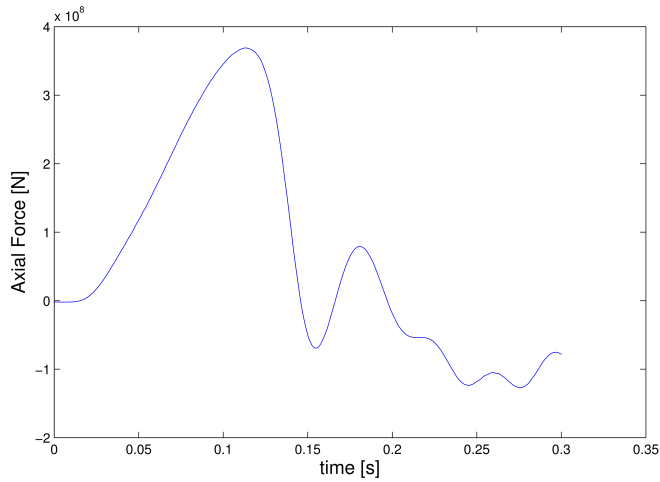


Figure 5.9: Load history of tension leg for $A = 1.00$ m and $T = 0.25$ s

5.2.4 Elastic-plastic analysis

The tension leg was run with a defined yield stress. The maximal axial load of the leg are shown plotted in Figure 5.10.

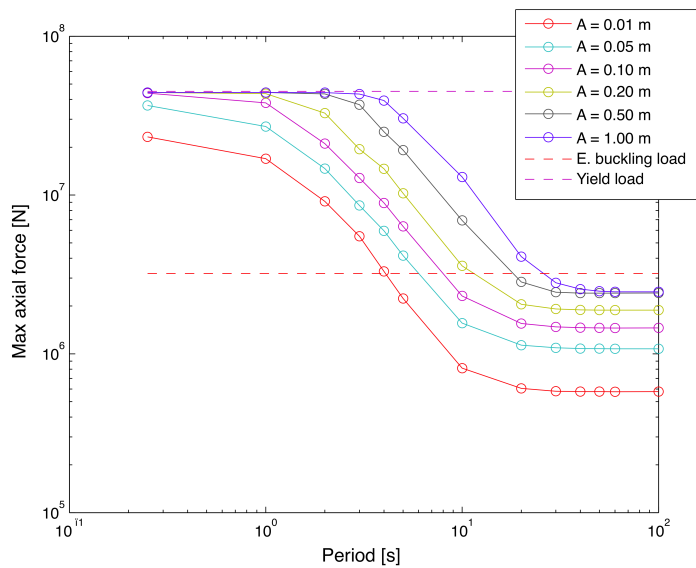


Figure 5.10: Maximum axial compression load of tension leg

The figure is very similar to the elastic analysis before the pure axial yield load. As the load approaches the yield load the load bends of, and converges to the yield load. There is no noticeable difference between the elastic-plastic analysis and the elastic analysis before the axial load is very close to the pure axial yield load.

5.2.5 Post buckling behavior

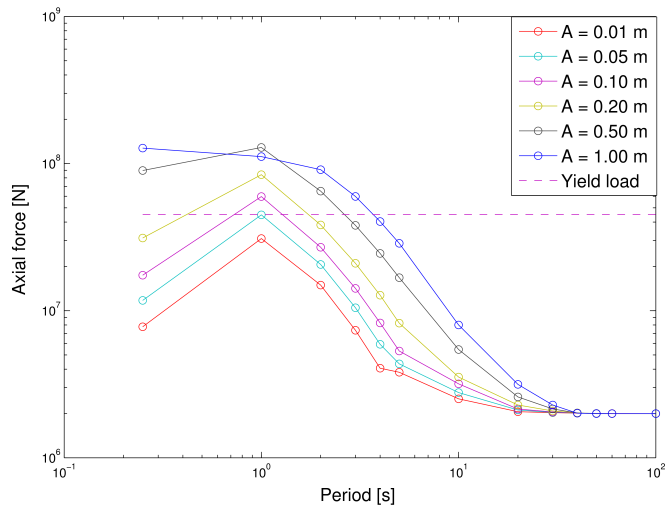


Figure 5.11: maximum axial tension load of tension leg

Figure 5.11 shows the maximum tension for the analyses. In the static area of the graph, i.e., periods above 30 seconds, the maximum tension of the tension leg is constant. This value is equal to the tension at equilibrium, before the displacement starts. The maximum tension increases also exponentially as the dynamic effects increases. A thing to note in the figure is that it seems that the maximum tension has a top at a loading period of 1 second for almost all displacement amplitudes.

When Figure 5.11 is compared with Figure 5.8, the maximum tension load is actually larger than the compression loads for many of the analyses. This means that the axial tension force is larger than the yield load for the shortest loading periods. The maximum tension load actually decreases for most of the analyses for the shortest period of 0.25 seconds.

The loading history for the analysis with displacement amplitude equal to 1.00 meters and loading period equal to 1.00 seconds are shown in Figure 5.12. Here the axial loading goes directly from the maximum compression load, when the leg buckles, to the maximum tension load after. The maximum tension load happens at around 0.55 seconds after the displacement has begun. This means that the

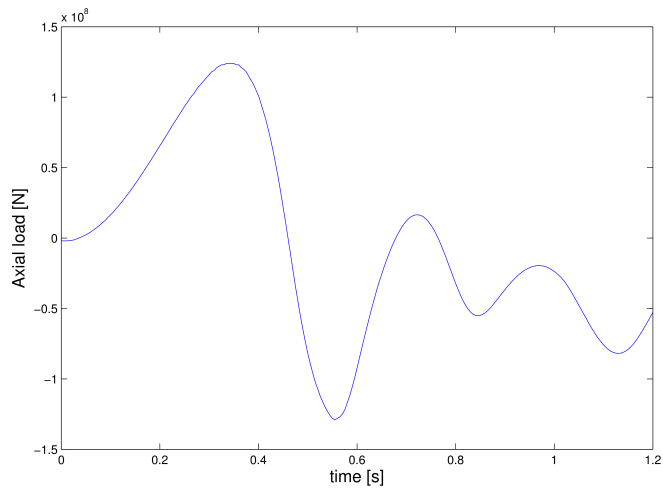


Figure 5.12: Load history of tension leg for $A = 1.00$ m and $T = 1.00$ s

maximum tension load happens while the top of the tension leg is almost at the lowest point, and on its way back to the equilibrium.

5.3 Discussion of the result

5.3.1 Analyses with spurious vibrations

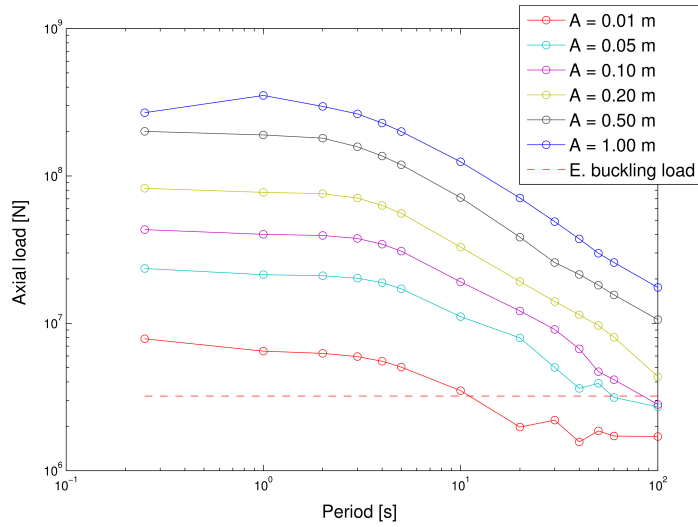


Figure 5.13: First maximum axial compression load of tension leg

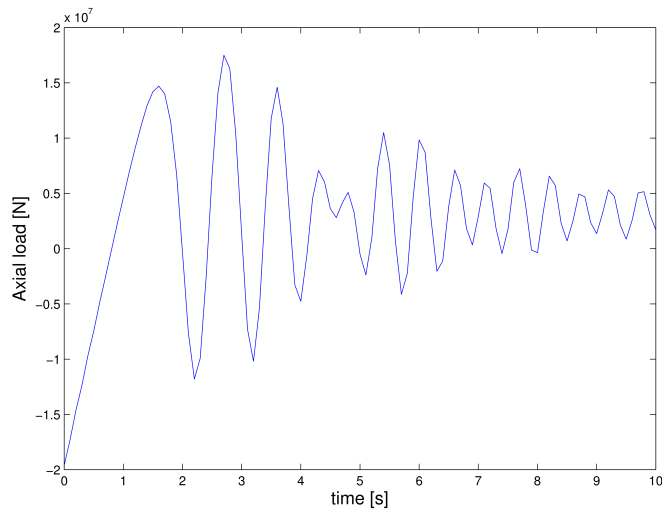


Figure 5.14: Time history for axial load for $A=1.00$ m and $T=100$ s with vibrations
 After the first run of analyses was done, it was apparent that something did not

add up. The maximum axial loads had, for many of the analyses, a much higher load than the Euler buckling load at near static analyses. As seen in Figure 5.13, the axial loads at a period of 100 seconds are very high even though the dynamic effect should be negligible at this loading rate.

Looking at the time history of the loading the reason for the high axial load becomes apparent. As seen in Figure 5.14 the loading history has high vibrations even with slowly applied loading.

The major contribution to the false results in Figure 5.13 was found to be the way initial imperfections was applied. In USFOS the imperfection is first applied at the beginning of the analysis, then the model is set in equilibrium between gravitational forces and buoyancy forces. This means that the initial imperfection, when starting the dynamic analysis, is smaller than the one specified in USFOS input-file. This effect is illustrated in Figure 5.3 with simple trigonometric shapes. If the pre-initial imperfection, $w_{i,0}$, is small enough the tension leg will not have any initial imperfection when starting the dynamic analysis. This may introduce significant numerical errors in the result.

A pre-initial imperfection of 0.5 meters will give zero imperfections when the analysis starts. This was given in the first analyses, so the high axial loading could partly be explained by this effect. Actually an initial imperfection less than 1.7 meters will give zero imperfections according to Equation (5.4).

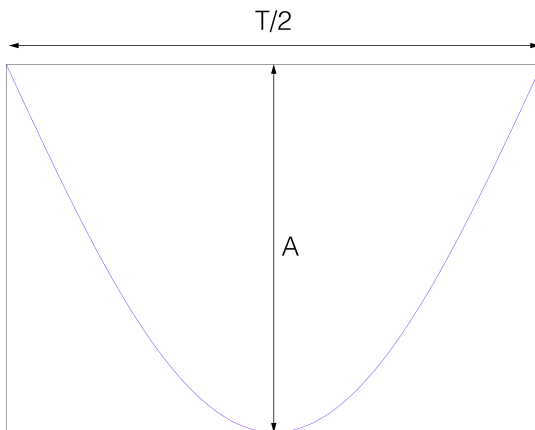


Figure 5.15: Original displacement history of SWAY spar as half-sine wave

The pre described motion set for the node was first assumed to be a half-sine wave, as seen in Figure 5.15. With this motion the velocity of the displacement was at its highest when the analysis started. This rapid change in velocity could also contribute to the vibrations seen in Figure 5.14.

5.3.2 Eigenvalue analysis

The results obtained from the eigenfrequency analysis show that the eigenmodes have periods in the same range as some of the loading periods in the dynamic analysis. However, this did not affect the result very much. The buckling mode was mainly the same as the imperfection even though it was in the resonance range of a higher eigenmode. A thing to note from the analysis was that the eigenperiods were dependent on the assumed imperfection shape and load in the tension leg.

For the first eigenmode, the eigenperiod in the same direction as the imperfection was much larger than normal to the imperfection. Since the leg is in tension, the explanation of this can be the importance of geometric stiffness. When a lateral deflection is introduced the tension leg is forced out in that shape. This will make it more reluctant to oscillate around this point, and the eigenperiod will decrease. In the other direction this will have minimum effect since the leg has no imperfections in that direction. As mentioned, the higher mode shapes are almost identical. This is because these eigenmode shapes do not have an assumed imperfection. A run without the initial imperfection showed that all the eigenmodes with equal shape had the same eigenperiod.



Figure 5.16: Buckling response for $A = 1.00$ m and $T = 0.25$ s

The only scenario that buckled in another buckling mode than the first was the scenario with a period of 0.25 seconds. Comparing Figure 5.5 with Figure 5.16, it can be seen that the wavelengths are in the same range. A more careful inspection of the wavelengths gave that the eigenmode had a wavelength of about 41 meters, giving 5 half-waves along the tension leg. The buckling mode had a wavelength

of about 35 meters. This would give a eigenmode with almost 6 half-waves along the tension leg if the wave amplitude had been constant over the length. The eigenmode that corresponded to this had an eigenperiod of 0.14 seconds. The buckling mode did not correspond directly to the eigenmode, but to a eigenmode with a smaller eigenperiod. The buckling mode does not have a constant amplitude across the whole leg, but decreasing further down the leg. This may indicate that the buckling mode cannot "feel" the whole leg when buckling. As a result, the corresponding eigenmode could be for a shorter beam. This could give a different buckling mode than the eigenmode.

Another effect could be the change in amplitude of the buckling mode. Since the amplitude decreases further away from the applied loads, less mass gets accelerated further away, than close to the applied loading. This may also give an effect on the length of the half-waves.

5.3.3 Higher buckling modes

The analyses with the highest velocities did chose another buckling shape than the imperfection shape. This can be seen in Figure 5.16. The leg buckles with most deflection at the top of the leg, the deflection becomes smaller longer down the riser. This is probably because when the spar moves as fast as in the illustrated analysis. It takes about 0.02 seconds for the stress to move 100 meters, i.e., from the top of the riser to the bottom. When the riser moves at its fastest, the leg becomes displaced by 0.25 meters before the stress has propagated to the bottom. If this increase in compression forces is above the buckling capacity of the top of the tension leg, the leg will buckle before the bottom part have reached the same stress. When looking at the analysis, the leg seems to begin to buckle at the top, when the velocity of the spar is at its peak. The length of the part that will start to buckle is hard to predict, since both stress propagation and inertia forces will contribute.

The buckling length for these higher modes will be much shorter than the whole leg. Looking at the case with $A = 1.0$ m and $T = 1.0$ s. The Euler buckling load for the buckling mode with a half-wave of 17.5 meters across the length will be

$$P_k = \frac{\pi^2 EI}{(L_k)^2} = 1.05 \cdot 10^8 \text{ N} \quad (5.6)$$

This is much more than the Euler buckling load calculated earlier, but it is still under the maximum compressive axial load that the analysis showed. In the analysis the leg withstood a compressive force of $3.69 \cdot 10^8$ N before it buckled. The difference between the dynamic result and the static result, with respect to the higher buckling mode, would mainly be the inertia and drag effect.

The maximum compressive load in the tension leg is much more sensitive to change in the loading duration than change in the loading amplitude. This is illustrated

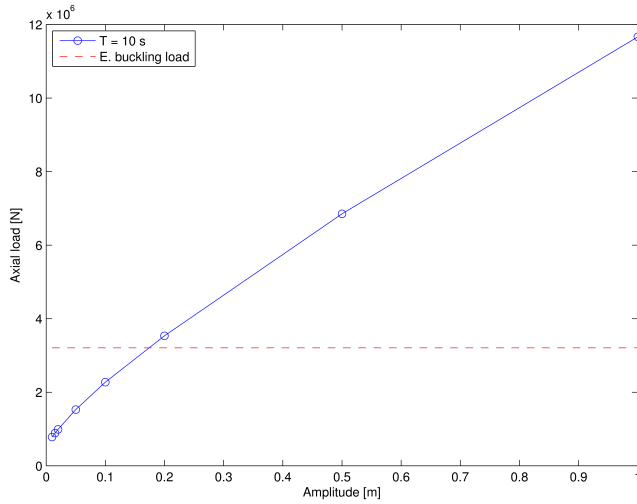


Figure 5.17: Change in maximum loading with varying amplitude and $T = 10$ s

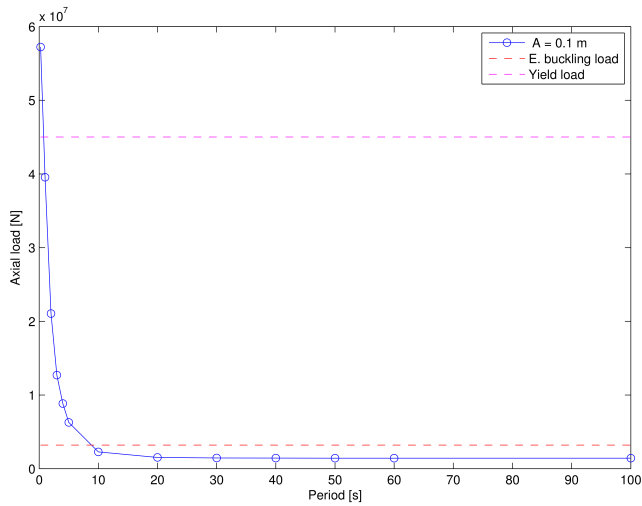


Figure 5.18: Change in maximum loading with varying period and $A = 0.1$ m

in Figure 5.17 and 5.18. The axial loads in Figure 5.17 are varying almost linearly with different amplitudes. In Figure 5.18 the loading is varying exponentially with different periods.

5.3.4 Comparison with static analysis

In the static analysis the buckling load was found from hand calculations and in USFOS. The imperfections had a great effect on the buckling load. This is because the initial imperfection is set on the basis of the tension leg in tension. Though, this does not have an effect on the static analyses. Here the imperfection that is important is when the leg starts to take compressive forces. In the static analyses the tension leg had an imperfection of $0.018L$ as the buckling load was calculated. The effect can be seen in Figure 5.6, where the tension leg starts to lose axial strength long before the Euler buckling load.

The static analyses of the different displacement amplitudes were done to determine the dynamic effects. The displacement amplitude of 1 meter was the only one that had sufficient loss in axial strength, and could be characterized as buckling. The other result had still axial strength when axial displacement was increased and the load was much lower than the Euler buckling load.

The dynamic analyses show that the tension leg is exposed to large axial forces when dynamic effects are considered. The loading was larger than the Euler buckling load for most of the results when dynamic effects become important. The loading even became larger than the axial yield load when the loading period became short enough. This shows that dynamic effects are very important when considering buckling effects. An example is a static analysis of a displacement amplitude of 0.2 meters will give axial loads lower than the buckling load. If the same analysis is done dynamically with a loading period of 1.0 second the axial load will be larger than the yield load both in compression and tension.

5.3.5 Elastic-plastic analysis

The effect of a yield capacity was different for the SWAY tension leg than for a unstiffened plate discussed in Section 4.2.5. For the tension leg case the leg did not reach yield stress in the cross section before the axial stress was almost at the yield load. This means that there is little bending stress in the cross section before the leg reaches its capacity.

This is because the leg loses its capacity as the leg moves out laterally. This means that the bending stress in the cross section does not become large before after the leg has buckled, and already lost its capacity. This means that the capacity of the leg will be the buckling capacity for loads that are under the yield load, and the yield capacity for loads that are above.

Figure 5.19a shows the deformation of the tension leg, with a displacement amplitude of 1.0 meter and a duration of 1.0 second. The leg forms a plastic hinge almost at the top of the leg. This means that the axial load in the leg cannot increase because of the displacement of the spar.

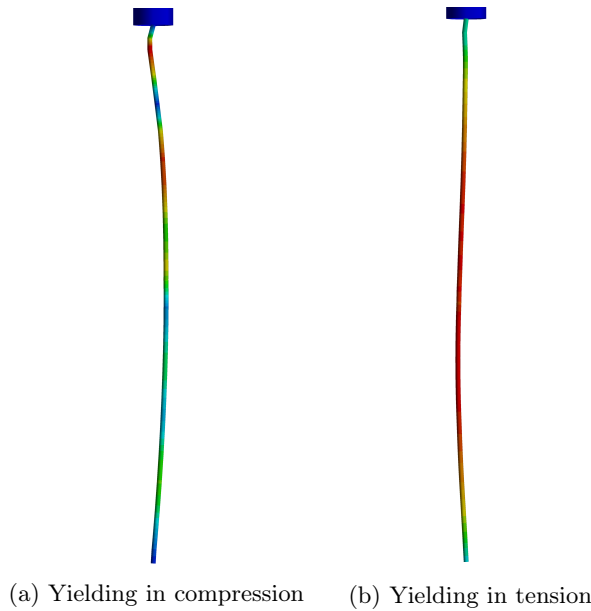


Figure 5.19: Plastic deformation of the tension leg with $A = 1.0$ m, $t_0 = 1.0$ s

Figure 5.19b is the same scenario after the compression is done. The plastic deformation can still be seen at the top of the leg. As the leg straightens, a large part of the leg is yielding in tension. This means that the leg does not have any extra capacity to hold against any increase of the load.

5.3.6 Post buckling behavior

An interesting effect of the dynamic buckling analysis was the axial loading that happened post buckling. The tension leg straightened after the buckling had happened, as the top of the tension leg was displaced back to the equilibrium position. This forced the lateral deflection back from the maximum deflection. When this straightening of the leg had a period that excited the lateral motion of the tension leg the leg experienced a "whipping" effect, giving large tension forces in the leg. This was especially true for the loading period of 1 second. Figure 5.20 shows the configuration of the tension leg when maximum tension load occurs. This is from the case shown in Figure 5.12.

The top of the tension leg is moving upwards while the lateral motion from the buckling is still moving outwards. This makes the leg take tension forces. The maximum happens when the lateral deflection turns and starts going back, so the acceleration is large. For most of the analyses, the tension load gets smaller for the shortest loading duration. This may be because the leg does not have time to react to the displacement. The lateral displacements are small because the leg



Figure 5.20: Configuration of tension leg with max tension force

does not have time to react to the displacement. When the leg straightens again, the leg does not have a large lateral velocity. This means that the force needed to straighten the leg is not that large.

5.3.7 Mass calculations

The assumption that the mass of the SWAY wind turbine was so large that the displacement would not affect the tension leg was checked. The mass of the SWAY wind turbine, including ballast, was $4.6 \cdot 10^6$ kg. Looking at a static case first, the Euler buckling load was given as the capacity of the tension leg. The assumption is that the force of the tension leg can be seen as a reduction of the gravitational acceleration, g . The acceleration can be seen as

$$a = g - \frac{P_E}{M} = 9.11 \text{ m/s}^2 \quad (5.7)$$

This is a reduction of 7 %, which can be accepted.

In the dynamic analyses, the force of the tension leg was much greater than the Euler buckling load. The reduction in gravitational acceleration could be larger, although, the dynamic amplification factor for the axial deformation would also be larger. The effect of the tension leg would probably be so large that it could not be neglected for the analyses with the shortest loading durations. This means that

the results from the fastest applied loads would overestimate the applied axial load. It would, however, be difficult to compare the results if the tension leg should be considered in the displacement of the spar buoy.

5.4 Conclusion

The results of the analyses show that the dynamic effects for the tension leg are very important. This means that the riser can yield for very small displacements in compression. For a static analysis of the same case would give no critical loads. The dynamic buckling load was also shown to be much larger than the static. It was seen that the buckling load became much greater than the yield load at several scenarios.

Eigenperiods had little effect when the initial imperfection was dominating. When the loads were applied fast enough, the leg started to buckle in other modes than the initial. When this happened, the effect of eigenperiods in the same magnitude as the loading durations became noticeable. Even though the buckling mode did not match exactly the closest eigenperiod, it was clear that the effects are correlated. The exact connection was hard to find.

Post-buckling the leg straightened. This gave substantial tension forces in the leg. The tension in the leg was especially large for periods of 1 second. This indicated that there was some kind of resonance at this period. For loadings with duration of 0.25 seconds the tension leg were smaller, meaning that the loading was applied so fast that the leg did not have time to react.

The plastic capacity of the tension leg was reached with enough dynamic effects. The leg was far below this load for the highest displacement amplitude for a static analysis, meaning that the leg would have full capacity in tension after the displacement. With the dynamic effects taken into account the buckling capacity would increase so that the yield stress was reached for many of the analyses. This would result in permanent damage of the tension leg.

These motions of the SWAY spar buoy is very fast for the most extreme cases, and would probably not happen in reality. To find out, and run analyses, on motions that the buoy that could be the case during extreme motions could be done at a later stage.

As further work the buckling analyses could be combined with other loads on the SWAY structure. If the imperfection of the tension leg had been induced by for example current and wind forces, a more realistic buckling capacity could be found. A more detailed analyses of the connection between buckling modes and eigenmodes could be done. Instead of a pure displacement control of the spar buoy, the force from the tension leg could be considered.

Chapter 6

Impact analysis of dropped riser

Reinertsen Oil and Gas has been looking at a scenario where a part of a steel production riser gets dropped from a platform. When the riser part reaches the bottom it will have gained a high velocity, and an impact could induce buckling of the riser. The riser could hit the wellheads, or other subsea equipment, beneath and cause damage. If the riser buckles the amount of energy of the impact could be smaller since the amount of kinetic energy of the riser that would be transferred to the impact would be less. If the dynamic effects make the buckling capacity large enough, the amount of energy in the impact could contribute to more damage of the wellheads.

If the impact force is large enough, the capacity of the riser may be limited to the yield strength of the material. The buckling capacity may be larger than static considerations, however, if the riser starts to yield, the capacity would not increase.

Different scenarios have been checked. Different riser lengths have been used. The risers were dropped with different angles from the platform, how this affected the impact response have been looked at. Since the properties of bottom structure, that the riser hits, are unknown for this analyses, different impact stiffness has been used.

6.1 Setup of the analysis

The material used for the production riser was given as 80 ksi grade steel. The relevant properties of this steel is specified in Table 6.1

The dropped production riser consisted of five main components. The main riser part was made up of sections called standard joints. The sections were about

Table 6.1: Material properties of 80 ksi grade steel

80 ksi grade steel	
Density	7850 kg/m ³
Young's Modulus	207 GPa
Poisson's ratio	0.3
Specified minimum yield stress	552 MPa
Ultimate tensile stress	650 MPa

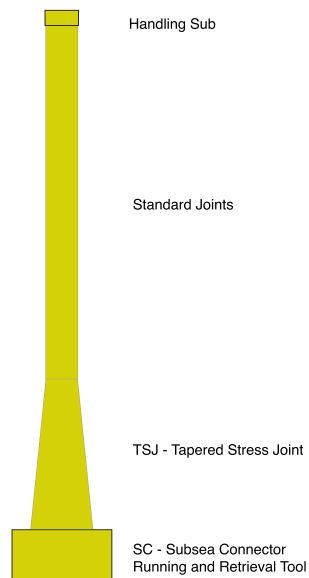


Figure 6.1: Sketch of the production riser

12 meters each. Different riser length was checked, meaning that the number of standard joints was varied. In addition there was a tapered stress joint connected to the subsea end of the main riser. This tapered joint was about 15 meters long with increasing outer diameter. At the end of the tapered joint was a thick flange. The tapered stress joint was connected to a subsea connector. This is used to connect the riser to the wellhead. Connected to the subsea connector was a "running and retrieval tool". At the very top of the standard joint was a small handling sub. A sketch of the production riser can be seen in Figure 6.1. Table 6.2 gives the mass and main dimensions of the components used in the analysis.

The short components of the riser were modeled as a nodal mass. This meant the

Table 6.2: Components of production riser

Component	Outer diameter	Thickness	Mass	Length
Handling Sub	305.6 mm	N/A	135 kg	1.215 m
Standard joint	279.5 mm	14.1 mm	1180 kg	12.20 m
TSJ	279 - 332 mm ^a	14.5 - 41.0 mm ^a	3300 kg	15.14 m
Subsea connector	1168 mm	N/A	5700 kg	1.425 m
R & R Tool	2546 mm	N/A	5000 kg	N/A

^a See Appendix C.1.1 for details

handling sub, the subsea connector and the "running and retrieval tool". This was because these would not buckle or be critical for the impact, so the only important effect was the mass. The mass was given to the top and bottom of the riser, according to where the components were placed.

The tapered stress joint had a constant internal diameter, while the thickness varied over the length. The joint had three different sections with linearly varying thicknesses. To represent this in USFOS the joint was modeled with beam elements of 0.5 meters in length. The thickness of the cross section was given as the average between the two ends of the beam. The length of the beam elements was given from another input file, discussed later. At the end of the tapered stress joint there was a flange. This was represented as a nodal mass in the analyses for reasons mentioned earlier.

Table 6.3: Drop scenarios for production riser

Riser length	Velocity at impact	Drop angle	Scenario
42 m	15.0 m/s	85°	PA85
		89°	PA89
128 m	17.0 m/s	85°	PC85
		89°	PC89
237 m	18.5 m/s	85°	PF85
		89°	PF89

Another simulation of the dropped production riser had been done. The riser had been dropped through the water with different lengths. The angle between the horizontal line and the riser had also been varied when dropped. From these analyses the speed of the riser when the bottom was hit was given. The configuration of the riser was also found, i.e., the coordinates of the nodes of the riser. These results were taken as input for the dynamic buckling analysis. The riser configuration his-

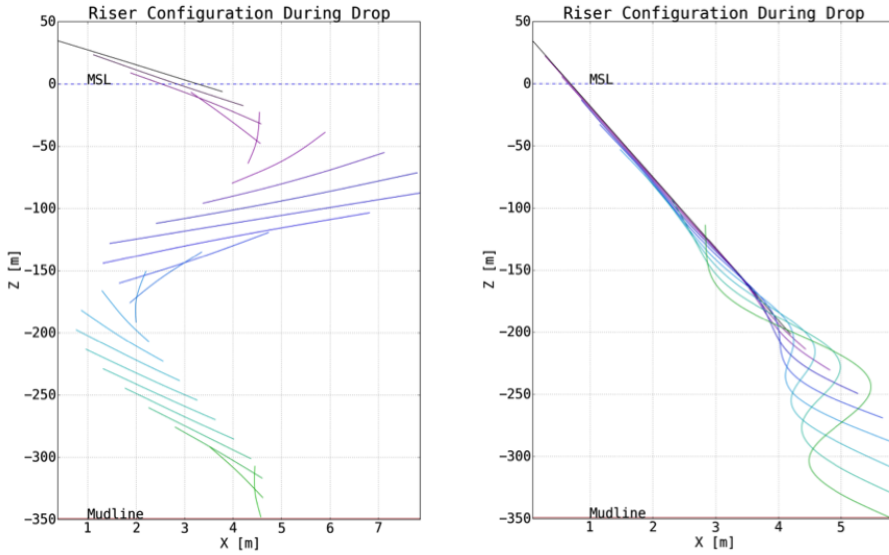
(a) PA-riser with drop angle of 85° (b) PF-riser with drop angle of 89°

Figure 6.2: Drop of production riser with different length and drop angle

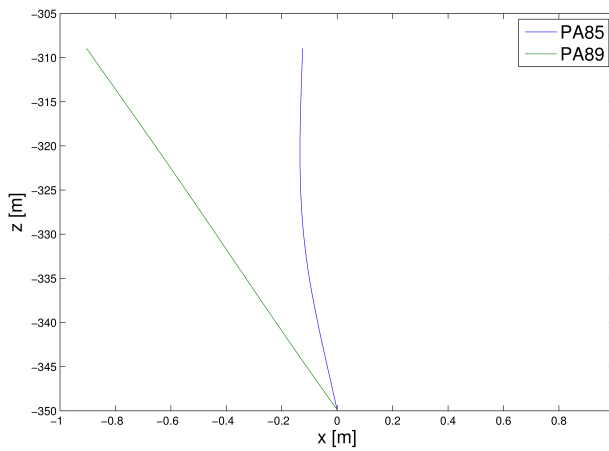


Figure 6.3: Riser configuration for PA

tory for the drop of two of the scenarios is shown in Figure 6.2. The configuration of the riser at the time step before the riser has contact with the bottom is taken as the input configuration of the buckling analysis. Table 6.3 shows the different sce-

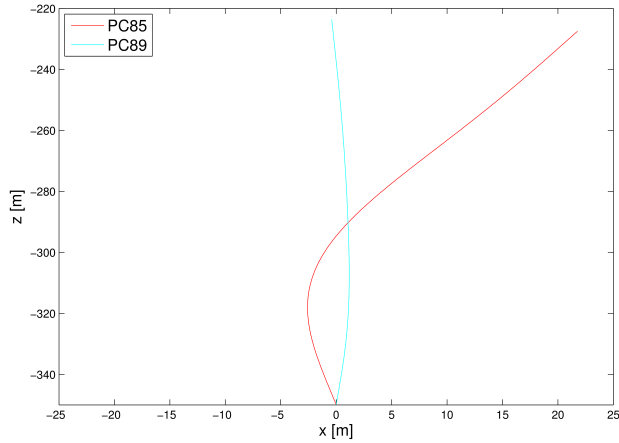


Figure 6.4: Riser configuration for PC

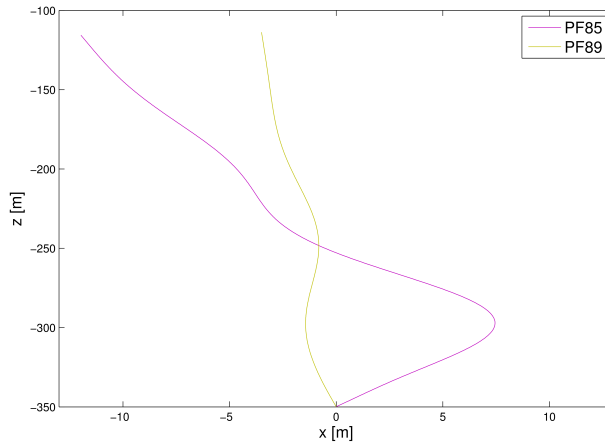


Figure 6.5: Riser configuration for PF

narios analyzed. The three different risers, PA, PC and PF, had different lengths. This resulted in different velocities at impact of the bottom.

Two drop angles were used, 85° and 89° . The impact velocities were very similar between the drop angles, so they were assumed the same. The configuration for the different scenarios is shown in Figure 6.3, Figure 6.4 and Figure 6.5 for riser PA, PC and PF respectively. The x-axis is scaled up to show the configurations clearly. Figure 6.6 shows the configuration in scale of the riser length.

The nodes of the risers in the earlier analyses were about 0.5 meters apart. For

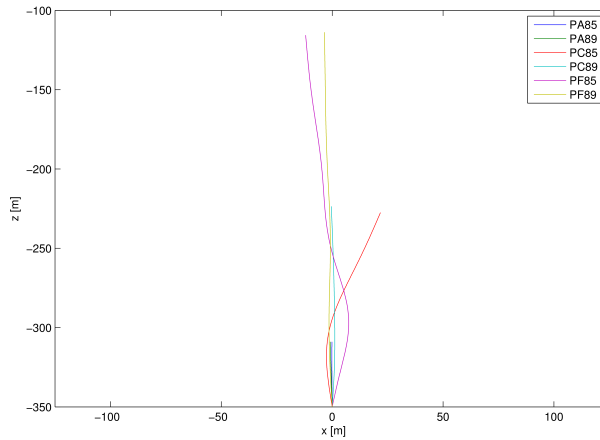


Figure 6.6: Riser configurations with no scaling

simplicity the nodes was used directly in USFOS. This means that the beam elements in USFOS were 0.5 meters long. This is much smaller than necessary for the analysis. The standard beam elements used in USFOS can replicate static buckling deformation with only one element, making the necessary elements over the riser mainly dependent on higher order buckling modes, and the accuracy of the shape of the riser. Since the analyses were not over a long time period the computational time were relatively short, so the element length was kept. One thing to note when using USFOS beam elements is that the ratio between the diameter and the length of the beam cannot be too large. USFOS limits the ratio to be larger than 2. The analyses are much lower than this limit but it is important to inspect the analysis for unusual element behavior when the beam elements are this small.

The speed was assumed to be only in the vertical direction. This would not be entirely correct. The riser would probably have velocity in x- and y-direction when the bottom was reached. These speeds would most likely be much smaller than the vertical speed. So the approximation was assumed to give a good idea of the buckling response. For a later analyses it could be an idea to include the effects of an impact with a velocity at an angle.

The bottom was modeled by two elements connected in series and then to the riser. One was modeled as a hyper-elastic spring element and the other one was modeled as an elastic-plastic spring element. The hyper-elastic spring connected to the riser was very soft at the beginning and very stiff after a given displacement. This was to simulate the contact force between the riser and the bottom. The stiffness of the soft part was negligible to the loads in the analysis and was used when the riser had not made contact with the bottom. The stiffness used was 10 N/m. The stiff part was much stiffer than the axial stiffness to the riser, and the elastic-plastic spring. The purpose of this stiffness was to transfer the axial force to the elastic-plastic

spring. The stiffness used was $1 \cdot 10^{13}$ N/m.

The second spring was used to reproduce the deformation of the bottom as the riser hit. The spring was modeled as an elastic-plastic riser beam element to get the desired effect in USFOS. The riser beam type was chosen since USFOS models it with a traditional beam shape function. This element does not take elastic buckling, plastic hinges, etc., into consideration. This combined with a generic beam cross section made it behave like an elastic-plastic spring.

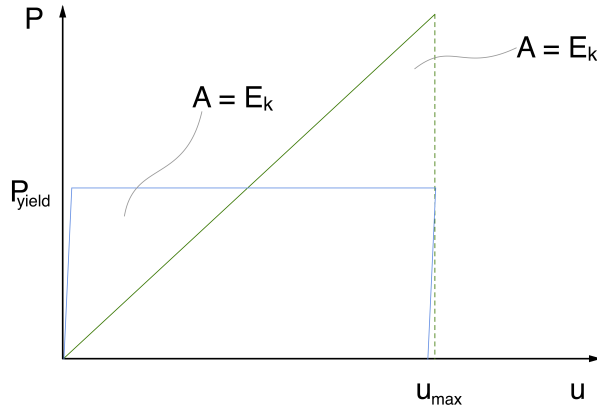


Figure 6.7: Sketch of the spring deformation and equivalent elastic-plastic behavior

In talks with M.Sc. Benjamin I. Brynstad a stiffness that gave a deformation between 0.5 meters and maximum 2.0 meters of the bottom was preferred. The desired deformation of the elastic-plastic spring was found by hand calculations. Energy calculations of a linear spring were used as basis. The energy absorbed of a linear spring can be expressed as

$$E_s = \frac{1}{2} k u_{max}^2 \quad (6.1)$$

where u_{max} was the axial displacement of the spring. The kinetic energy of the riser was set equal to the spring energy of the bottom. The kinetic energy is expressed in Equation (6.2). The added mass in the longitudinal direction is considered negligible.

$$E_k = \frac{1}{2} M \dot{u}^2 \quad (6.2)$$

The deformation of the spring at different stiffness could now be found. The elastic modulus of the spring was very stiff. This meant that the load-deformation curve of the beam was almost a rectangular shape, meaning that the absorbed energy could be approximated to

$$E_s \approx P_{yield} u_{max} \quad (6.3)$$

where P_{yield} is the maximum load in the spring. Using the kinetic energy and the given displacement of the beam, the yield strength of the elastic-plastic spring was calculated. This is illustrated in Figure 6.7. The deformation would not be the same as the hand calculation since the whole kinetic energy would not be absorbed by the spring. The riser itself will deform and absorb energy. The potential force from the gravity is not considered. And the energy calculations are assuming a one degree of freedom case. This would, though, give a good basis for the magnitude of the deformation. The reason the bottom was modeled as an elastic-plastic beam was that the ground should deform, but not spring back after the deformation had happened. By using a large elastic modulus and a yield strength, the beam would not go back after it as deformed.

Two different stiffness of the bottom was used. The different deformations used can be seen in table 6.4. The kinetic energy found in Table 6.5. The elastic stiffness used on the elastic-plastic spring was set to $8.50 \cdot 10^{11}$ N/m

Table 6.4: Stiffness used on bottom

Eq. linear stiffness	Riser	Spring def.	Spring yield load
$1.0 \cdot 10^7$ N/m	PA	0.60 m	$3.01 \cdot 10^6$ N
	PC	0.88 m	$4.39 \cdot 10^6$ N
	PF	1.12 m	$5.61 \cdot 10^6$ N
$1.0 \cdot 10^8$ N/m	PA	0.19 m	$9.53 \cdot 10^6$ N
	PC	0.28 m	$1.39 \cdot 10^7$ N
	PF	0.36 m	$1.77 \cdot 10^7$ N

The analyses were run on a very small time increment during the impact. When the impact was over, i.e., the spring did not deform and the bottom of the riser was stationary, a larger time increment was used to see how the riser behaved post impact. For the soft bottom the time increment was set to $5.0 \cdot 10^{-5}$ seconds during the impact, and $1.0 \cdot 10^{-3}$ seconds after. The stiffer bottom the time increment was $1.0 \cdot 10^{-5}$ seconds during the impact, and $1.0 \cdot 10^{-3}$ after. The softer bottom had the impact time increment for 0.2 seconds to ensure the impact was over, the stiffer bottom needed only 0.08 seconds for the impact. Both analyses were stopped after 2 seconds.

An elastic only analysis was done to see if the riser would buckle elastically on impact. If the riser yielded before it buckled, it would be interesting to see how much more capacity the riser would have before buckling became the limiting effect.

An eigenvalue analysis was also done on the risers. This would give us the eigenmode that could be induced by the impact duration. It could be interesting to

see if the eigenmode had any connection with the buckling mode. The eigenvalue analysis was done by fixing the top node of the risers, and keeping the bottom fixed for translation in the horizontal plane. The eigenvalues were found by using the Lanczos algorithm in USFOS. MATLAB was used to post-process the result.

Morrison theory was used for the added mass and damping forces. The mass and damping coefficient was set to $C_m = 2.0$ and $C_d = 0.7$ respectively. The structural damping for the riser was assumed dependent on Rayleigh damping. The damping ratio was set to 0.02 at 0.2 Hz and 2.0 Hz.

6.2 Result of the analysis

The mass was calculated by USFOS. The basis was the modeling of the production riser. The mass would probably not coincide exactly with the real mass. Partly because of the simplification discussed in Section 6.1. The result is considered good enough for the application. The velocity was given from another analysis. The kinetic energy for the whole riser was calculated. The result is shown in Table 6.5.

Table 6.5: Kinetic energy of the riser scenarios

Riser	Mass	Velocity at impact	Kinetic energy
PA	16 154 kg	15.0 m/s	$1.82 \cdot 10^6$ J
PC	26 617 kg	17.0 m/s	$3.85 \cdot 10^6$ J
PF	36 769 kg	18.5 m/s	$6.29 \cdot 10^6$ J

For the impact scenarios with a softer spring, the maximum axial load in the riser can be seen in Table 6.6

Table 6.6: Maximum axial load during an impact for a $1 \cdot 10^7$ N/m stiffness impact

Riser	Drop angle	Maximum axial load
PA	85°	$1.02 \cdot 10^6$ N
	89°	$1.02 \cdot 10^6$ N
PC	85°	$2.97 \cdot 10^6$ N
	89°	$3.13 \cdot 10^6$ N
PF	85°	$4.51 \cdot 10^6$ N
	89°	$5.03 \cdot 10^6$ N

The maximum axial load was larger for the scenarios with larger the length, and therefore mass. This was as expected. The risers dropped with a steeper angle was also larger than the other angle for all the riser lengths. This was a result of the configuration of the riser since the impact velocity were the same. The deformations from the analyses appeared to be in the elastic area of the riser. Looking at the stress in the risers confirmed that no part of the riser yielded.

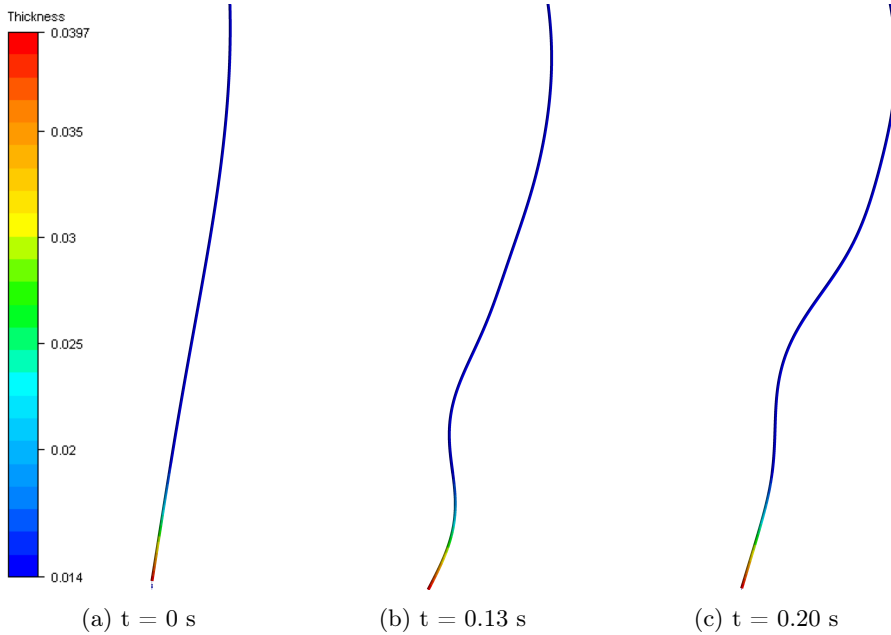


Figure 6.8: Riser deformation during impact for scenario PF at 85° and scale = 5

The deformation of the risers was not very large. The before and after impact of the riser end in scenario PF85 can be seen in Figure 6.8. The deformations are scaled up with a factor of 5 and the thickness is represented in the color scale to indicate the tapered section.

The PF-riser had the largest deformation of the different risers for the soft bottom. The riser began to buckle where the tapered section was part of the buckling mode. After the riser buckled, a buckling wave traveled upwards the riser. It were only the PF-riser scenarios that had any noticeable buckling, although all the scenarios had lateral displacement during the impact.

For the analyses with larger stiffness of the bottom is shown in Table 6.7. Also in this case the maximum axial load increased as the drop angle and mass increased. Though, in these analyses the increase was not as substantial as for the softer bottom.

Also with this stiffness of the bottom, the bottom of the riser did not yield. For the longest risers, i.e., PF and PC, did however yield. This can be seen on Figure

Table 6.7: Maximum axial load during an impact for a $1 \cdot 10^8$ N/m stiffness impact

Scenario	Drop angle	Maximum axial load
PA	85°	$3.30 \cdot 10^6$ N
	89°	$3.30 \cdot 10^6$ N
PC	85°	$7.34 \cdot 10^6$ N
	89°	$7.36 \cdot 10^6$ N
PF	85°	$8.04 \cdot 10^6$ N
	89°	$8.06 \cdot 10^6$ N

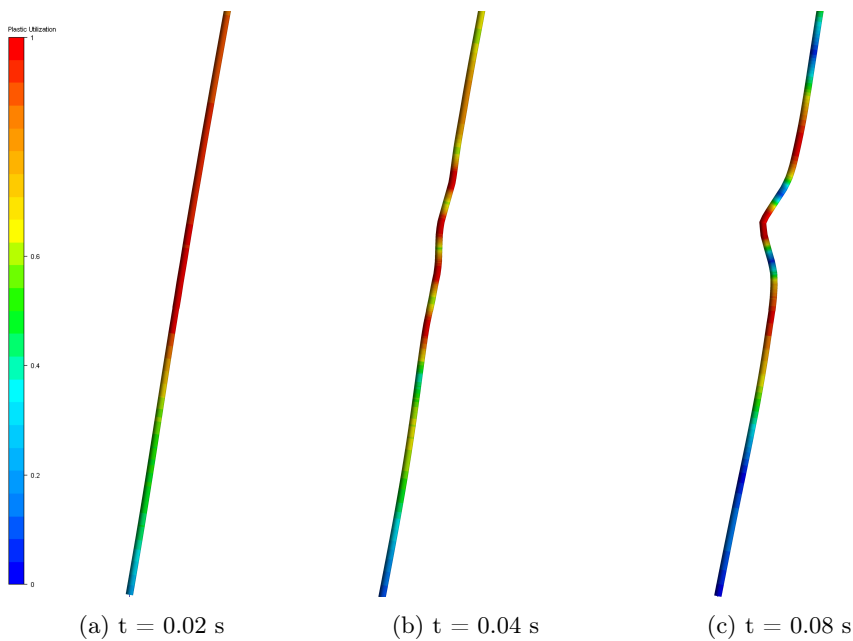


Figure 6.9: Riser deformation during impact for scenario PF at 85°

6.9. The riser developed plastic hinges right above the tapered section. Figure 6.10 shows where the tapered section begins relative to the plastic hinge. These figures are of the PF85 scenario. The same response was seen on the other riser scenarios that yielded. The hinges developed right above the tapered section. Figures of some of the other scenarios can be seen in Appendix C.2.1.

The energy absorbed by the spring in the ground is shown in Table 6.8 and 6.9. The axial force in the spring was integrated over the displacement, using MATLAB. The energy was extracted when the deformation of the spring was done for all analyses.

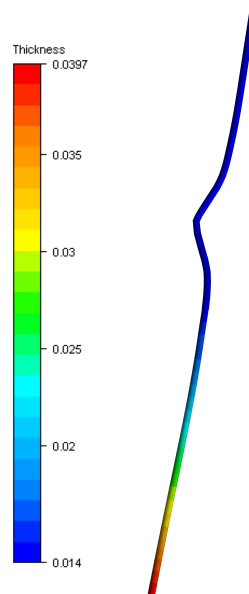


Figure 6.10: Representation of wall thickness for PF at 85°

Table 6.8: Energy absorbed in softer spring used on bottom

Riser	Drop angle	Spring energy
PA	85°	$1.90 \cdot 10^6$ J
	89°	$1.90 \cdot 10^6$ J
PC	85°	$3.40 \cdot 10^6$ J
	89°	$3.56 \cdot 10^6$ J
PF	85°	$5.12 \cdot 10^6$ J
	89°	$6.01 \cdot 10^6$ J

In Table 6.8 it can be seen that the kinetic energy of the riser has a correlation to the amount of energy absorbed in the spring. The absorbed spring energy becomes larger when the kinetic energy is larger. This is, though, not a linear relationship. The increase in spring energy is not as large as the increase in kinetic energy for the different risers.

For Table 6.9 the correlation between kinetic and absorbed energy breaks down. In this case the risers that had the least amount of kinetic energy has almost the largest absorbed spring energy. The main difference between the response from the softer and the stiffer bottom is that the longest risers started to yield in the latter analysis.

Table 6.9: Energy absorbed in stiffer spring used on bottom

Riser	Drop angle	Spring energy
PA	85°	$1.60 \cdot 10^6$ J
	89°	$1.59 \cdot 10^6$ J
PC	85°	$1.35 \cdot 10^6$ J
	89°	$1.84 \cdot 10^6$ J
PF	85°	$1.43 \cdot 10^6$ J
	89°	$1.45 \cdot 10^6$ J

6.2.1 Elastic analysis

The analyses were repeated without a yield capacity, so the scenario was in the elastic area. As the softer stiffness run did not have any yielding, the results were the same with the elastic material. For the stiffer stiffness, the result of maximum axial load can be seen in Table 6.10

Table 6.10: Maximum axial load during an elastic impact for a $1 \cdot 10^8$ N/m stiffness impact

Scenario	Drop angle	Maximum axial load
PA	85°	$3.30 \cdot 10^6$ N
	89°	$3.30 \cdot 10^6$ N
PC	85°	$8.20 \cdot 10^6$ N
	89°	$8.45 \cdot 10^6$ N
PF	85°	$9.10 \cdot 10^6$ N
	89°	$9.25 \cdot 10^6$ N

The increase in maximum axial load was more like the first analyses, where the impact was in the elastic area. The maximum axial load was increased for all the analyses, except for the PA-riser. These scenarios did not yield when the elastic-plastic material was used.

Looking at the impact behavior of the risers, it was seen that the lateral deformation resembled buckling, though, the deformation was not very large. In Figure 6.11 the impact of PF85 can be seen. The deformation is scaled by a factor of 5 and the colors represent the wall thickness of the riser. Like the earlier analysis, this was the scenario with the largest deformation during impact. The riser buckles with half-waves at the bottom, but the rest of the riser has not reacted to the

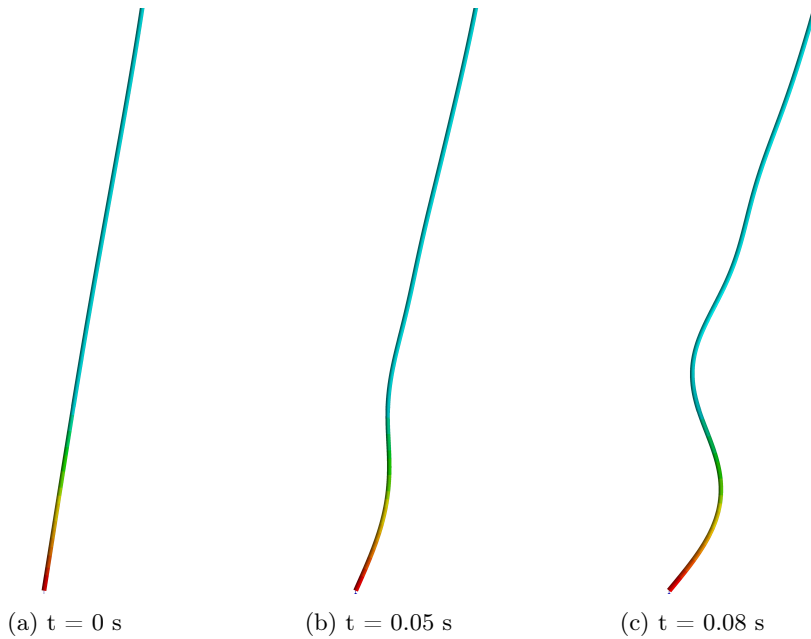


Figure 6.11: Comparison of riser before and after impact for scenario PF at 85° and scale = 5

impact. This resembles the buckling shape of the tension leg of the SWAY-concept in Chapter 5. For comparison, Figure 5.16 has a similar buckling shape.

6.2.2 Eigenvalue analysis

The load history for the bottom spring in the PF85-scenario and a high stiffness bottom can be seen on Figure 6.12. This is for the elastic impact case. From this figure the impact duration can be set to 0.0869 seconds. This could be looked at as a half period, and the corresponding period would then be 0.174 seconds. The closest eigenperiod for the PF-riser was 0.176 seconds. This eigenmode is shown in Figure 6.13a. The wavelength of this shape is very similar to the wavelength of the buckling mode in Figure 6.11.

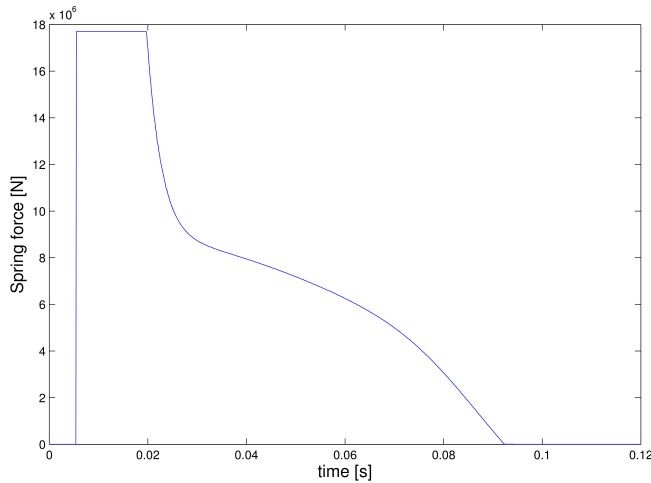
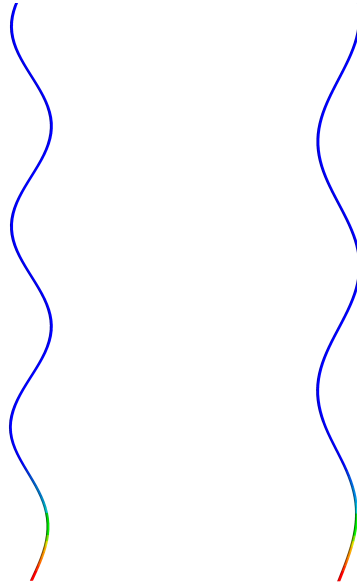


Figure 6.12: Load history for the bottom spring, scenario PF85

Doing the same comparison for the softer bottom, the impact duration can be set to 0.136 seconds. This gives the period of 0.272 seconds, which the closest eigenperiod is 0.274 seconds. The eigenmode corresponding to this is seen in Figure 6.13b. Also in this case, the wavelengths look very similar to the buckling wavelength in Figure 6.8.

The wave amplitude for the eigenmode was smaller at the bottom of the riser than at the rest. This was the case for both the selected eigenmodes. This is barely noticeable, but can be seen in Figure 6.13.

The same analysis was done for rest of the scenarios. These are presented in Table 6.11 and 6.12.



(a) Eigenperiod of 0.176 s (b) Eigenperiod of 0.274 s

Figure 6.13: Eigenmodes for the PF-riser

Table 6.11: Eigenperiods for bottom stiffness $1.0 \cdot 10^7$ N/m

Scenario	Impact duration	Impact period	Nearest eigenperiod
PA85	0.105 s	0.211 s	0.209 s
PA89	0.105 s	0.211 s	0.209 s
PC85	0.131 s	0.261 s	0.251 s
PC89	0.136 s	0.272 s	0.251 s
PF85	0.136 s	0.272 s	0.274 s
PF89	0.159 s	0.317 s	0.313 s

Table 6.12: Eigenperiods for bottom stiffness $1.0 \cdot 10^8$ N/m

Scenario	Impact duration	Impact period	Nearest eigenperiod
PA85	0.0452 s	0.0904 s	0.0941 s
PA89	0.0452 s	0.0904 s	0.0941 s
PC85	0.0584 s	0.117 s	0.122 s
PC89	0.0629 s	0.126 s	0.122 s
PF85	0.0869 s	0.174 s	0.176 s
PF89	0.102 s	0.204 s	0.198 s

6.3 Discussion of the result

6.3.1 Energy considerations

The energy dissipated in the spring, calculated in Table 6.8 and 6.9, was compared to the total energy in the system, when approximating the problem as a one degree of freedom problem. The total energy was calculated as the kinetic energy from the initial velocity, and the potential energy. The potential energy was assumed from the height difference from the bottom of the riser at the start, and at the end of the analysis. The one degree of freedom approach does not take into account that the vertical kinetic energy can be transferred to kinetic energy in other directions. The energy calculation also had the assumption that the riser had a lumped mass at the bottom, so the whole riser moved as one point. This will be a conservative estimate of the total energy in the system. The result can be seen in Tables 6.13 and 6.14.

Table 6.13: Energy comparison for bottom stiffness $1.0 \cdot 10^7$ N/m

Scenario	Absorbed energy	Total energy	Amount absorbed
PA85	$1.90 \cdot 10^6$ J	$1.93 \cdot 10^6$ J	98.3 %
PA89	$1.90 \cdot 10^6$ J	$1.93 \cdot 10^6$ J	98.3 %
PC85	$3.40 \cdot 10^6$ J	$4.08 \cdot 10^6$ J	83.4 %
PC89	$3.56 \cdot 10^6$ J	$4.08 \cdot 10^6$ J	87.1 %
PF85	$5.12 \cdot 10^6$ J	$6.66 \cdot 10^6$ J	77.0 %
PF89	$6.00 \cdot 10^6$ J	$6.77 \cdot 10^6$ J	88.7 %

As the Table 6.13 shows, for the most part, most of the riser energy gets dissipated in the spring. The PA-riser has almost all the energy been transferred to the spring. With visual inspection of the analysis confirmed that the whole riser had no vertical velocity, so there was minimal kinetic energy left in the system. Figure 6.14 shows the velocity of the top node for the different risers with a drop angle of 85 degrees. For the PA85 scenario the top has no vertical velocity after about 0.12 seconds. The same was true for the PA89 scenario. This means that the rest of the total energy is most likely going to strain energy in the riser. This can be both axial and bending strain. As the velocity at the top of the riser was zero and, as noted in Section 6.2, there was little lateral movement. This indicates that buckling is not happening for the PA-riser.

In the PC- and PF-riser there were a smaller percentage of the energy that were absorbed by the spring. As Figure 6.14 shows, there is still vertical velocity in the two longest risers after 0.2 seconds. All the risers had stopped in the bottom after about 0.1 seconds. There is also no indication of the top of the two riser are about to stop. Looking at the result after 0.2 seconds confirmed that the top of

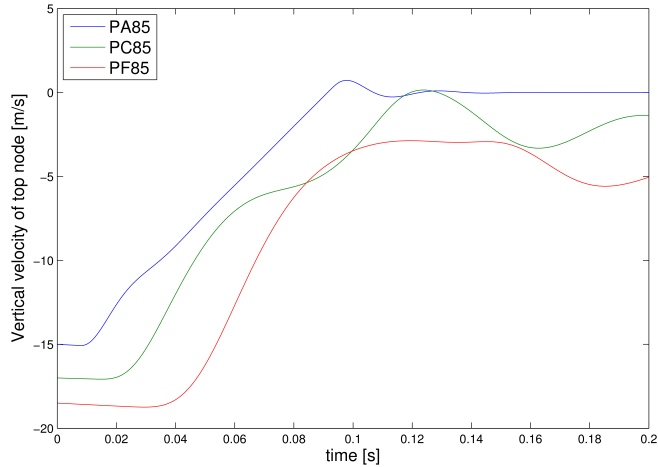


Figure 6.14: Vertical velocity of riser top for the softer bottom

the risers did not stop, and continued to fall until the whole analyses were done after 2 seconds. This means that there is still kinetic energy at the end of these results. The amount of mass that still moves is complicated to find, so there is not an easy way to find the kinetic energy left in the systems. Combined with strain energy is mainly where the rest of the systems energy is. As the longer risers are very curved when hitting the ground, there is probably not much pure axial strain in the riser. This means that most of the deformation energy will be bending strain. Since there is still velocity at the top of the risers, means that the risers still deform. This can indicate that global buckling is induced in the risers, although this is mainly because of the configuration of the riser when hit.

Table 6.14: Energy comparison for bottom stiffness $1.0 \cdot 10^8$ N/m

Scenario	Absorbed energy	Total energy	Amount absorbed
PA85	$1.60 \cdot 10^6$ J	$1.86 \cdot 10^6$ J	85.8 %
PA89	$1.59 \cdot 10^6$ J	$1.86 \cdot 10^6$ J	85.6 %
PC85	$1.35 \cdot 10^6$ J	$3.90 \cdot 10^6$ J	34.7 %
PC89	$1.84 \cdot 10^6$ J	$3.91 \cdot 10^6$ J	47.2 %
PF85	$1.43 \cdot 10^6$ J	$6.36 \cdot 10^6$ J	22.5 %
PF89	$1.45 \cdot 10^6$ J	$6.36 \cdot 10^6$ J	22.8 %

For the stiffer bottom, the risers yield. The amount of absorbed spring energy can be seen in Table 6.14. This makes the force acting on the spring much smaller than

estimated. The exception is the PA-riser, which does not yield. In these analyses the smallest riser have the largest amount of energy absorbed by the spring by a good margin. This have however smaller absorbed energy than the softer bottom run. The top of the riser has stopped, so there is not much kinetic energy left. This means that the riser have to deform more that the previous case. This is logical, since the bottom is stiffer, the riser will take more deformation. From visual inspection of the deformation, it looks like the lateral deformation is also larger, but still not large. So also here there is indication that the axial deformation is the dominating part of the deformation. For the longer risers, that is the PC- and PF-riser, the yielding of the cross section created three plastic hinges on the riser. This meant that there will not be an increase in load, or deformation of the bottom. This is why the amount of dissipated energy in the spring is much lower than the previous analyses. The risers still have much kinetic energy when the yielding takes place. This means that there probably will be less strain energy deforming the riser other than at the plastic hinges.

The trend is that the amount of energy dissipated in the spring is less for longer risers and stiffer bottom. It can also be concluded that there is a connection between the amount of lateral deformation and amount of energy dissipated in the spring. From the analyses run it can be concluded that the runs where the least amount of energy, relative to the total, have the most lateral displacements and where buckling is most likely induced.

6.3.2 Deformation of the risers

The lateral deformations of the riser are dependent on the configuration of the riser as the impact happens. The analyses with a drop angle of 89° have risers in a straighter configuration than the analyses with an 85° drop angle. This gives a higher maximum axial load in Table 6.6 and 6.7. The deformation became naturally larger for the higher axial load. The risers with an 89° drop angle had also smaller lateral deformations. This indicates that the configuration of the riser, when hitting the bottom, is important if the riser buckles or not.

Figure 6.8 shows that the riser deforms laterally at the bottom, where the thickness is larger than for the rest of the riser. It looks like the half-wave that gets generated under the impact doesn't get affected by the increase in thickness that much. As the time increases the buckling wave travels up the riser. This effect may be explained by a much larger lateral movement further up on the riser. This moves out laterally during the impacts, and at $t = 0.2$ seconds, the half-wave gets straightened out by the larger lateral deformation. The buckling wave will now travel up the riser as the bottom of the riser gets smaller compressive forces. A larger part of the riser at $t = 0.2$ seconds can be seen in Figure 6.15. Here the larger wave can be seen, and the smaller buckling wave traveling upwards. The figure is scaled with a factor of 5.

As discussed above, the longest risers dropped with the most gradual angle are



Figure 6.15: Buckling wave traveling, PF85 at $t = 0.2$ and scale = 5

the scenarios that look like buckling takes place. While the shortest riser with the steepest angle looks like no significant buckling takes place. Looking at the results of the softer bottom, the axial load in the riser was compared to the change in the height of the riser. For the smallest riser, the shape was almost the same. In Figure 6.16 the relative displacement between the top and bottom of the riser and axial load was plotted and scaled to compare. As most of the relative displacement of the riser is a pure axial deformation. This means that the lateral deformation of the riser is not big, and the riser has most likely not buckled. This coincides with the previous results discussed. After a while the relative displacement started to increase. This was because the riser started to tip over.

The longest riser had a very different shape for the relative displacement and the axial force. In Figure 6.17 the comparison can be seen. As the impact is over, the axial load is small for the riser, while the relative displacement is growing without any sign of stopping. This means that the relative displacement is not very dependent on the axial deformation of the riser. This indicates that mainly bending strain deforms the riser.

The same trend that Figure 6.17 shows can be seen for the PC-riser. The difference between the shortest riser and the two others is that the lateral deformation does not increase rapidly as the time increases. A possible explanation for this can be that the configuration of the PA-riser is much more straight than the others. This means that the bending stress in the riser will be much smaller during the impact, and the riser will not bend out laterally that much. Another effect that contributes is that the risers have the same cross section, but different mass. This means that

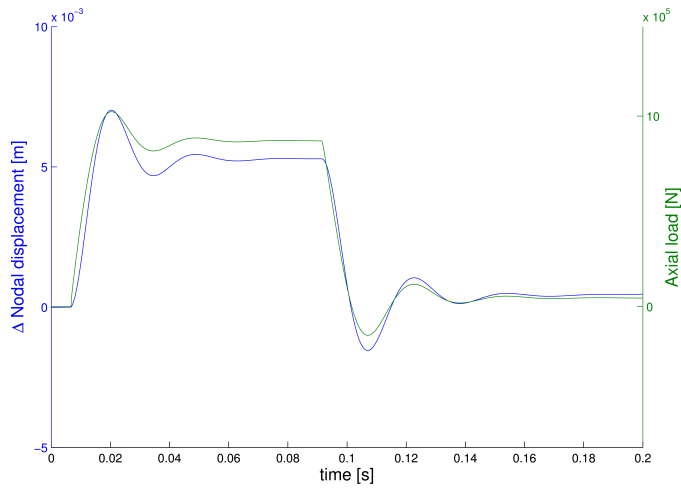


Figure 6.16: The force and relative displacement of the PA-riser

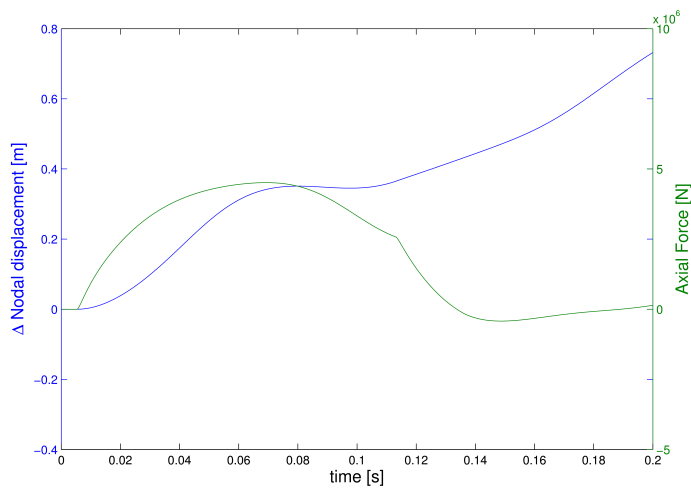


Figure 6.17: The force and relative displacement of the PF-riser

for the long risers the stress is much greater.

Looking at the behaviors of the riser after the impact show a clear difference between the PA-riser and the PC-and PF-risers. For PA, the riser collapsed by falling on its side. This means that this riser will not buckle more than it already have. The two other riser lengths, on the other hand, did start to collapse upon themselves. The top of the riser was in about the same place as when the analysis

started, in the horizontal plane. The axial and bending stiffness of the riser was not enough to hold it upright, and it started to have large lateral deformations. The start of the collapse for PF85 can be seen in Figure 6.18. This collapse mode would happen even though if the risers did not have any velocity. The configuration of the riser is too curved to withstand its own gravitational force.

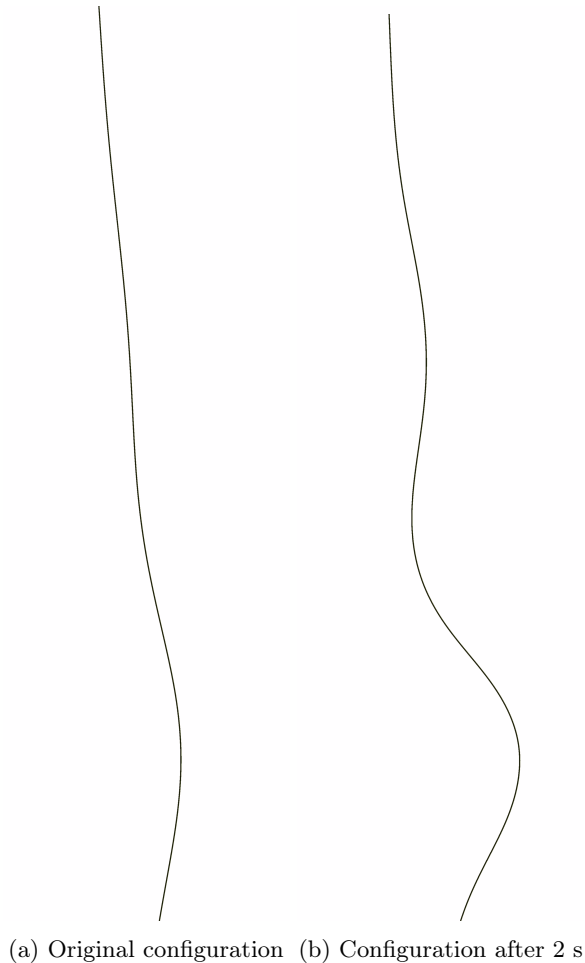


Figure 6.18: Collapse mode for the PF85 scenario

The stiffer bottom analyses had about the same behavior for the PA-riser. The lateral deflection during impact was not large, and the riser was falling down on its side when the impact was over. The impact force was naturally larger for a stiffer impact, but there were not much indication of a buckling behavior.

For the longer risers the yield capacity was the dominating factor of failure. As the axial load became large enough, the cross section started to yield. Here, the

thickness of the riser wall was important. When the risers buckled for the softer bottom, the increase in thickness, and bending stiffness, appeared not to influence the lateral deflection. For the stiffer bottom case, the riser started to yield at the cross section right before the tapered section. The course of events was about the same for all the scenarios where the risers yields, and are shown in Figure 6.9. The riser started with a relative large area above the tapered section that started to yield. This created instability and the risers started to move out laterally. The deformation stabilized as three plastic hinges. Because of this collapse form, the mass above the hinges will not contribute to additional axial load is transferred to the spring. This deformation will probably give tearing in the riser wall as the riser collapses.

6.3.3 Elastic analysis

As the collapse of the risers were dominated by the yield capacity of the riser, it was interesting to see how the risers would behave as an elastic material. The stiffer bottom was repeated without a yield load for the steel. The result was similar to the softer bottom, only a more substantial response. The riser buckles at the bottom while the rest of the riser does not. This can partly be explained by the speed of the stress propagation.

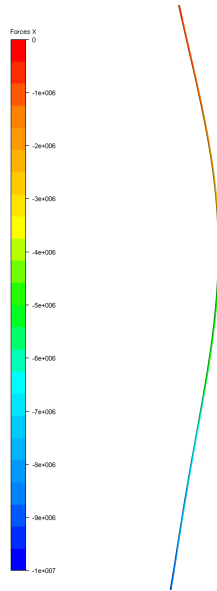


Figure 6.19: Stress propagation for the PF-riser at 85° at 0.02 s

As Figure 6.19 shows, the PF-riser has about the maximum compressive force in the bottom, while the riser is almost stress free 100 meters above. This means that the bottom of the riser starts to buckle before the stress from the impact reaches

the top, for the longest riser. Using Equation (4.6) the stress reaches the top of the PF-riser after $t = 0.046$ seconds. Comparing to the time on Figure 6.11, the riser has already begun to buckle. This means that the length of the riser that has compression forces above the buckling capacity, is smaller than the riser length. The part that buckles will therefore only be a part of the bottom of the riser. The length of the part that buckles is dependent on its own length, since the slenderness is an important factor of buckling capacity. This combined with dynamic effects make the length of the part that buckles hard to predict.

6.3.4 Eigenvalue analysis

From the eigenvalue analyses the eigenmodes for the relevant periods were found. The impact was idealized as half a period, and the corresponding eigenperiod was found as the closest to the impact period. The PF-riser was used, as this was the only riser that the buckling mode could be seen reasonably.

As noted in Section 6.2 the eigenmodes was very similar to the buckling mode at the riser end. A closer comparison between the wavelength of the eigenmode and the buckling mode were done. For the soft bottom the PF85 had a buckling wavelength of about 31 meters. The wavelength for the eigenmode corresponding to the impact duration had a wavelength of about 32 meters. For the stiff bottom, the buckling mode had a wavelength of about 26 meters, while the eigenmode had a wavelength of 25 meters.

The wavelength for the buckling modes of the bottom of the riser corresponded very well to the eigenmodes. They could be assumed to be the same. The buckling wave did die out after about one wave for both the stiffness, so the uncertainty is quite large when measuring the wavelength.

The result is very similar to the SWAY tension leg in Section 5.3.2. In this result, though, the difference between the eigenmode and the buckling mode is not that clear. Without more analyses, it is hard to draw a conclusion of which result that gives the most correct notion of the connection. The eigenperiods have about the same magnitude as the SWAY periods, but the riser is more than twice the length of the tension leg. This means that the stress propagation is more dominating in this analysis. The applied load in the riser case is not a correct sinusoidal load, as is the case for the tension leg. These effects would probably explain some of the different result. Although, the discussion for the connection between buckling mode and eigenmode for the tension leg in Section 5.3.2 is valid for this case as well.

6.4 Conclusion

From the analyses it was clear that the shortest riser did not buckle. The riser did not yield either in any of the analyses. This meant that most of the energy was

transferred to the spring. This means that if a subsea construction gets hit by the PA-riser almost all of the energy in the riser goes to deformation of the riser and the construction. Although, the lateral deformation became larger as the stiffness of the spring increased, so the riser could buckle or yield if the impact stiffness became large enough. The riser started to tip over when the analyses stopped. This could give more damage to constructions to the sides of the riser.

For the longer risers, there was an indication that some form of buckling took place. The bottom of the risers got some buckling, but the buckling deflection was so small that it probably did not have any noticeable effect. The yielding of the riser cross section was the effect that gave the most reduction in energy dissipation in the bottom spring. This led to formation of plastic hinges that made much less of the energy get transferred to the bottom.

The collapse of the risers for the softer spring was probably most because of the configuration. The risers did collapse because of the large that were caused of the long drop.

The comparison between the eigenmode and the buckling mode did show that there is probably a connection. The eigenmode and buckling mode were very similar. The exact relationship did, however, not get found. This could be a topic in further work.

The risers should be run with a realistic stiffness of the subsea construction to see how much energy that gets dissipated in deformation of the construction. The velocity the risers had when hit the bottom, should be done more realistically. That means that the riser would have a velocity at an angle of the bottom.

Chapter 7

Conclusion

In this thesis a review of analytical solution to the dynamic buckling problem has been done for both beams and plates. The governing methods for solving dynamic buckling problems with a finite element method have also been presented. The overall conclusion from this review was that the structures increased their buckling capacity when dynamic effects are considered.

An unstiffened plate was considered. The dynamic buckling behavior for the plate was investigated. Both displacement of the plate end, and force loading was used. The analyses of the plate were done in Abaqus FEA, USFOS, and an analytical solution using MATLAB. The results were that the dynamic effect limited the deformation of the plate during the loading, and therefore increased its capacity. In a dynamic analysis, a plate will continue to have resistance even after buckling has occurred. This means that the yield stress will probably be the limiting factor for the capacity.

Dynamic buckling of the tension leg of the SWAY wind turbine was revisited from the project work. This time the analyses focused on the effect of amplitude and duration of a sinusoidal displacement of the spar buoy. The buckling capacity of the tension leg would give insight in the increase of capacity of a slender beam. The analyses showed that the buckling capacity could increase above the yield capacity. For some of the loading duration the buckling mode gave a large loading in tension in the straightening phase. This tension force could be larger than the compressive force, and were above the yield capacity for several cases.

An impact analysis of a dropped production riser from a platform was done. The effect of buckling during impact was investigated. The energy transferred from the riser impact was used as an indication on the buckling of the riser. It was found that the length and configuration of the riser did influence the buckling response. The longer risers with the most curved configuration did transfer the least amount of its kinetic energy during the impact. As with the SWAY tension leg, the yield stress was the dominating effect on such short durations. The buckling mode that

the riser buckled in was about the same as the eigenmode corresponding to the impact duration. This means that the eigenperiod can affect the buckling capacity.

Chapter 8

Further work

In this thesis much of the basic effect that dominate the dynamic buckling has been investigated. For further work it is recommended that more advanced analyses of the same thematic is done. Combining the effect of dynamic buckling with other types of loading and members in the models.

For the analysis of dynamic buckling of unstiffened plates the following work is recommended to expand upon. It would be interesting to try to find a design formulation for the capacity of the plate, with dynamic effects included. An analysis of dynamic buckling of plate in more complex structure and realistic loading. This would give a better understanding in how dynamic buckling gets affected by other boundary conditions and loads.

The SWAY concept has been analyzed in both this thesis and the project thesis. There is still more to find out about the effect of dynamic buckling, however. A more realistically case where current and winds are applied. The displacement loading can be replaced with an actual wave load applied to the spar buoy. This would give a more genuine response of the tension leg, and the practical amplification of the capacity could be investigated.

For the impact of the production riser on a subsea structure only an introductory analyses was done. The subsea structure that the riser hits could be modeled with real geometry and material. This would give a more realistic energy calculation and deformation of the riser.

For a more general case, a relationship between the buckling mode and eigenmode can be derived. This could be done for both beams and plates. Insight in how eigenperiods affect the buckling modes could be very helpful in design formulations where dynamic buckling is included.

References

- Abaqus 6.12 Documentation. Theory manual, 2012.
- Jørgen Amdahl. Chapter 3: Buckling of stiffened plates. In *TMR 4205 Buckling and Ultimate Strength of Marine Structures*. Department of Marine Technology, 2013.
- Shijie Cui, Hee Kiat Cheong, and Hong Hao. Experimental study of dynamic buckling of plates under fluid-solid slamming. *International Journal of Impact Engineering*, 1999.
- Shijie Cui, Hong Hao, and Hee Kiat Cheong. Numerical analysis of dynamic buckling of rectangular plates subjected to intermediate-velocity impact. *International Journal of Impact Engineering*, 2001.
- R. E. Ekstrom. Dynamic buckling of a rectangular orthotropic plate. *AIAA Journal*, pages 1655–1659, December 1973.
- Ivar Langen and Ragnar Sigbjörnsson. *Dynamisk analyse av konstruksjoner*. SINTEF, 1979.
- Carl M. Larsen. *TMR 4182 Marin Dynamikk*. Department of Marine Technology, 2012.
- Bernt J. Leira. *TMR 4170 Marine Konstruksjoner Grunnkurs*. Department of Marine Technology, 2011.
- Herbert E. Lindberg. *Little Book of Dynamic Buckling*. LCE Science/Software, September 2003.
- Torgeir Moan. *TMR 4190 Finite Element Modelling and Analysis of Marine Structures*. Department of Marine Technology, 2003.
- Tore H. Søreide, Jørgen Amdahl, Ernst Eberg, Tore Holmås, and Øyvind Hellan. USFOS - a computer program for progressive collapse analysis of steel offshore structures. Theory manual, 1993.
- Jonas Gullaksen Straume. Dynamic buckling of marine structures. Project thesis, December 2013.

USFOS User's Manual. Input description USFOS control parameters, 2012.

George Z. Voyiadjis and Pawel Woelke. *Elasto-Plastic and Damage Analysis of Plates and Shells*. Springer Berlin Heidelberg, 2008.

Appendices

Appendix A

Unstiffened plate analyses

A.1 MATLAB-code for the numeric time integration

```
1 clear all
2 a = 2.4;      %Length of the plate
3 b = 0.8;      %Width of the plate
4 E = 2.11e11;  %Youngs modulus
5 h = 0.01;     %Plate thickness
6 A = h*b;      %Cross section area
7 rho = 7850;  %Material density
8 mu = 0.3;     %Poissons ratio
9
10 ts = 0.02;   %Time end
11 dt = 1e-7;   %Time step
12 t = 0:dt:ts;
13 k = 0;
14
15 f = zeros(size(t));
16 w = f;
17 a_z = f;
18 P = f;
19 G = f;
20 f_0 = 0.001; %Amplitude of initial imperfection
21 f(1) = f_0;
22 n = 1;       %Half-waves over the width
23 m = 7;       %Half-waves over the length
24
25 M = rho*A;
26 K = E*A*h^2*pi^4/(12*(1-mu^2))*((m/a)^4+2*(m*n/(a*b))^2+(n/b)^4);
27
28 for i = t(1:(length(t)-1))
29     k = k + 1;
30
```

```

31     P(k) = -E*A/a*( (m*pi)^2/(8*a)*(f(k)^2-f_0^2)-u*t(k));
32     G(k) = E*A/24*pi^4*( (m/a)^4+(n/b)^4)*(f(k)^2-f_0^2);
33     a_z(k) = (-K*(f(k)-f_0)+(m*pi/a)^2*P(k)-G(k))*f(k)/M;
34     w(k+1) = w(k) + a_z(k)*dt;
35     f(k+1) = f(k) + w(k)*dt;
36 end
37
38 P(k+1) = -E*A/a*( (m*pi)^2/(8*a)*(f(k+1)^2-f_0^2)-u*t(k+1));

```

A.2 Python script for Abaqus analyses

```

1  # -*- coding: mbc -*-
2  from part import *
3  from material import *
4  from section import *
5  from assembly import *
6  from step import *
7  from interaction import *
8  from load import *
9  from mesh import *
10 from optimization import *
11 from job import *
12 from sketch import *
13 from visualization import *
14 from connectorBehavior import *
15
16 ForceAmpList = [1, 2, 5, 7, 9, 10, 15, 20, 25, 30, 35, 40, 50, 60, 70, 80, 90, 100]
17 T0 = 0.01298
18 T = [T0/10, 2*T0/10, 3*T0/10, 4*T0/10, 5*T0/10, 6*T0/10, 7*T0/10, 8*T0/10,
19      9*T0/10, T0]
20 T = [x/1.5 for x in T]
21
22 ## IMPORT MODEL ##
23 mdb.ModelFromInputFile(inputFileName=
24     'V:/Masteroppgave/Abaqus/Unstiff_plate_model/Unstiff_plate_n=3_exp.inp', name=
25     'Unstiff_plate_n=3')
26
27 ## APPLY CONSTRAINT ##
28 mdb.models['Unstiff_plate_n=3'].Equation(name='Upper_Constraint', terms=((1.0,
29     'PLATE-1.UPPER_LINE', 2), (-1.0, 'PLATE-1.UPPER_NODE', 2)))
30 mdb.models['Unstiff_plate_n=3'].Equation(name='Lower_Constraint', terms=((1.0,
31     'PLATE-1.LOWER_LINE', 2), (-1.0, 'PLATE-1.LOWER_NODE', 2)))
32 mdb.models['Unstiff_plate_n=3'].Equation(name='Left_Constraint', terms=((1.0,
33     'PLATE-1.LEFT_LINE', 1), (-1.0, 'PLATE-1.LEFT_NODE', 1)))
34
35 ## APPLY LOAD ##
36 mdb.models['Unstiff_plate_n=3'].ExplicitDynamicsStep(maxIncrement=0.00001, name=
37     'Step-1', previous='Initial', timePeriod=0.03)
38 mdb.models['Unstiff_plate_n=3'].ExplicitDynamicsStep(maxIncrement=0.0001, name=
39     'Step-2', previous='Step-1', timePeriod=0.06)
40 mdb.models['Unstiff_plate_n=3'].SmoothStepAmplitude(data=((0.0, 0.0),
41     (T[0], 0.309), (T[1], 0.5878), (T[2], 0.809), (T[3], 0.9511), (T[4], 1.0),
42     (T[5], 0.9511), (T[6], 0.809), (T[7], 0.5878), (T[8], 0.309),

```

```

43         (T[9], 0.0), (0.03, 0.0)), name='Sin_Amp', timeSpan=STEP)
44     mdb.models['Unstiff_plate_n=3'].rootAssembly.Surface(face4Elements=
45     mdb.models['Unstiff_plate_n=3'].rootAssembly.instances['PLATE-1'].
46     elements[0:1]+\
47     mdb.models['Unstiff_plate_n=3'].rootAssembly.instances['PLATE-1'].
48     elements[50:51]+\
49     mdb.models['Unstiff_plate_n=3'].rootAssembly.instances['PLATE-1'].
50     elements[100:101]+\
51     mdb.models['Unstiff_plate_n=3'].rootAssembly.instances['PLATE-1'].
52     elements[150:151]+\
53     mdb.models['Unstiff_plate_n=3'].rootAssembly.instances['PLATE-1'].
54     elements[200:201]+\
55     mdb.models['Unstiff_plate_n=3'].rootAssembly.instances['PLATE-1'].
56     elements[250:251]+\
57     mdb.models['Unstiff_plate_n=3'].rootAssembly.instances['PLATE-1'].
58     elements[300:301]+\
59     mdb.models['Unstiff_plate_n=3'].rootAssembly.instances['PLATE-1'].
60     elements[350:351]+\
61     mdb.models['Unstiff_plate_n=3'].rootAssembly.instances['PLATE-1'].
62     elements[400:401]+\
63     mdb.models['Unstiff_plate_n=3'].rootAssembly.instances['PLATE-1'].
64     elements[450:451]+\
65     mdb.models['Unstiff_plate_n=3'].rootAssembly.instances['PLATE-1'].
66     elements[500:501]+\
67     mdb.models['Unstiff_plate_n=3'].rootAssembly.instances['PLATE-1'].
68     elements[550:551]+\
69     mdb.models['Unstiff_plate_n=3'].rootAssembly.instances['PLATE-1'].
70     elements[600:601]+\
71     mdb.models['Unstiff_plate_n=3'].rootAssembly.instances['PLATE-1'].
72     elements[650:651]+\
73     mdb.models['Unstiff_plate_n=3'].rootAssembly.instances['PLATE-1'].
74     elements[700:701]+\
75     mdb.models['Unstiff_plate_n=3'].rootAssembly.instances['PLATE-1'].
76     elements[750:751]+\
77     mdb.models['Unstiff_plate_n=3'].rootAssembly.instances['PLATE-1'].
78     elements[800:801]
79     , name='Left-Surf')
80 # SET LOAD#
81     mdb.models['Unstiff_plate_n=3'].ShellEdgeLoad(createStepName='Step-1',
82     distributionType=UNIFORM, field='', localCsys=None, magnitude=1,
83     name='Load-1', region=
84     mdb.models['Unstiff_plate_n=3'].rootAssembly-surfaces['Left-Surf'])
85     mdb.models['Unstiff_plate_n=3'].loads['Load-1'].setValues(amplitude='Sin_Amp')
86
87     for ForceAmp in ForceAmpList:
88         EdgeLoad = ForceAmp/0.8*1E5
89         JobName = "P_%dE5_t0_0-0087" % (ForceAmp)
90
91         ## CHANGE LOAD##
92         mdb.models['Unstiff_plate_n=3'].loads['Load-1'].
93         setValues(magnitude=EdgeLoad)
94
95         ## CREATE JOB & SUBMIT ##
96         mdb.Job(activateLoadBalancing=False, atTime=None, contactPrint=OFF,
97         description='', echoPrint=OFF, explicitPrecision=SINGLE,
98         historyPrint=OFF, memory=90, memoryUnits=PERCENTAGE,
99         model='Unstiff_plate_n=3', modelPrint=OFF,

```

```
100     multiprocessingMode=DEFAULT, name=JobName,
101     nodalOutputPrecision=SINGLE, numCpus=4, numDomains=4,
102     parallelizationMethodExplicit=DOMAIN, queue=None, scratch='',
103     type=ANALYSIS, userSubroutine='', waitHours=0, waitMinutes=0)
104     mdb.jobs[JobName].submit(consistencyChecking=OFF)
105     mdb.jobs[JobName].waitForCompletion()
106
107     ## OUTPUT ##
108     execfile('out_data.py')
109
110     print 'Edge Load =', EdgeLoad
111
112 ## END OF SCRIPT ##
```

Appendix B

SWAY analyses

B.1 BASH-script for USFOS runs

```
1  #!/bin/bash
2  #
3  # Script that controls the execution of one or more analyses
4  # with parameter variation. The script calls different modules,
5  # each module doing it's own task.
6  #
7  # The file containing the parameters that are going to be substituted
8  # into the different data files are defined in the beginning of this
9  # script. The default (and recommended) filename is './input/parameters'
10 #
11 # This file is organized as a table, where the first line is a header
12 # line, one header per column. No spaces are allowed in the header. The
13 # column headers are the keys to look for in the files passed through the
14 # substitution process. The rest of the lines define each combination
15 # of parameters that is going to be excuted, one execution per line.
16 #
17 # If your computer has more than one processor core, the analysis
18 # part will be run in parallel. The number of parallel processes
19 # is automatically determined, but can be overridden by setting the
20 # THREADS variable to the number of parallel threads. If this value is
21 # set to 0 or a negative value, the number of threads will default to
22 # the maximum possible number.
23 #
24 # Written by Håkon Strandenes, hakostra@stud.ntnu.no, 2011-2012.
25 # Modified by Jonas G. Straume
26 #
27 # This file is licensed under the GNU General Public License,
28 # version 3, or later. Please see file LICENSE for details.
29 #
30 # ----- PARAMETERS ----- #
31 INPUTFILE="./input/parameters" # The file containing the parameter data
32 THREADS=0 # The number of parallel threads (0=auto)
33 # ----- #
```

```
34
35 # Define a function used to initialize modules
36 function initialize {
37     # Run all all scripts
38     for MOD in ./modules/*
39     do
40         if [ -f $MOD -a -x $MOD ]; then
41             $MOD init >> ./logs/init.log
42         fi
43     done
44 }
45
46 # Define function used to find what files that is going through substitution
47 function findfiles {
48     # Run all all scripts
49     for MOD in ./modules/*
50     do
51         if [ -f $MOD -a -x $MOD ]; then
52             $MOD files $1 | grep -v '^$' # The grep command is to remove empty lines
53         fi
54     done
55 }
56
57 # Do the postprocessing
58 function postp {
59     # Go through all scripts
60     for MOD in ./modules/*
61     do
62         if [ -f $MOD -a -x $MOD ]; then
63             $MOD postp2 >> ./logs/postp2.log
64         fi
65     done
66 }
67
68 # Make a folder for the contents of the terminal logs
69 if [ ! -d logs ]; then
70     mkdir logs
71 else
72     rm logs/*.log
73 fi
74
75 # Do the initialization
76 echo -n "Initializing folders..."
77 initialize
78
79 echo "Done."
80 echo -n "Assembling input files..."
81
82 # Reads the first line of the input file to get the column headers
83 read -r FIRSTLINE < $INPUTFILE
84
85 # Finds the number of columns
86 FIELDS='echo $FIRSTLINE | awk '{ print NF }''
87
88 # Make an array with the column/field names
89 for i in `seq 1 $FIELDS`
90 do
```

```

91 FIELD[$i]='echo $FIRSTLINE | awk '{ print $c }' c=$i'
92 done
93
94 # Reads the parameter file line by line
95 LINE=0
96 COMMAND=""
97 while read INPUTLINE
98 do
99     # Do not process the first line
100    LINE='expr $LINE + 1'
101    if [ $LINE -eq 1 ]; then
102        continue
103    fi
104
105    # Construct the case name/filename
106    CASENAME=""
107    for i in `seq 1 $FIELDS`
108    do
109        VALUE='echo $INPUTLINE | awk '{ print $c }' c=$i'
110        CASENAME="${CASENAME}_${FIELD[$i]:0:2}=$VALUE"
111    done
112    CASENAME=${CASENAME:1}
113
114    # Do the substitution process for all files returned by the modules
115    while read INPOUT
116    do
117        # If empty string, continue loop
118        if [ ${#INPOUT} -lt 3 ]; then
119            continue
120        fi
121
122        # Define file names
123        INPUT='echo -n $INPOUT | awk '{ print $1; }'`
124        OUTPUT='echo -n $INPOUT | awk '{ print $2; }'`
125
126        # Create folder for output file if it not exist
127        OUTDIR='dirname $OUTPUT'
128        if [ ! -d $OUTDIR ]; then
129            mkdir $OUTDIR
130        fi
131
132        # Copy original file to destination
133        cp $INPUT $OUTPUT
134
135        # Substitution process for each field
136        for i in `seq 1 $FIELDS`
137        do
138            VALUE='echo $INPUTLINE | awk '{ print $c }' c=$i'
139
140            # Substitute in header and model file
141            ./substitute ${FIELD[$i]} $VALUE $OUTPUT
142        done
143        done <<< "findfiles $CASENAME"
144
145        # Putting the job in the command string
146        COMMAND="${COMMAND}${CASENAME}\0"
147    done < "${INPUTFILE}"

```

```
148
149 # Find the number of threads your computer can run
150 if [ $THREADS -lt 1 ]; then
151     THREADS='cat /proc/cpuinfo | grep processor | wc -l'
152 fi
153
154 # Executing the commands in parallel
155 echo "Done."
156 echo "Running multiple analyses with $THREADS threads in parallel..."
157 echo -e $COMMAND | xargs -O -n 1 -P $THREADS ./runone analyze
158
159 # Running postprocessing
160 echo "Parallel processing done."
161 echo "Running postprocessing tasks..."
162
163 # No parallel run of postprocessing
164 echo -e $COMMAND | xargs -O -n 1 -P 1 ./runone postpl
165
166 # Final postprocessing
167 echo -n "Running final postprocessing..."
168 postp
169
170 ./findmax
171 echo "Done."
172 echo "Finished!"
```


Appendix C

Riser impact analyses

C.1 Data for the production riser

C.1.1 Details for the tapered stress joint

Production Riser - Taper Stress Joint	
Length	15140 mm
ID (internal diameter)	250.0 mm
Number of linear taper sections	3
Length of taper section 1	4000 mm
Length of taper section 2	4000 mm
Length of taper section 3	3200 mm
Lower flange OD	768 mm
Lower flange thickness	240.0 mm
Wall thickness:	
Top of taper section 1	14.5 mm
Top of taper section 2	22.0 mm
Top of taper section 3	32.0 mm
Bottom of taper section 3	41.0 mm
Material :	80 ksi grade steel
Weight estimate:	3300 kg

C.2 Result of the riser impact analysis

C.2.1 Result from the stiff bottom analysis

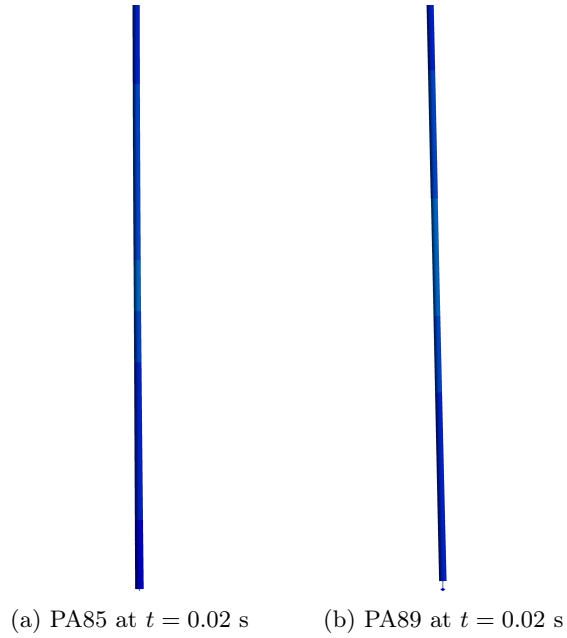


Figure C.1: Deformation of PA-riser



Figure C.2: Deformation of PC-riser

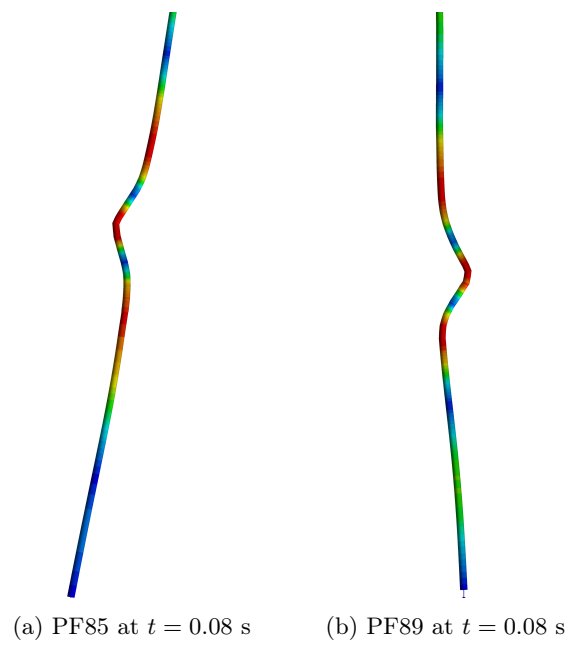


Figure C.3: Deformation of PF-riser

Table C.1: Stiffness used on bottom

Eq. linear stiffness	Scenario	Drop angle	USFOS def.	Deviation
$1.0 \cdot 10^7$ N/m	PA	85°	0.63 m	+5.0 %
		89°	0.63 m	+5.0 %
	PC	85°	0.78 m	-11 %
		89°	0.81 m	-8.0 %
	PF	85°	0.92 m	-18 %
		89°	1.07 m	-4.5 %
$1.0 \cdot 10^8$ N/m	PA	85°	0.17 m	-11 %
		89°	0.17 m	-11 %
	PC	85°	0.098 m	-65 %
		89°	0.13 m	-54 %
	PF	85°	0.081 m	-78 %
		89°	0.082 m	-77 %